GESP-7017
SEPT 1969

A DESIGN STUDY FOR A MAGNETOHYDRODYNAMIC POWER SYSTEM FOR A NUCLEAR ELECTRIC PROPELLED UNMANNED SPACECRAFT

QUARTERLY PROGRESS REPORT NO. 1

COVERING THE PERIOD 26 MAY 1969 TO 25 SEPTEMBER 1969

PREPARED UNDER CONTRACT JPL 952415

FOR

PROPULSION RESEARCH AND ADVANCED CONCEPTS SECTION
JET PROPULSION LABORATORY
4800 OAK GROVE DRIVE
PASADENA, CALIFORNIA, 91103

NSP NUCLEAR SYSTEMS PROGRAMS
ISOTOPE POWER SYSTEMS OPERATION

GESP-7017
SEPT 1969

A DESIGN STUDY FOR A MAGNETOHYDRODYNAMIC POWER SYSTEM FOR A NUCLEAR ELECTRIC PROPELLED UNMANNED SPACECRAFT

QUARTERLY PROGRESS REPORT NO. 1

COVERING THE PERIOD 26 MAY 1969 TO 25 SEPTEMBER 1969

PREPARED UNDER CONTRACT JPL 952415

FOR

PROPULSION RESEARCH AND ADVANCED CONCEPTS SECTION
JET PROPULSION LABORATORY
4800 OAK GROVE DRIVE
PASADENA, CALIFORNIA, 91103

THIS WORK WAS PERFORMED FOR THE JET PROPULSION LABORATORY, CALIFORNIA INSTITUTE OF TECHNOLOGY AS SPONSORED BY THE NATIONAL AERONAUTICS AND SPACE ADMINISTRATION UNDER CONTRACT NAS7-100

ISOTOPE POWER SYSTEMS OPERATION
GENERAL ELECTRIC
SPACE DIVISION
KING OF PRUSSIA PARK
P.O. BOX 8661 • PHILADELPHIA, PENNA., 19101

This report contains information prepared by the General Electric Company under JPL subcontract. Its content is not necessarily endorsed by the Jet Propulsion Laboratory, California Institute of Technology, or the National Aeronautics and Space Administration.

ABSTRACT

This report discusses the progress made in the first quarter of a one-year design study of nuclear-electric propelled unmanned spacecraft using a magnetohydrodynamic (MHD) power system. This report includes as appendices the analytical treatment of the MHD system as developed by Jet Propulsion Laboratory and upon which the spacecraft analysis is based. The study guidelines and approach are defined here, and the characteristics of one launch vehicle, the thruster subsystem, and the payload and communications system are presented.

The MHD power conversion system is described and methods used to calculate MHD system parameters are discussed. This report includes the initial estimation of baseline (300 kWe) system design parameters and a discussion of the arrangement and structural arguments used to select system configuration. The system startup technique is identified, and the nuclear reactor and primary radiator characterization are presented.

TABLE OF CONTENTS

TABLE OF CONTENTS (continued)

LIST OF ILLUSTRATIONS

LIST OF ILLUSTRATIONS (continued)

LIST OF TABLES

1. INTRODUCTION

1. INTRODUCTION

On May 26, 1969, the General Electric Company began a design study for the magnetohydrodynamic (MHD) power system for a nuclear-electric propelled unmanned spacecraft. This work is being performed for the Jet Propulsion Laboratory under contract number JPL 952415, and is based on MHD system technology being developed by the Jet Propulsion Laboratory. The purpose of this study is to provide size, weight and mission performance estimates for nuclear-electric propelled unmanned spacecraft using MHD power systems rated at 100 kWe to 3 MWe. This study is also intended to guide future MHD development by discovering specific requirements associated with spacecraft power system design. The spacecraft design of principal interest is one whose unconditioned power output is a nominal 300 kW(e). The weight goal for this spacecraft is 10,000 pounds including reactor, shielding, MHD conversion equipment, power distribution and conditioning equipment, thruster subsystems, and structure.

The work of this study program is divided into four principal tasks:

a. Task 1 - System Evaluation - The purpose of this task is to establish guidelines and design requirements for the program and to measure the designs generated in the program against these guidelines and requirements.

b. Task 2 - Powerplant Design - The purpose of this task is to provide the engineering analysis and design information necessary for spacecraft design layout. This will include parametric analyses to identify the influence of major plant variables on powerplant and spacecraft characteristics. This task also includes evaluation of the effects of changes in technology levels associated with the powerplant components.

c. Task 3 - Spacecraft Design - The purpose of this task is to define the arrangement, mechanical design and weight estimation for the MHD spacecraft designs.

d. Task 4 - Mission Analysis and Engineering - The purpose of this task is to perform the analysis necessary to evaluate the mission capabilities of the various spacecraft, and to perform a preliminary assessment of prelaunch, launch and flight operations, specifically with respect to aerospace nuclear safety.

In the first half of this one-year study a baseline design spacecraft and powerplant are being developed. This baseline design is a 300 kWe system and is being based on relatively conservative estimates of component technology. In the second half of the year the spacecraft and the powerplant design will be varied parametically to evaluate the effects of changes in output power level and operating parameters, and to evaluate the effects of improvements in the technology of key components. At the end of the year-long Phase I, a reference MHD spacecraft design will be selected. Phase I is then to be followed by a Phase II study, of about a year's length, in which this reference design will receive detailed design analysis including startup and control analysis.

The MHD spacecraft study is being performed concurrently with a design study of a thermionic reactor power system for nuclear-electric propelled unmanned spacecraft, (JPL Contract No. 952381). Wherever possible, design bases for the MHD spacecraft are being made the same as those for the thermionic spacecraft in order to provide a clear comparison of these two power systems. In particular, the MHD spacecraft baseline design is using the same payload thruster subsystem and mission profile as the Phase I thermionic reactor spacecraft.

The MHD spacecraft study is proceeding on schedule. The computer programs for MHD generator and cycle analysis have been received from JPL and converted to basic FORTRAN IV for use on the IBM 1130 computer. Preliminary startup and reactor characterization have been completed. Configuration tradeoffs for the baseline design are complete and detailed design has begun. The remaining sections of this report discuss the progress to date. Appendices I and II, which reproduce Dr. D. G. Elliott's analytical treatment of the MHD generator and cycle, are included for the reader's convenience, since this summary treatment is unpublished.

2. TECHNICAL DISCUSSION

2. TECHNICAL DISCUSSION

2.1 MHD SYSTEM REQUIREMENTS

2.1.1 BASELINE DESIGN GUIDELINES

The system requirements and design guidelines for the baseline design have been identified; they are:

a. Power Output - A nominal 300 kWe adjusted as necessary to match thruster system and other load requirements

b. Launch Vehicle - The Titan IIIC-7

c. Mission - Jupiter planetary orbiter. Starting from a 750 nm earth orbit, the spacecraft will use low, ion thrust to spiral away from earth, reach Jupiter and decelerate into Jovian orbit. The estimated time periods and power levels are as follows:

MISSION MODE	POWER LEVEL (kWe)	TIME (Days)
Spiral Escape from Earth	300	50
Accelerating Thrust	300	160
Coast	30	120
Decelerating Thrust	300	270
Jovian Orbit Operation	30	(one orbit, 17 days minimum)

d. MHD Cycle - One stage with two nozzles using impinging stream separation

e. Cycle Inlet Temperature - 1800°F (corresponds to reactor outlet temperature in a one-loop system)

f. MHD Loop Containment Material - Cb-1Zr

g. Radiator Type - Triform, stainless steel heat pipe

h. Permanent Shield Materials - Lithium hydride and tungsten

i. Radiation Dose Limits For Payload, Power Conditioning and Communications Equipment -

Neutron	10^{12} nvt > 1 mev
Gamma	10^{7} rad

j. Meteoroid Survival Criteria - The meteoroid model is based on the following:

1. Penetration Model

$$t = 0.5\, m^{0.352}\, \rho_m^{1/6}\, v^{0.875}$$

2. Meteoroid Flux

$$\phi = \alpha\, m^{-\beta}$$

3. Non-Puncture Probability

$$P(0) - e^{-\phi AT}$$

4. Effective Thickness

$$t_{eff} = 0.432\ t(\text{Jupiter})$$

where

t	=	radiator armor thickness, cm
ρ_m	=	meteoroid density, gm/cm^3
m	=	meteoroid mass, gm
v	=	meteoroid velocity, km/sec
α	=	empirical coefficient
β	=	empirical exponent
$P_{(0)}$	=	non-puncture probability
ϕ	=	cumulative meteoroid flux, number particles/m^2sec

A = projected vulnerable area of the spacecraft (radiator), m^2

T = exposure time, sec

ASSUMED VALUES

ρ_m = $0.5 g/cm^3$ α = 6.62×10^{-15}

V = 20 km/sec β = 1.34

T = 7.2×10^7 sec (20,000 hr) $P_{(0)}$ = 0.95

2.1.2 ALTERNATE DESIGN GUIDELINES

The requirements and design guidelines for the alternate designs differ from those of the baseline design as follows:

a. Power Output - 100 kWe, 300 to 500 kWe, and 3 MWe

b. Launch Vehicle - Titan IIIC-7 and Saturn V

c. Missions

1. 100 kWe to escape on Titan IIIC-7

2. 300 to 500 kWe to low orbit on Titan IIIC-7

3. 300 to 500 kWe to escape on Saturn V

4. 3 MWe to low orbit on Saturn V

d. MHD Cycle - 1-6 stage

e. MHD Cycle Inlet Temperature - 1600 to 2200°F

f. MHD Containment Material - One advanced material

g. Radiator Type - Flatplate or triform, stainless steel or columbium heat pipe.

2.2 SPACECRAFT DESIGN GUIDELINES

2.2.1 PAYLOAD

The scientific payload and its communications system are assumed to

weigh one metric ton, 2205 pounds, and to have a full power requirement of one kWe. Reference 1 has identified tentative payload details which have been adopted for the MHD spacecraft as well. The communications subsystem is assumed to require 800 of the 1000 W alloted; subsystem component characteristics are listed in Table 2-1. A payload equipment bay of approximately nine feet in diameter and at least 15 inches in height can contain the payload equipment excluding the deployable antenna, and provide adequate surface area for the payload thermal control radiator.

TABLE 2-1. COMMUNICATIONS SUBSYSTEM CHARACTERISTICS

Low Gain Antenna (Receiving)	
Diameter	6 inches
Weight (including cable)	2.5 pounds
Deployment Structure Weight	Negligible
High Gain Antenna (Transmitting)	
Diameter	9 feet
Weight (including cable)	31 pounds
Deployment Structure Weight	8 pounds
Power Input	800 watts
Power Transmitted	200 watts
Bit Rate (120 feet diameter receiving antenna)	10^4 bits/sec
Transmitter	
Weight	20 pounds
Size	6 x 6 x 20 inches

2.2.2 THRUSTER SUBSYSTEM

The thruster subsystem for the MHD spacecraft has been defined by Reference 2 and has the following general characteristics:

a. Spacecraft propulsion is provided by 31 equal size electron bombardment ion thruster engines using mercury as the propellant.

b. Six spare thrusters will be provided for a total of 37 units. Considering switching and power conditioning requirements, six spares provide one spare for each group of five operating thrusters.

c. Thrust vector control will be provided by a three axis attitude control system (two axis translation, one axis gimbal).

Guidelines for thruster subsystem design are given in Table 2-2. Thruster power supply requirements are listed in Table 2-3, and subsystem weights are given in Table 2-4.

TABLE 2-2. GUIDELINES FOR THRUSTER SUBSYSTEM DESIGN

1. Total Conditioned Power to Thrusters	240 kW
2. True Specific Impulse	5000 seconds
3. Number of Thrusters	37
4. Thruster Redundancy	20 percent
5. Attitude Control	Electric Propulsion System
6. Maximum Envelope Diameter	10 feet
7. Thrust Duration	10,000 hours
8. Technology	Estimated for 1980

TABLE 2-3. THRUSTER POWER SUPPLY REQUIREMENTS

Supply Number	Supply Name	Type	Output[1]	NOMINAL RATING					MAX. RATING			Control Range, A
				Volts	Amps	Watts	Reg. %	Peak Ripple	Volts	Amps	Amps Limit[2]	
1	Screen	DC	V	3100	2.32	7200	1.0(V)	5	3200	2.32	2.60	2.0 - 2.4
2	Accelerator	DC	F	2000	.02	40	1.0(V)	5 @ 0.2 A	2100	0.20[3]	0.21	---
3	Discharge	DC	V	35	8.3	290	1.0(V)	2	150 @ 50 mA	9 @ 37V	10	7.5 - 9.0
4	Mag. - Man.	DC	F	15	.7	11	1.0(I)	5	20	1.0	1.0	---
5	Cath. Htr.[4]	AC	F	10	4.0	40	5.0	5	11	4.4	4.1	---
6	Cath. Keeper	DC	F	10	0.5	5	1.0(I)	5	150 @ 50 mA	1.0 @ 20 V	1.0	---
7	Main Vapor.	AC	V	0.6	1.0	1	Loop	5	8[5]	2.0	2.2	0.5 - 1.5
8	Cath. Vapor	AC	V	0.3	0.5	1	Loop	5	8[5]	1.0	1.1	0.2 - 0.8
9	Neut. Cath. Htr.	AC	F	10	2.0	20	5.0	5	11	2.2	2.2	---
10	Neut. Vapor.	AC	V	0.3	0.5	1	Loop	5	8[5]	1.0	1.1	0.2 - 0.8
11	Neut. Keeper	DC	F	10	0.5	5	1.0(I)	5	150 @ 50 mA	1.0 @ 20 V	1.0	---

(1) V = Variable, F = Fixed

(2) Current limit or overload trip level.

(3) Current at this level for less than 5 min. at low repetition rate.

(4) Needed only during startup or until discharge reaches 3A.

(5) Startup only.

TABLE 2-4. THRUSTER SUBSYSTEM WEIGHTS

COMPONENT	WEIGHT (POUNDS)
Thrusters (37)	585
Thrust Vector Control System	548
Miscellaneous (wiring, adapters, etc.)	100
	1,233

2.2.3 LAUNCH VEHICLE INTERFACE

The Titan IIIC-7 launch vehicle will be used to boost the spacecraft into a 750 nm (design objective) circular earth orbit. This vehicle is similar to the Titan IIIF except that it uses a standard transtage. It is a nonmanrated vehicle and employs the stretched Stage I tanks and seven segment, 120 inch diameter solids characteristic of the Titan IIIM. The overall length of the vehicle to the payload separation plane is approximately 117 feet.

2.2.3.1 Physical Constraints on Shroud Size

The height of the 50-ton bridge crane above the launch vehicle is one identified constraint on the aerodynamic shroud (hence payload) overall length. At the Eastern Test Range (ETR) Titan vehicles are launched from Launch Complex 40 or 41. With the Titan vehicle in place on the Mobile Service Tower, the clearance between the bridge crane and the Titan IIIC/7 payload interface is only 75 feet while for the Titan IIIC, this clearance is 88 feet. The decrease in available clearance is due to: (1) a 5-1/2 foot increase in the length of the first stage, and (2) a 7-1/2 foot increase in launch stand height. The launch vehicle contractor suggests the possibility of using ETR launch pad 37B, which has been used for S-IB launches. There would be virtually no height limitations.

On the launch pad, a universal environmental shelter is used to provide temperature and humidity control, and RF protection. It also acts as a clean room for the transtage and payload envelope. At the present time the limit of this facility is 55 feet, which means that this is the maximum payload plus transtage length which can be accommodated. Longer lengths will require major construction revisions to the shelter.

2.2.3.2 Flight Fairing Weight and Payload Penalty

During a "nominal" launch of the Titan IIIF vehicle, the flight fairing is normally jettisoned at 280 seconds, which is just after completion of the Stage I burn. In order to prevent freezing of the liquid metal coolant during launch, it may be desirable to retain the flight fairing as a radiation barrier until after reactor startup in earth orbit. However, this procedure imposes a severe payload weight penalty which depends on the shroud length (weight) and the terminal orbit altitude.

Figure 2-1 shows the flight fairing weight and the payload penalty as a function of shroud length, assuming shroud jettison at 280 seconds into the mission. If the shroud is retained past earth orbital insertion, then the payload weight penalty will be equal to the shroud weight. It should be noted that as the terminal orbital altitude increases, the payload penalty decreases for normal shroud ejection since a larger portion of the ΔV is added after shroud ejection. The curves are based on the data supplied by the Martin Marietta Corporation.

The effect of shroud retention on payload capability is shown in Figure 2-2. The upper lines define the Titan IIIC/7 payload capability for a 28.5 degree orbital inclination mission with shroud jettison occurring at 280 seconds into the mission. The lower curves show the effect of retaining the shroud through achievement of final Earth orbit.

Under nominal conditions, and with a 35-foot shroud, the vehicle can deliver 30,000 pounds into a 630 nm circular orbit. Employing longer shrouds, with jettison at 280 seconds, reduces the payload capability (initial mass in Earth orbit) as shown in Table 2-5.

Alternatively, injecting 30,000 pounds of payload into circular orbit will decrease the maximum possible orbit altitude as shown in Table 2-6.

If the shroud is jettisoned after achieving Earth orbit (630 nm), the payload capability will be reduced as shown in Table 2-7.

2.3 MHD POWER SYSTEM OPERATION AND ANALYSIS

2.3.1 TWO-COMPONENT LIQUID METAL MHD POWER SYSTEM

2.3.1.1 Power System Fluid Flow

Figure 2-3 illustrates the flow arrangement by which a two component liquid metal MHD power system can generate useful amounts of electrical energy with no moving parts except the fluids themselves. As the

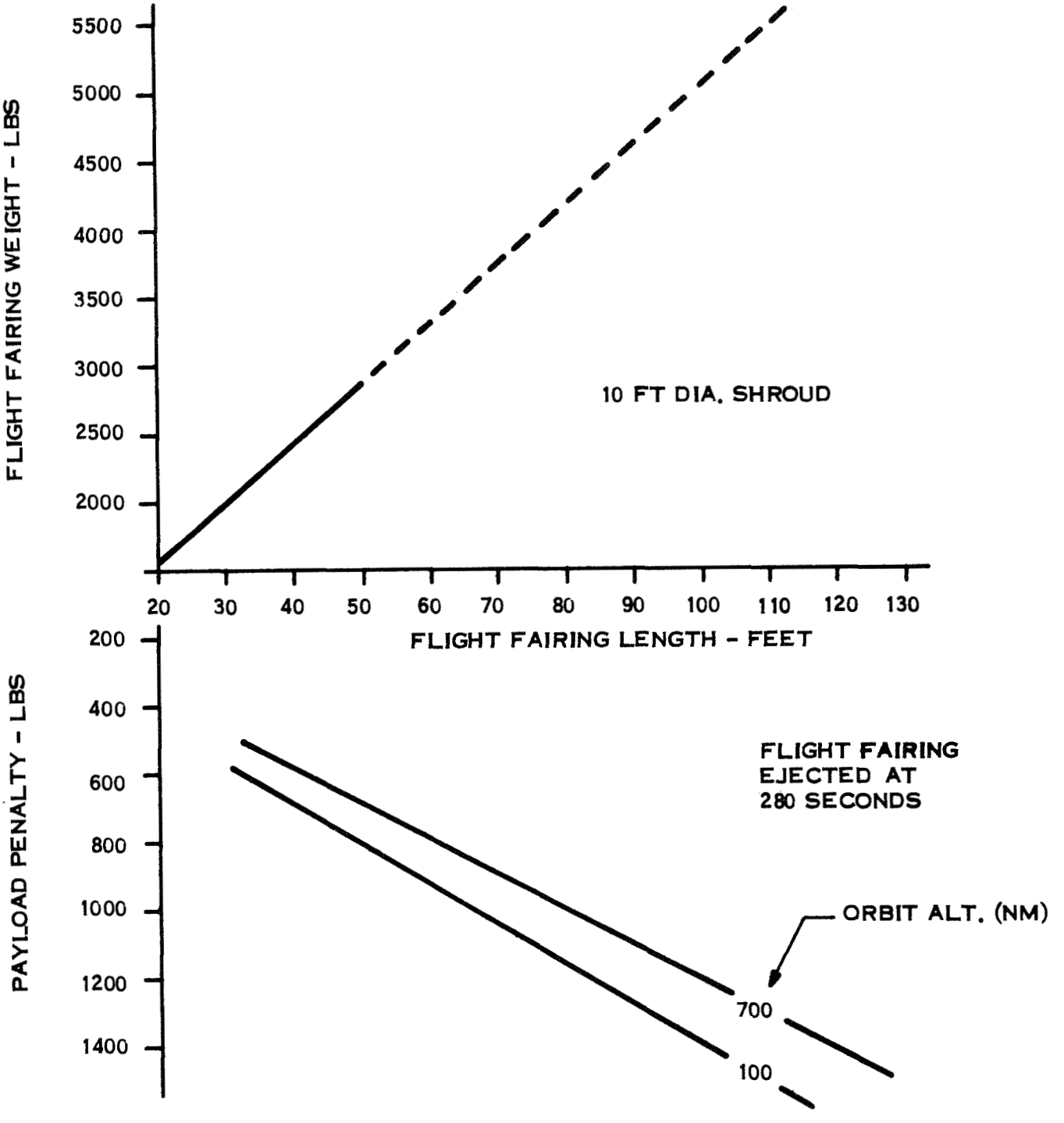

Figure 2-1. Flight Fairing Weight and Payload Penalty (Titan IIIC/7)

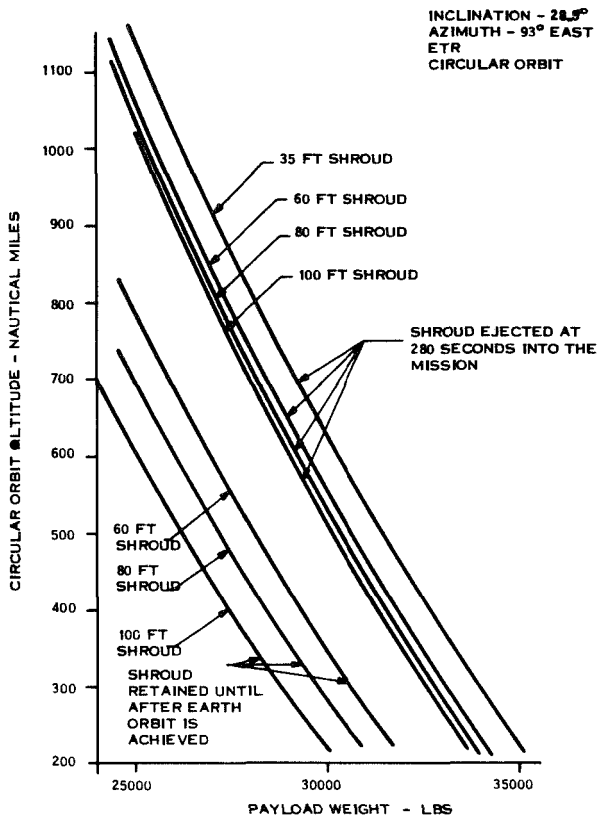

Figure 2-2. Effect of Shroud Retention on Payload Capability (Titan IIIC/7)

TABLE 2-5. MAXIMUM PAYLOAD CAPABILITY WITH SHROUD EJECTION AT 280 SECONDS

Shroud Length (feet)	Shroud Penalty (pounds)	Maximum Payload Weight (pounds)
60	808	29,191
80	1021	28,978
100	1234	28,765

TABLE 2-6. MAXIMUM EARTH ORBITAL ALTITUDE FOR A 30,000 POUND PAYLOAD, WITH SHROUD JETTISON AT 280 SECONDS

Shroud Length (feet)	Maximum Orbit Altitude (nm)
60	555
80	530
100	512

TABLE 2-7. MAXIMUM PAYLOAD CAPABILITY AT 630 NM WITH SHROUD EJECTION AFTER ACHIEVING EARTH ORBIT

Shroud Length (feet)	Shroud Penalty (pounds)	Maximum Payload Weight (pounds)
60	3300	26,700
80	4200	25,800
100	5000	25,000

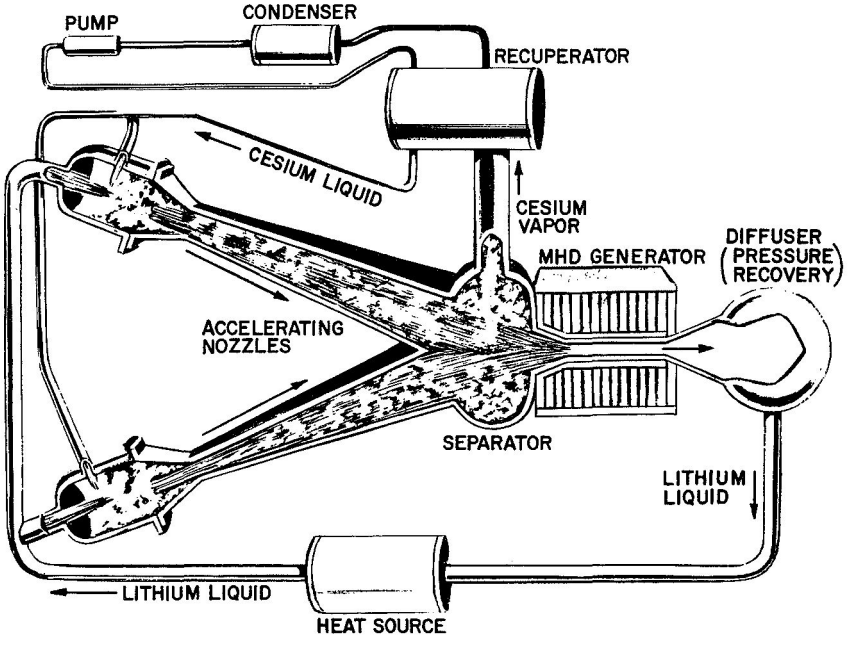

Figure 2-3. Lithium-Cesium MHD Cycle

illustration shows, lithium is heated in a heat source and injected into expansion nozzles with liquid cesium. Upon mixing in the nozzles, heat transfer from the lithium causes the cesium to boil. The lithium liquid does not boil but is dispersed in the stream by the boiling of the cesium. As the lithium breaks up into smaller and smaller drops its surface-to-volume ratio increases, enhancing heat transfer to the cesium vapor. The high specific heat of lithium along with a retatively high lithium mass flow to cesium mass flow ratio enables the cesium boiling and expansion in the nozzles to take place at almost isothermal conditions.

The expansion of the cesium vapor as it travels down the nozzles accelerates the entrained lithium liquid droplets to high velocities. At the convergence of the two nozzles the impingement of the two streams requires each to undergo a change in direction. The resulting lateral acceleration imposed on the flow stream causes its components to separate into strata with the lithium collecting in the center of the combined stream and the cesium vapor moving out to the sides of the stream. The combined lithium streams enter a diffuser where the stream pressure is raised threefold to dissolve any remaining cesium bubbles and the lithium stream then passes through the MHD generator duct where much of the stream's kinetic energy is converted to electrical energy (see Paragraph 2.3.1.2 - Energy Conversion, following). At the MHD generator exit, the lithium stream passes into a diffuser where most of its remaining kinetic energy is converted to pressure head in order to pump the lithium through the heat source and back around to the nozzle entrance with more heat.

The cesium vapor, separated from the lithium streams at the nozzle exits, is passed out through a recuperator to a condenser. The condensed lithium is pumped electromagnetically back through the recuperator to the nozzle entrances where it can be vaporized again.

A simpler method of stream separation is used in the single nozzle MHD test system shown in Figures 2-4 and 2-5. This system, which is currently being used for development testing by Dr. D. G. Elliott at Jet Propulsion Laboratory, operates at about room temperature with NaK alloy in place of lithium and compressed nitrogen gas expanding to accelerate the liquid phase. In this arrangement, the vapor and liquid streams are separated by impingement on an inclined plate, see Figure 2-5. The single nozzle system, although simpler to construct, is less desirable because of the skin friction losses the liquid stream suffers in passing across the separator plate. In the dual nozzle system the opposing streams, moving at equal speeds, provide the flow diversion thus eliminating this friction loss and improving system overall efficiency from about six and one-half percent to almost eight percent. Although the dual nozzle system will require flow balancing, its improved efficiency makes it the more attractive design.

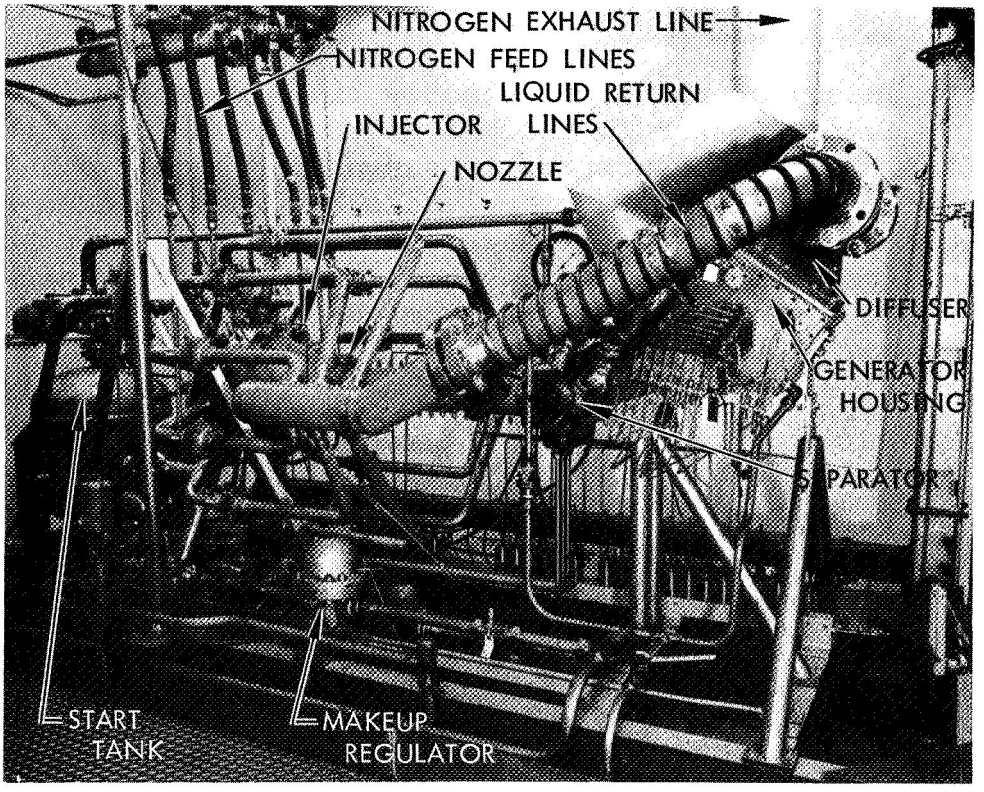

Figure 2-4. NaK/N_2 MHD Test System

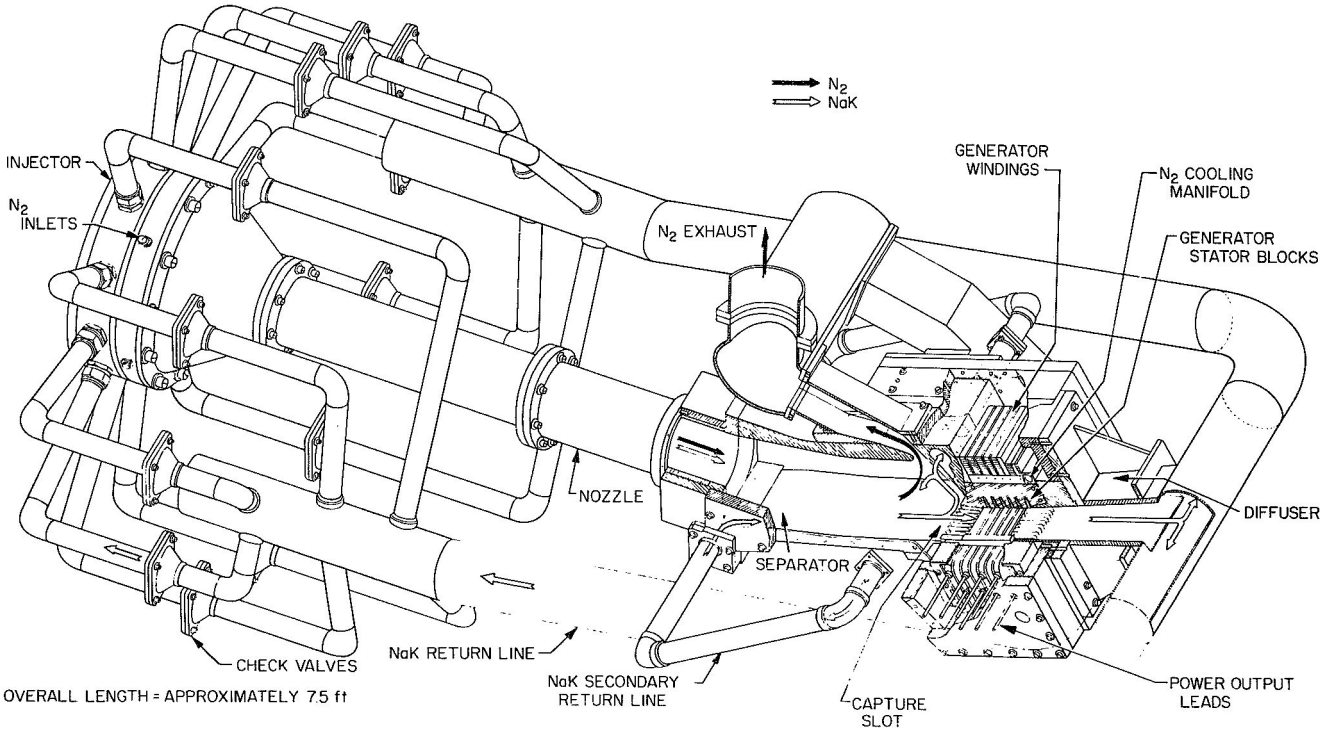

Figure 2-5. Cutaway NaK/N_2 MHD Test System

2.3.1.2 Energy Conversion

The kinetic energy of the high velocity lithium stream is converted to alternating current power in the MHD generator; a schematic depiction of this flat induction generator is shown in Figure 2-6. The lithium stream, an electrical conductor, enters the channel at a velocity U, as indicated in the figure. A magnetic field, B, set up across the channel acts on this moving conductor to generate a transverse current J. The magnetic field is time-varying and the generator length, L, is equal to one wavelength.

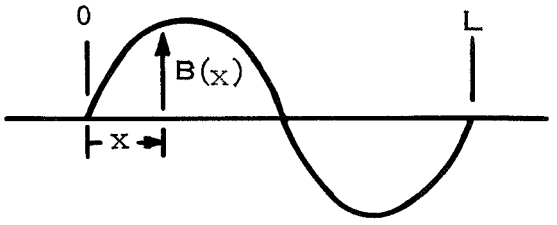

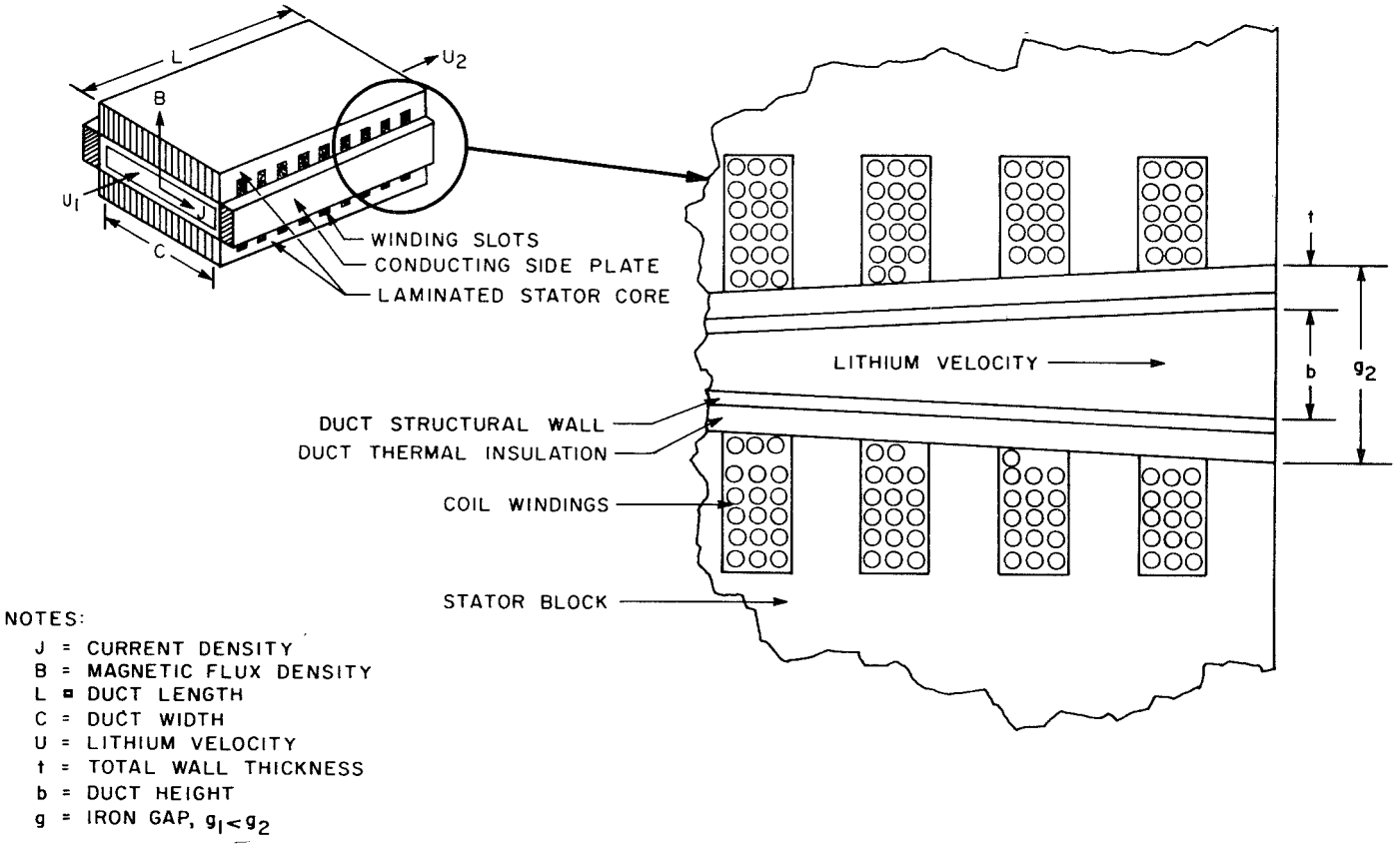

Figure 2-6. Schematic of a Flat AC Induction Generator

The induced current, J, has a negative analog, -J, induced by this time-varying, one-wavelength, travelling field. J and -J are L/2 apart and are electrically connected by the conducting side plates of the generator to complete a current loop. This lithium current in turn induces a power current in the same windings of the generator in which the exciting current runs. The power current is not in phase with the exciting current and the exciting current is derived from the power current by the use of capacitors. Typically, the reactive power exceeds the net usable power by a factor of four. The induction of current in the lithium and, in turn, in the windings exerts a retarding force on the lithium stream. Thus, some of the kinetic energy of that stream is converted into electrical energy.

2.3.2 METHODS OF ANALYSIS

Based on the analysis presented in Appendices I and II, Dr. Elliott has written two programs used in MHD generator and cycle calculations.

These two programs "GENERATOR" and "CYCLE-B" are both written in CAL, a language used by Tymshare, Inc. Both programs have been written in basic FORTRAN IV for use on the IBM 1130 computing system.

The IBM 1130 system configuration at General Electric-Valley Forge includes a processor with 8K active memory and 512K on-line disk unit. We have a 300 cpm card reader and a 110 lpm line at a time printer included in the system.

Unfortunately, neither program fits in 8K of storage and a technique called LOCALING must be used to run these programs. Basically, this means that the mainline program and one subroutine are loaded into the area of core occupied by the first subroutine as they are needed.

This technique obviously slows down the execution of the programs. Execution time including input and output for the generator program is about three to four minutes, and for the cycle program about one minute.

2.3.2.1 Generator Program

The IBM 1130 version of the generator program is called MHDGN. The required input is described below with the first column showing the variable identification used in MHDGN, and the second the nomenclature used in the analysis of Appendix I.

M1	$\dot{m}$	flow rate (Kg/sec)
U1	U_1	inlet velocity (m/sec)

U2	U_2	exit velocity (m/sec)
C	C	Channel width (m)
D1	ρ	fluid density (Kg/m^3)
V5	μ	fluid viscosity ($N\text{-}sec/m^2$)
CO	σ	fluid electrical conductivity (mho/m)
I80	I_{ec_1}	eddy-current amp-turns in upstream compensating pole (amps)
I81	I_{ec_2}	eddy-current amp-turns in downstream compensating pole (amps)
LO	L_{c1}	length of upstream compensating pole (m)
L1	L_{c_2}	length of downstream compensating pole (m)
WO	c_1	mean channel height in upstream compensating pole (m)
W1	c_2	mean channel height in downstream compensating pole (m)
TWALL	t_w	wall thickness (m)
C_{LOSS}	α	coil loss factor
C_{TEMP}	T_c	coil temperature (^oC)
SATFD	B_s	saturated field (T)
NSLOT	N	number of slots
INFLD	B_1	inlet fielt (T)
ENDU		number of upstream end slots (=1 or 2)

Figure 2-7 shows the subroutine calling schematic of MHDGN. Listed below are the subroutine names and a brief description of the purpose of each.

MHDGN	Mainline program, directs logic of the whole code
INPUT	writes the input values

NAMLT simulated "namelist" input

SUB9 calculations common to TW and end slots

SUB11 slot calculations in traveling wave region

SUB13 end slot calculations

SUB20 calculations certain parameters required throughout code

SUB31 optional detailed calculations

SUB34 end slot spacing

OUT41 slot by slot output

OUT42 sector powers output

OUT43 optional calculations output

OUT46 summary output

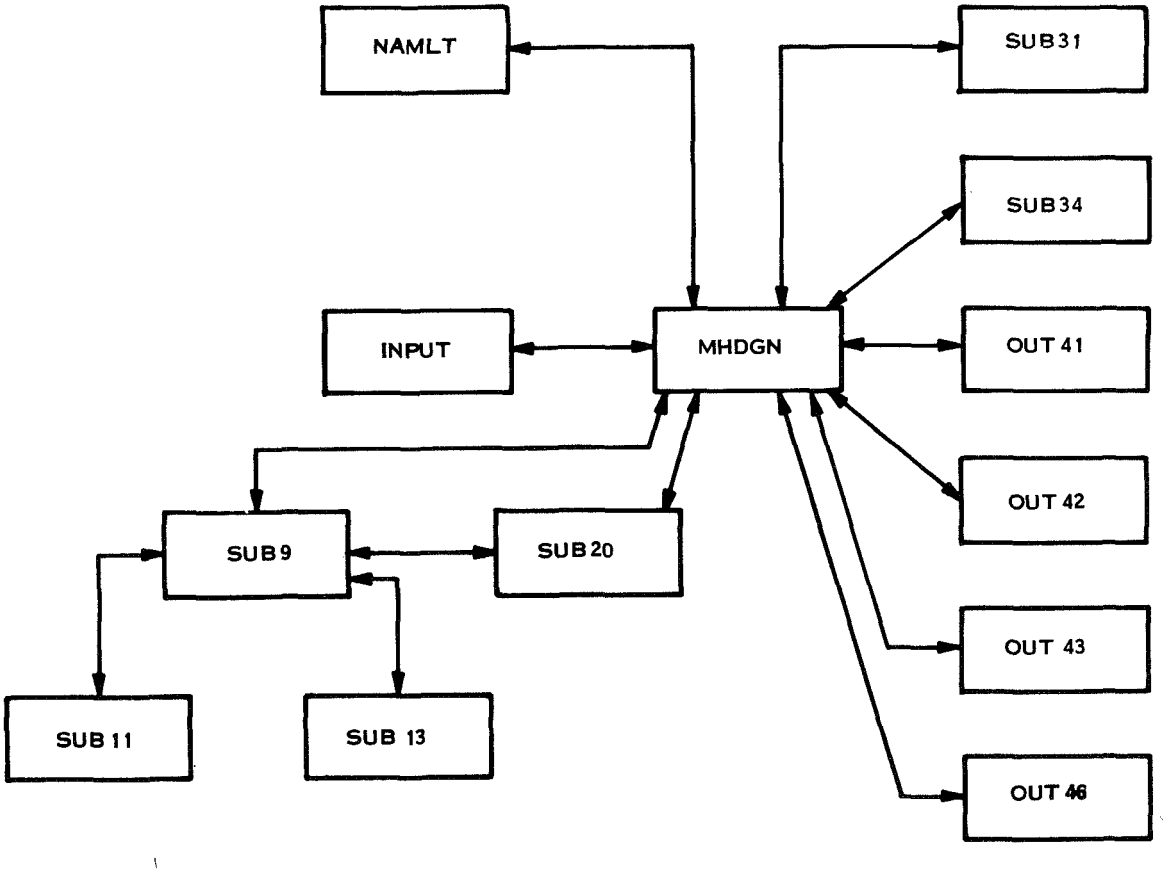

Figure 2-7. Subroutine Calling Schematic of MHDGN

2.3.2.2 Cycle Program

The IBM 1130 version of the cycle program is called MHDCY. The required input is described below with the first column showing the variable identification used in MHDCY and the second the nomenclature used in the analysis in Appendix II.

CASE		nozzle case number
A2A	A_2/A^*	nozzle area ratio
CH2	C/h_2	nozzle exit width/height ratio
PEOUT	P_e	net electrical power output (w)
THETA	θ	jet impingement half angle (rads)
ZKV	K_v	velocity adjustment factor
RV3	r_{v3}	capture slot gas/liq. volume ratio
ZL1C	L_1/c	upstream diffuser length/width ratio
ZL2C	L_2/c	downstream vane length/width ratio
ZN1	N_1	number of upstream vane channels
ZN2	N_2	number of downstream vane channels
ETAP	η_P	cesium pump efficiency
DELP1	$P_{6,7}$	heat source pressure drop (N/m^2)
DELP2	$P_{8,10}$	separator exit to condenser inlet pressure drop (N/m^2)
DELP3	$P_{12,13}$	recuperator liquid pressure drop (N/m^2)
DELP4	$P_{10,11}$	condenser pressure drop (N/m^2)
ETAG	η_g	generator traveling wave region efficiency
FREQ	f	generator frequency (Hz)
THETC	θ_c	compensating pole flux (Wb)

The mainline program MHDCY does all the calling in this code. Listed below are all the subroutines used in MHDCY and a brief description of their purpose.

MHDCY mainline program, station by station calculations

NAMLT simulated "namelist" input

NOZLE performs table look-up for nozzle conditions

CYC3 nozzle flow conditions at stations one and two

FF4 velocity loss in vane channels

T3 cesium saturation temperature loop

FINAL power and efficiency calculations

CYCOT output routine

Listings of both the MHDGN and MHDCY programs and sample cases are available, but have been omitted from this report for brevity.

2.3.2.3 Generator Variable Sensitivity

The CAL generator program supplied by JPL was converted to basic FORTRAN IV, and included the modification for a symmetric generator with the impinging nozzles separator. After satisfactory checkout against the supplied sample program, the input data for the sample case was rounded out and used to generate a base reference case. The rounded input data for this case was:

M1 Kg/sec	U1 m/sec	U2 m/sec	C m	I8(1) Amp	I8(2) Amp	L(1) cm	L(2) cm	H1 cm	H2 cm	I(1) mm	I(6) Tesla
90	116	61	0.23	175	140	5	5	1.7	1.7	2.5	0.46

The principal results for this case were:

P_{induc} = 337.9 kW,

P_{coil} = 8.04 kW,

P_{net} = 329.8 kW,

P_{reac} = 1248.5 kW, and

net efficiency η_{net} = 0.730.

The program was then run to determine the effect on the base case values of varying one input quantity at a time. This quantity X (=U1, M1, etc. in turn) was varied over a small range about the base case value, X_{ref}, to determine a sensitivity factor

$$\frac{dQ}{dX} \times \frac{X_{ref}}{Q_{ref}}$$

where Q was an output quantity such as P_{net}, η_{net}, P_{reac} and P_{coil}.

The sensitivity factors for P_{net} in Figure 2-8 show that U1, M1 and U2 are by far the most influential on net power, while, from Figure 2-9, M1, U2 and C have the most effect on net efficiency. These sensitivity factors can be useful for interpolation when a particular operating point is required.

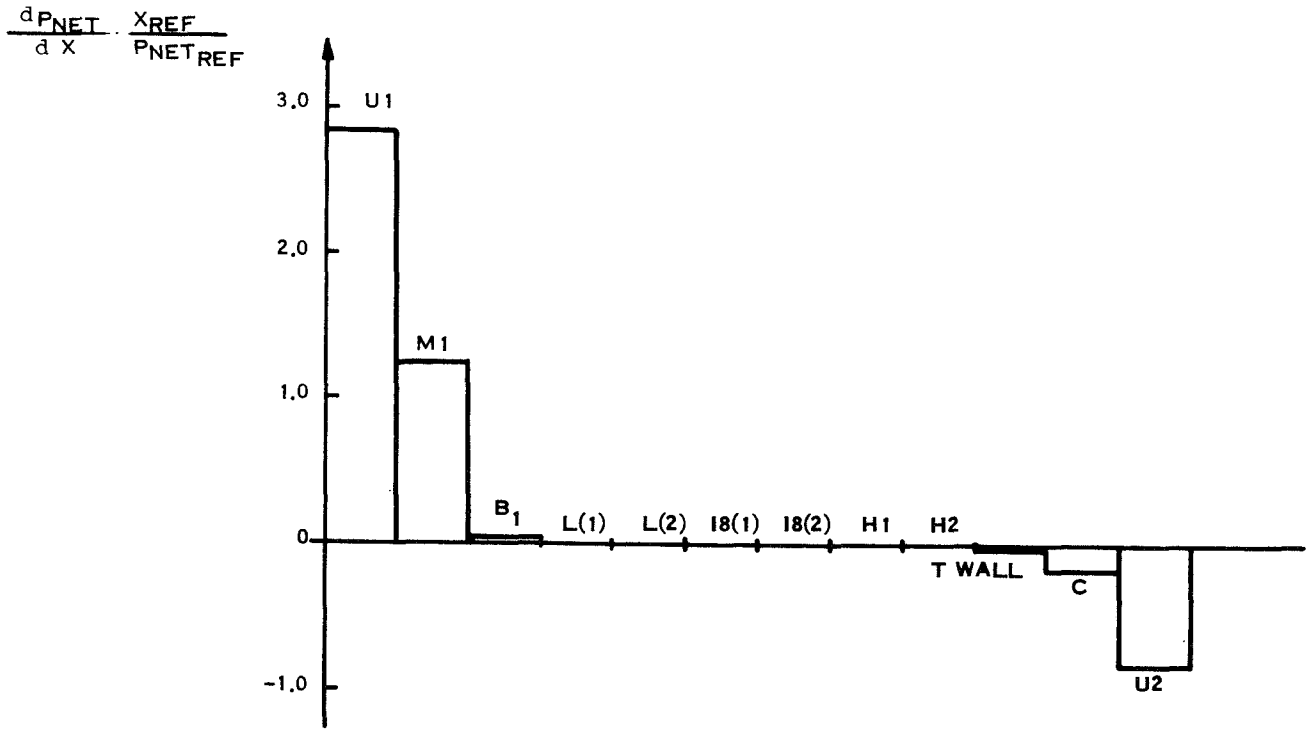

Figure 2-8. Sensitivity Factors for Net Power

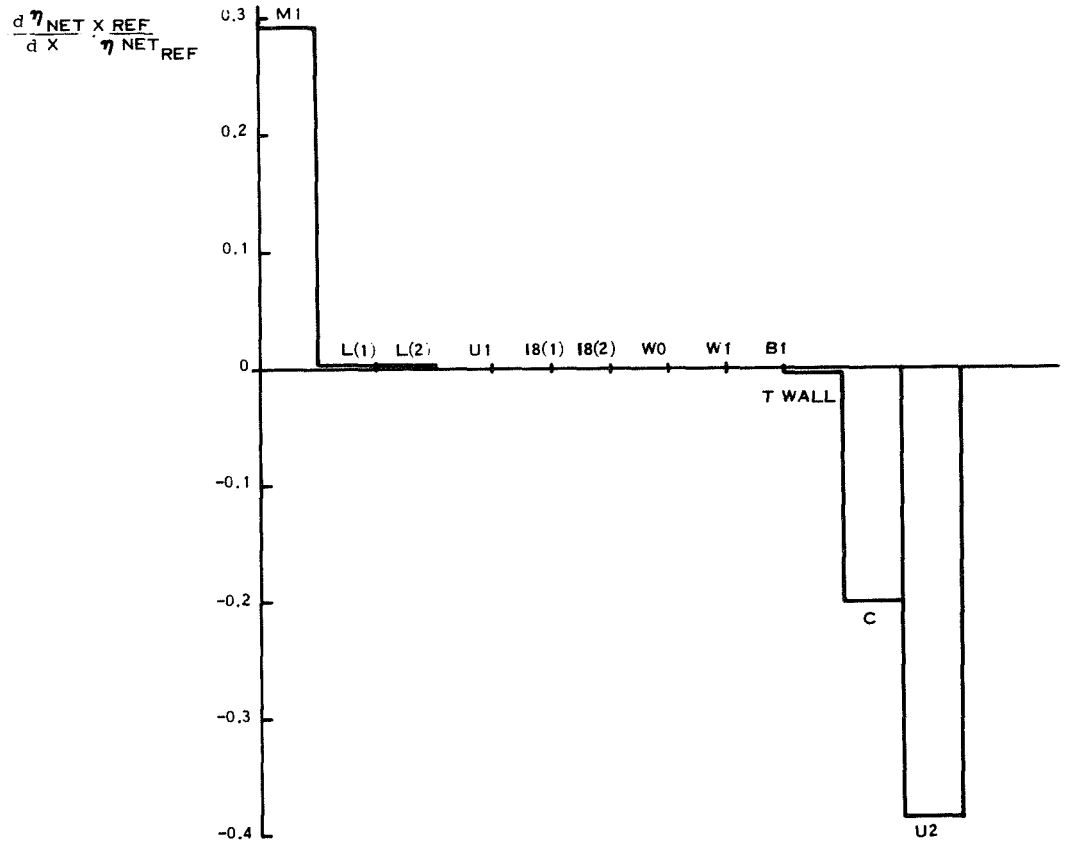

Figure 2-9. Sensitivity Factors for Net Efficiency

It should be noted that the variation of X about X_{ref} probably produces values of η_{net} less than the optimum value presumed associated with the reference base case by adjustment of B_1.

It was initially rather surprising that the wall thickness, t_{wall}, had almost no effect on P_{net} and η_{net}. Since wall thickness has a direct bearing on lithium duct heat transfer to the stator block, and incorporation of methods to suppress wall currents, its effect was investigated further. As seen in Figure 2-10 the principal effects of increasing t_{wall} from one to ten millimeters are to double the reactive power and produce a roughly proportionate increase in copper coil dissipation. These cause significant penalties in capacitor weight and low temperature radiator area.

The decrease in P_{net} and η_{net} are relatively modest, being, of course, directly coupled to P_{coil}.

2.3.2.4 Additional Analyses

In addition to the parameters calculated in the generator and cycle programs as presently written (described in the preceding sections), there is a need to calculate other parameters which are of significant

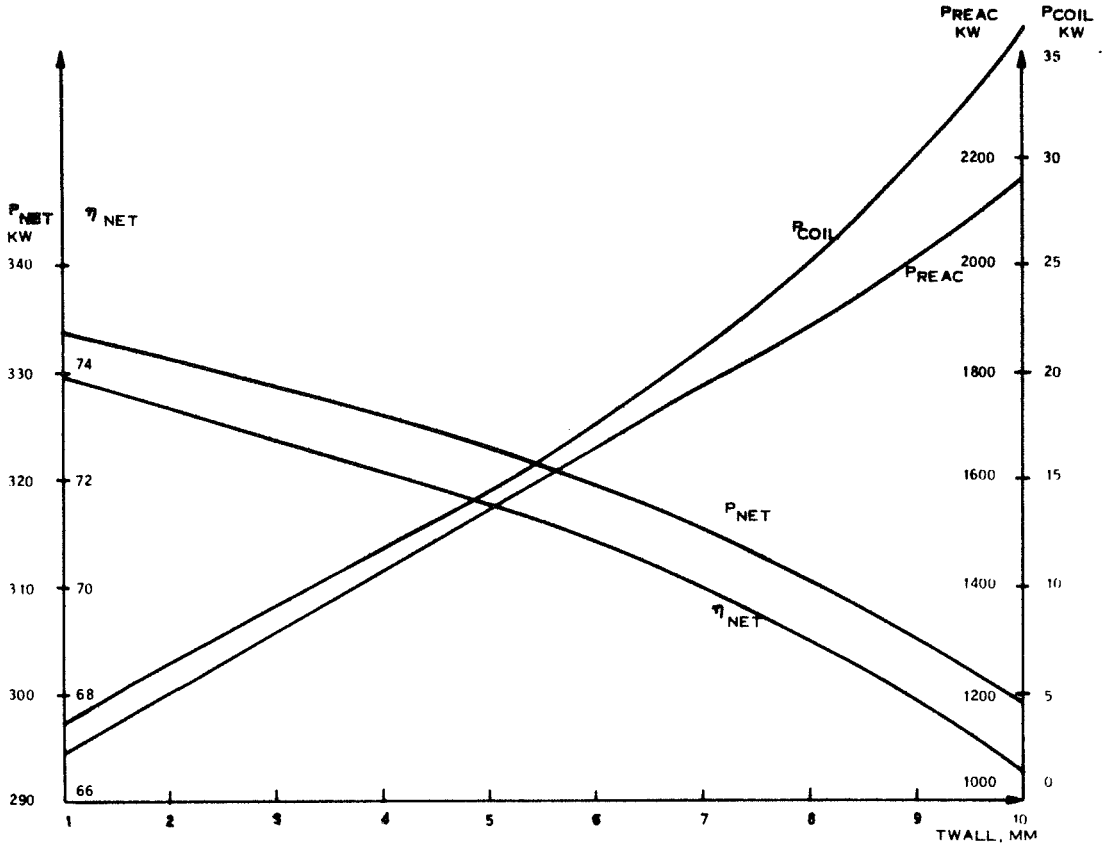

Figure 2-10. Effects of Varying T_{wall} From One to Ten Millimeters

concern to the spacecraft designer. Two which are of immediate importance are the MHD generator winding (copper) weight and the MHD generator stator (iron) weight. Modifications to the computer programs are being made to calculate these values on the bases described below.

2.3.2.4.1 MHD Stator Iron Weight - In the present generator analysis the stator slot height, D_o, is calculated but the total iron height is not. This total height can be identified as D_s and set equal to the sum of $D_o + D^*$ where D^* is the height of unslotted iron. D^* can be calculated explicitly since the net magnetic flux in this region is equal to the compensating pole flux (Reference 5). The iron cross-sectional area can therefore be calculated by setting

$$B_S \geq \frac{\sqrt{2}\,\phi_c}{A} \qquad (1)$$

where: B_S = saturation flux for iron, T

ϕ_c = compensating pole flux, W_b

A = iron area, m^2

B_S is an input to the program; ϕ is calculated by the program; and A is the product of c (channel/stator width, a program input) and D^*, the dimension sought. Therefore, total stator iron height is

$$D_S = D_o + D^*$$

$$D_S = D_o + \frac{\sqrt{2}\,\phi_c}{c\,B_S} \qquad (2)$$

The length of the stator block is

$$L_{Tot} = L_{TW} + L_{IN} + L_{OUT} \qquad (3)$$

where L_{TOT} = total length

L_{TW} = length of travelling wave section

L_{IN} = length of upstream compensating pole section

L_{OUT} = length of downstream compensating pole section.

From the arrangements developed in Appendix I, L_{IN} and L_{OUT} can be estimated quite closely as

$$L_{IN} = w\,5_1 - (x_1 - \frac{w\,2_1}{2}) + w\,2_0 + w\,6_1 \qquad (4)$$

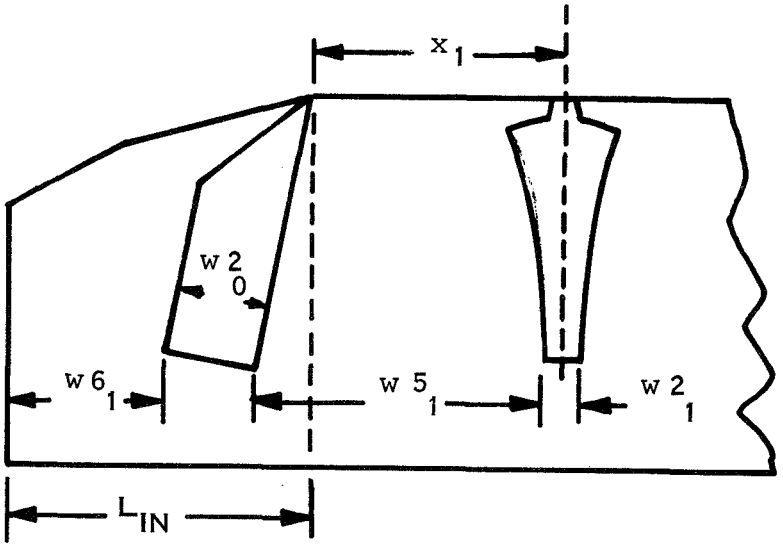

By the same technique

$$L_{OUT} = w\,5_2 - \left(L - x_{K-1} - \frac{w\,2_{K-1}}{2}\right) + w\,2_K + w\,6_2 \qquad (5)$$

The total stator volume then can be estimated by multiplying

$$V_{St} = 2 \times D_S \times c \times L_{TOT} \qquad (6)$$

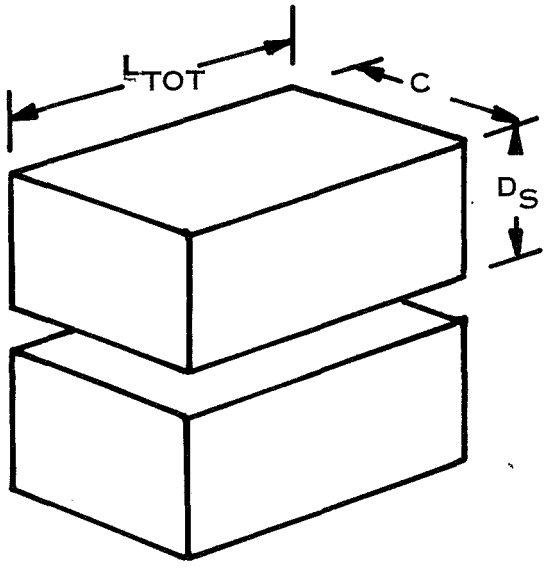

The generator program already calculates the slot area and the slot volume can be calculated by

$$V_{slot} = c \sum_{n=1}^{n=N-1} \left[w\,1_n\,D_n - w\,2_n\,(D_n - D_o)\right] / 3 \qquad (7)$$

for the travelling wave region and

$$V_{end\ slot} = c\ 4\ w_A\ D_o$$

for all four compensating pole slots (assuming a pair at each end of the generator) where

$$w_A = \tfrac{1}{2}\,(w2_0 + w2_N)$$

$w2_o = L_1$, if $L_1 < D_o$

$w2_o = D_o$, if $L_1 > D_o$

$w2_N = L_2$, if $L_2 < D_o$

$w2_N = D_o$, if $L_2 > D_o$

and

L_1 = length of upstream compensating pole

L_2 = length of downstream compensating pole

The iron weight can then be calculated

$$\text{Weight } F_e = \rho_{Fe} \left[V_{st} - V_{slot} - V_{end\ slot} \right]$$

2.3.2.4.2 MHD Generator Winding Weight - In the calculation of MHD generator performance, winding losses are calculated by the use of a winding loss factor, α , which is defined:

$$\alpha = \frac{\text{actual winding loss (including iron loss)}}{\text{solid fill DC loss of slot portion of coils}}$$

The numerical value of α has been assumed to be 3 as a typical value. Since the copper coil windings of the MHD generator are estimated to weigh more than 1000 pounds (Reference 3), an explicit relationship between copper weight and actual winding loss is needed in order that a tradeoff between copper weight and auxiliary cooling system weight can be made. In Reference 4 the coil loss factor, α , was broken down as follows:

a. slot filling factor: 0.8

b. ac/dc resistance ratio: 1.4

c. external conductor dc resistance is equal to slot dc resistance

d. The iron core loss is assumed to be negligible.

Thus, $\alpha = 1.4 \frac{R_i}{0.8} + 1.0 \frac{R_i}{0.8} = 3 R_i$

where R_i is the solid-fill slot dc resistance.

If the total current is I then the total winding loss is calculated as αI^2R_i. With α broken down it is possible to determine the external conductor resistance penalty when reducing the conductor weight as follows. Let resistance of external copper by γ times the above-assumed value so that $\gamma = 1$ corresponds to $\alpha = 3$ with the values assumed under items a and b above retained unchanged. Then:

$$\alpha = 1.75 + \frac{\gamma}{0.8}$$

which is plotted in Figure 2-11.

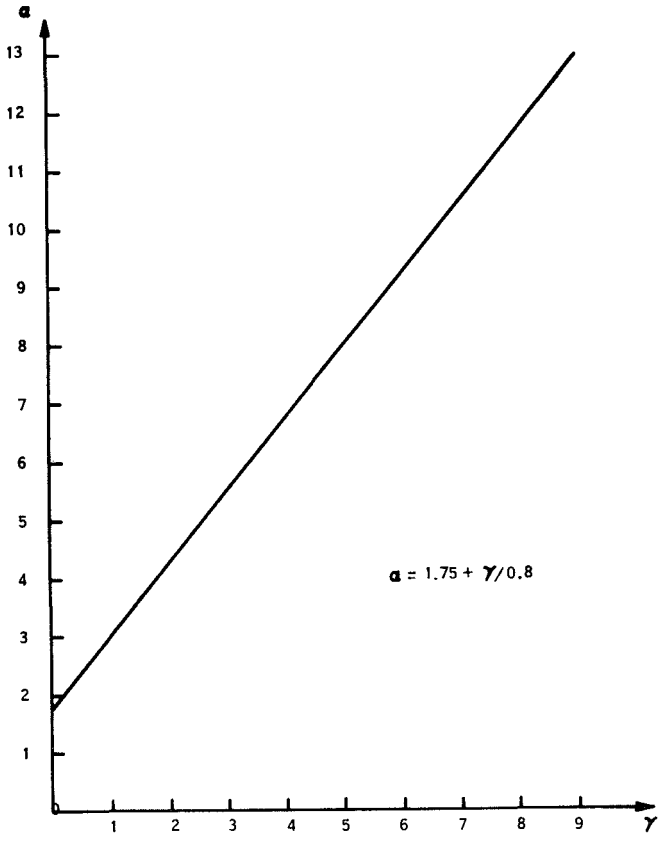

Figure 2-11. Relation Between Coil Loss Factor, α, and External Conductor Resistance Factor, γ.

We now wish to express copper weight as a function of γ.

Since resistance

$$R = \rho \frac{\ell}{A}$$

where

ρ is copper resistivity

ℓ is conductor length

A is conductor area

It will be necessary to determine ℓ and A for the slot conductor and for the external conductor. For the slot conductor the volume of the copper and hence the weight can be obtained explicity in the program. The cross sectional area of a particular slot is given by

$$A = \left[W1 \cdot D - W2 \cdot (D-D_o) \right] /3 \qquad (8)$$

where

$$D_o = 0.75\ D_{k-1}$$

and

D_{k-1} is the sharp point depth of the last inboard slot (see Figure 2-12)

and since the length is c, the volume for the travelling wave region slots is given by

$$Vol_{cu} = \frac{.8c}{3} \sum_{n=1}^{n=N-1} W1_n \cdot D_n - W2_n\ (D_n-D_o) \qquad (9)$$

The copper volume for the compensating pole slots is calculated

$$V_{end\ Cu} = 0.8\ c\ \ 4\ w_A\ \ D_o$$

where

$$w_a = \frac{w2_o + w2_N}{2}$$

and

$w2_o = L_1$, if $L_1 < D_o$

$w2_o = D_o$, if $L_1 > D_o$

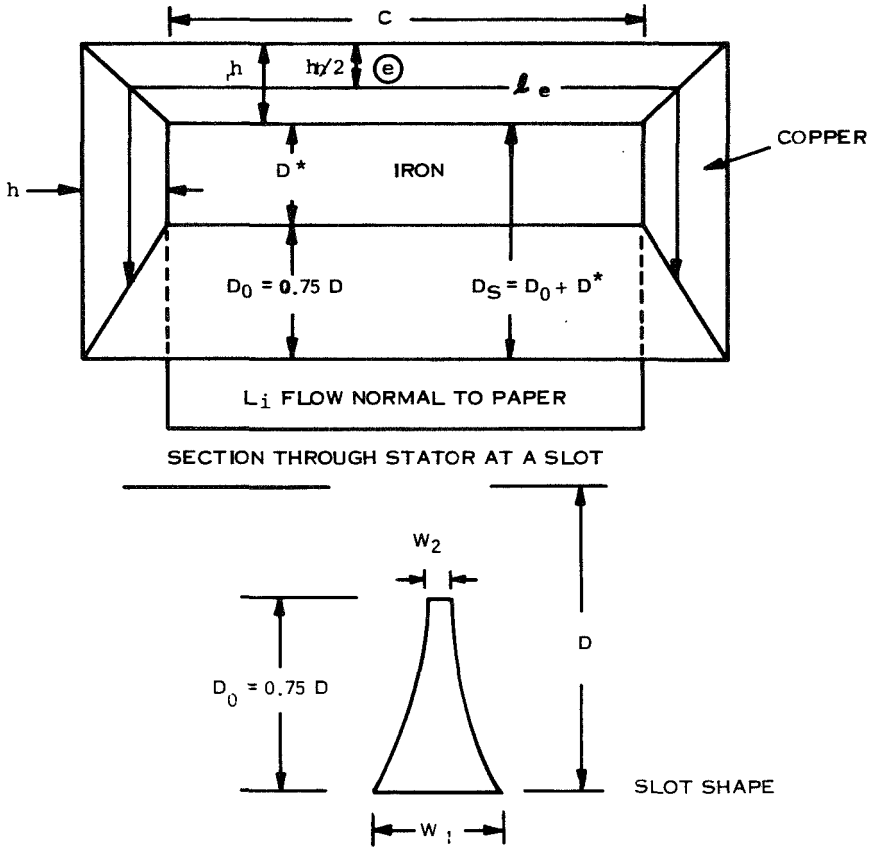

Figure 2-12. MHD Stator Winding Geometry

$$w2_N = L_1, \text{ if } L_2 < D_o$$

$$w2_N = D_o, \text{ if } L_2 > D_o$$

and

L_1 = length of upstream compensating pole

L_2 = length of downstream compensating pole

In both cases the sum is multiplied by 0.8 as this is the packing fraction of copper in a slot.

We can express the volume of the copper external to a particular slot as

$$Vol_{cu} = W_e \ \ell_e \ \ h \qquad (10)$$

where

W_e is the external width of the copper winding

ℓ_e is the external length of the copper winding

h is the height of the copper winding

By inspection of the generator program results, it appears reasonable to set

$$W_e = 5/3\ W1 \tag{11}$$

(a better approach might be to set W_e equal to the corresponding sector width, but this requires more inspection). This will reasonably fill the outside face of the stator block with copper.

We can estimate the length of the copper as

$$\ell_e = c + 2\ (\tfrac{1}{2}\ D_o + D^* + h/2 + h/2)$$

$$\ell_e = c + D_s + D^* + 2h \tag{12}$$

The first term ($\frac{1}{2}\ D_o$) in the bracket is considered a reasonable estimate in the cross-section shape-changing region on leaving the slot.

We can now write the corss-sectional area as

$$A_e = 5/3\ W1 \cdot h$$

and since

$$\frac{\ell_e}{A_e} = \gamma \frac{\ell_s}{A_s} = \gamma \frac{c}{A_s}$$

We can now write

$$\gamma \frac{c}{A_s} = \frac{c + D_s + D^* + 2h}{5/3\ W1\ h}$$

solving for h yields

$$h = \frac{A_s\ [c + D_s + D^*]}{5/3\ W1 \cdot \gamma c - 2A_s} \tag{13}$$

Putting (11), (12) and (13) into (10) yields

$$Vol_{cu_n} = (c+D_s+D^*+2h_n)(5/3Wl_n)\left[\frac{A_{s_n}\ (c+D_s+D^*)}{5/3\ Wl_n\ \gamma c-2A_{s_n}}\right] \qquad (14)$$

This equation yields the volume of the copper external to the nth slot.

The total volume of copper is then

$$Vol_{cu} = Vol_{cu_o} + Vol_{cu_N} + \sum_{n=o}^{n=N} Vol_{cu_n}$$

The first two terms are necessary to include all compensating pole slot copper for the case of two compensating pole slots at each end.

These equations will be used in programming the weight calculations into the generator code.

2.4 POWER SYSTEM SYNTHESIS

Before attempting the design and analysis of the baseline MHD powerplant, two basic questions had to be considered in order to synthesize a rational MHD power system. These two questions are the method of system startup and whether a one-loop or two-loop system is used.

2.4.1 MHD POWER SYSTEM STARTUP

As indicated in Section 1 of this report, MHD power system startup and control techniques are to be analyzed in Phase II of this study. It has been recognized, however, that some preliminary evaluation of startup techniques must be made early in Phase I in order that the arrangements and design layouts may include all the components such as valves, lines, and reservoirs which will be needed for plant operation. Therefore, discussions of MHD system startup techniques were held with Dr. Elliott, the principal scientist developing this system, during the first quarter of this study and a startup technique was identified.

2.4.1.1 Startup Requirements

Operation of this MHD power system requires steady two-phase flow in the MHD nozzles with phase separation at the generator entrance. The cesium needs heat from the lithium to boil and expand down the nozzle; the lithium needs the mechanical force of the expanding cesium to be accelerated down the nozzle. Thus, neither fluid stream can pass through the nozzles alone. In addition, some of the kinetic energy imparted to the lithium by the cesium in the nozzles is needed to pump the lithium. The first conclusion is, therefore, that the two streams must start into the nozzles together.

The NaK/N_2 test system (see Subsection 2.3) has been started by simultaneous injection of the two fluids into the empty nozzle with stable flow being achieved in seconds. The NaK/N_2 system is a cold test system, with the compressed energy of the nitrogen providing the kinetic energy rather than heat taken from the NaK stream. In the hot Li/Cs system the simultaneous injection startup can be expected to work only if there is enough thermal energy in the lithium stream to cause boiling and expansion of the cesium at once, sufficiently to establish self-sustaining flow conditions. Some reduced temperature level may suffice to start system flow; however, lacking any detailed analysis or test data to support that conjecture, the second conclusion is drawn with regard to startup technique - namely, that the two fluids will be injected at or near normal operating temperatures.

If the two fluids are to be injected into the nozzles for startup and steady state is to be achieved in seconds, the nuclear reactor heat source must already have been taken critical and warmed up since the nuclear reactor can probably be designed to take a large power swing in a matter of seconds but requires hours to be taken critical and warmed up. It is reasonable to assume that aerospace nuclear safety considerations will require that the reactor does not go critical until the spacecraft is in a high, long-life orbit. Thus, a third conclusion about startup techniques can be drawn, startup injection will not take place until the spacecraft has been in orbit for hours. A reasonable time limit of five hours can be estimated by allowing one hour for orbit ephemeris verification and four hours for achieving criticality and warmup.

The two fluids of the MHD system, lithium and cesium, have melting points of 357^{o}F and 84^{o}F, respectively. Since the spacecraft will be in orbit at least one hour before the lithium begins to receive heat from the reactor, the lithium must be preheated before launch to prevent fluid freezing. The cesium, with a much lower freezing point, poses far less a problem. In order to fill the lithium system on the launch stand it will have to be preheated and then filled with hot molten lithium to assure complete fill. Thus, a fourth conclusion about startup is drawn, the lithium systems will be preheated and launched hot. The results of previous studies such as SNAP-50/SPUR indicate that preheat to 500^{o}F should be adequate. The cesium system should receive enough heat from the lithium system to preclude freezing in it, although some way to warm up the radiator is needed.

The general requirements for the startup techniques can then be summarized:

a. Startup will be by simultaneous injection of lithium and cesium into empty nozzles

b. The two fluids will be injected at their normal operating temperatures

c. Startup will take place only after about five hours in orbit

d. The lithium system will be preheated to 500^{o}F at launch.

2.4.1.2 System Arrangement for Startup

Figure 2-13 is a schematic diagram of the MHD fluid system with the necessary valves and other equipment added so that the system can be started. The entire system can be evacuated through the four evacuation and fill connections with the following valve lineup:

LV-1	open
LV-2	open
LV-4	open to reactor bypass line
CV-1	open
CV-2	open

After the system is evacuated, LV-1, LV-2, CV-1 and CV-2 are closed and the cesium and lithium sections are filled through their respective fill connections. Preheating of the lithium piping and the reactor can be accomplished by circulating hot inert gas through their insulating jackets.

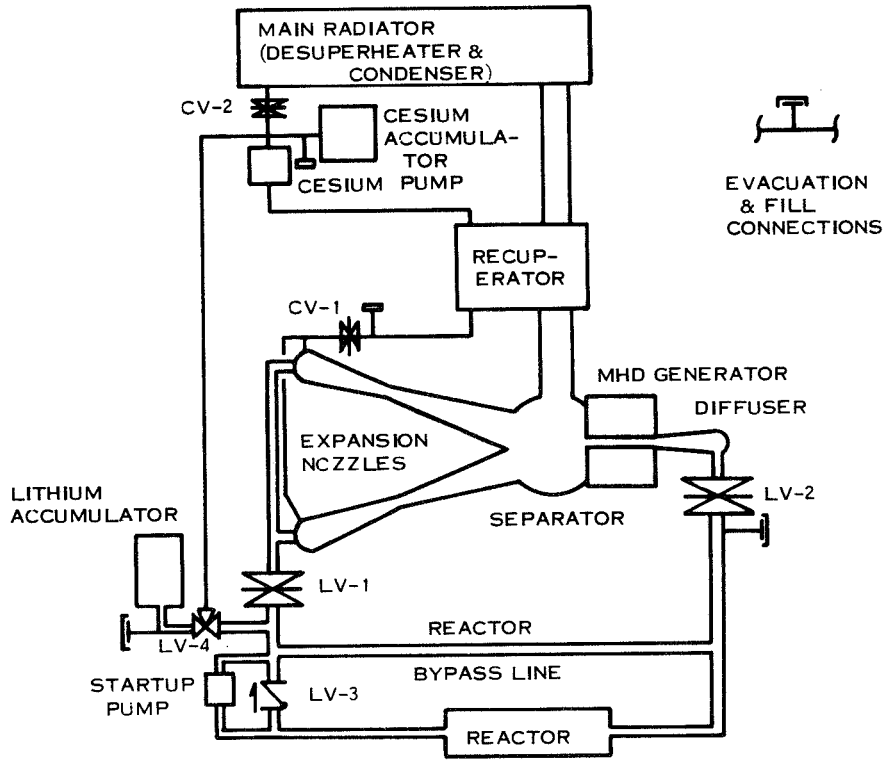

Figure 2-13. MHD Fluid System Schematic

After reaching a safe orbit, the reactor is taken critical and warmed up, circulating the lithium at a low flow rate with the battery-powered startup pump located in parallel with check valve LV-3. The lithium flow path is normal through the reactor section but is reverse through the reactor by-pass line. The cesium system is stagnant but shares the same insulated enclosure with all of the lithium system except the reactor and is, therefore, warmed up by radiated and conducted heat. System pressures are maintained by controlling the gas pressure acting on the two bellows type accumulators; the two accumulators absorb the fluid expansion volume during warmup.

When operating temperatures are reached, accumulator gas pressures are increased and valves LV-1 and CV-1 open, injecting the two fluids into the nozzles. After appropriate intervals, valves LV-2 and CV-2 are opened to complete the normal flow paths. The startup pump is secured and valve LV-4 switches the lithium reservoir connection over to the cesium pump suction to minimize the containment pressure requirements during long term operation. Cesium and lithium makeup to the system for leakage or volume expansion due to creep enter the system at the cesium pump suction controlled by accumulator gas pressure.

2.4.2 SHUTDOWN AND RESTART

The reference mission has a coast period halfway to Jupiter and the Jupiter orbit operation, both of which have a nominal ten percent power demand (See Paragraph 2.1.1). There is no estimate of the overall operating efficiency of the MHD power system when operating at ten percent output. If operation at ten percent rated output is achievable only at extremely low system efficiency, it might be worthwhile to shut down the MHD loop and operate the reactor at low power using an alternate conversion system, e.g., thermoelectrics, to generate power.

For the reference mission the low power demand time is 120 + 17 = 137 days out of 50 + 160 + 120 + 270 + 17 = 637 days or ~22 percent of the mission (more with longer time in Jovian orbit). If an alternate conversion system with equivalent efficiency (~ 7 to 8 percent) is available and the MHD loop can be shut down, the reactor core life required can be reduced to

$$\frac{500 + 0.08(137)}{637} \times 100 = 80\%$$

of the life required for continuous operation at rated power. Even without examining the possible difficulties of MHD loop shutdown

and incorporation of a second power conversion system, the ~20 percent saving in core design life does not seem a strong incentive for design change.

To restart the MHD system after an in-space shutdown, it is assumed that the original startup conditions must be restored in shutting down the system. Two shutdown approaches were considered. In the first, an exhaust connection would be added to the diffuser downstream of the MHD generator. The system would be shutdown by closing valves, LV-1, LV-2, CV-1, and CV-2 and opening the exhaust port simultaneously. The hot fluids in the nozzles and vapor spaces would boil off into space and, with the exhaust port reclosed, the system would again be ready for startup if the accumulators contained sufficient fluid inventory. This method was rejected for many reasons, namely:

a. The spacecraft would receive a large impulse from fluid exhaust just after its attitude control system (the thrusters) was shut down.

b. The exhausted liquid metal may contaminate spacecraft surfaces

c. The lithium and cesium reservoirs would require additional inventory for restart capability.

The second shutdown technique considered was to first close valves LV-1 and CV-1 and simultaneously lower the gas control pressures on the accumulators (the lithium accumulator is assumed to be valved back to the reactor by-pass line). The generator electrical circuits are then opened to minimize flow resistance and fluid momentum is relied upon to drive as much fluid as possible back into the accumulators. When sufficient fluid has been drawn out of the nozzle, generator and vapor spaces, valves LV-2 and CV-2 are closed to complete the shutdown. Successful execution of this type shutdown would require careful control and judgement of its feasibility would require extensive analysis. In the scope and context of this study and in view of the modest core life reduction to be attained, this analysis was not considered worthwhile.

If the MHD system cannot be shutdown but cannot operate stably at the low power levels required by the mission, it may be necessary to include a means of dissipating excess power. If this had to be taken out as electrical power, it would require a power flattening radiator of ~100 ft^2 (assuming radiator operation at 1000 to 1200°F). A radiator of this size would add less than four feet to the length of the spacecraft. As an alternate the power flattening resistor

could be located in the lithium flow path so that it would be liquid cooled. This second approach would probably be the lighter and would not add to spacecraft length. Since neither power flattening design would impose serious design penalties on the spacecraft, it is considered safe to assume stable part power operation pending detailed analysis.

2.4.3 ONE OR TWO-LOOP SYSTEM

2.4.3.1 Reactor Loop Arrangement

In order to provide the MHD loop with 1600 to 2200°F lithium, a fast spectrum, lithium-cooled reactor such as SNAP-50 is a logical choice. With such a reactor, the reactor coolant may be used directly in the MHD loop or an intermediate heat exchanger may be used to separate the reactor and MHD loops. Figure 2-14 shows the basic MHD cycle diagram with the reactor piped directly into the MHD loop. The movement of fluids in the MHD loop depends on the cesium stream receiving thermal energy from the lithium when the two streams are mixed in the nozzles. The boiling and expanding cesium then imparts kinetic energy to the lithium stream, part of which is converted to electrical energy in the MHD generator and part of which is converted to pumping pressure in the diffuser to circulate lithium back through the reactor and to the nozzles. The optional bypass shown in Figure 2-14 can be used to divert some of the lithium flow around the reactor in order to obtain a lower reactor pressure drop or a more compact reactor.

If the reactor loop is separated from the MHD loop by a heat source heat exchanger as shown in Figure 2-15, an additional pump is needed to circulate the lithium through the reactor loop.

The incentives for use of a separate reactor loop are:

a. The reactor pressure vessel may be designed for a containment pressure lower than the 150 psia typical of the MHD loop

b. Ingestion of cesium by the reactor, with subsequent bubble formation, is precluded

c. Activated coolant is kept away from the payload

The incentives for a one-loop system are:

a. The system is simpler and lighter

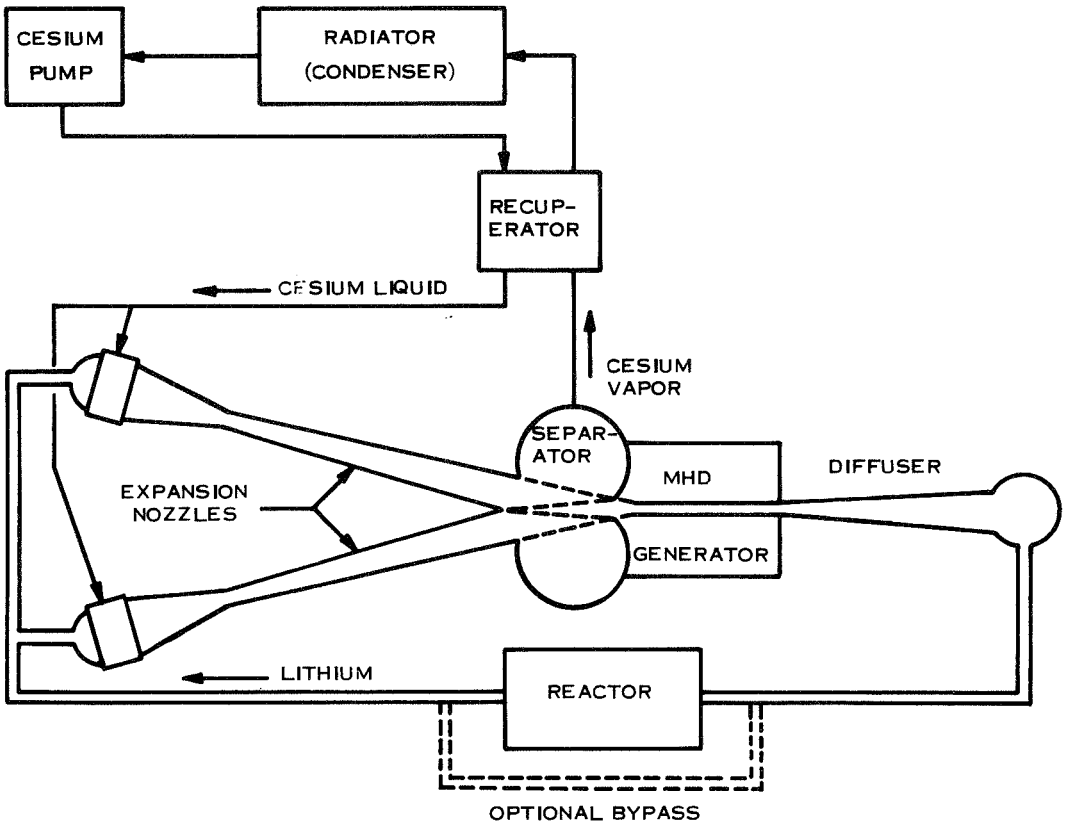

Figure 2-14. MHD Cycle Diagram

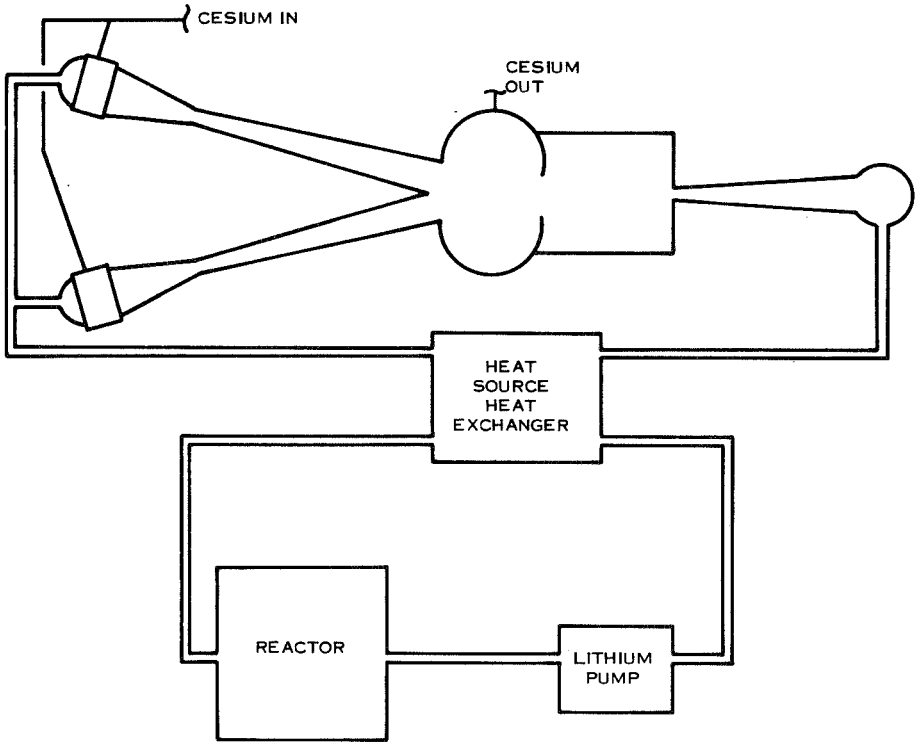

Figure 2-15. MHD Loop with Separate Reactor Loop

b. Lithium can be circulated for prestart warmup (see startup discussion in Paragraph 2.4.1) using just one pump. A two-loop system could also use just one pump if all lithium in the MHD circuit is left stagnant and warmed by conducted heat

c. Only one lithium accumulator is needed

d. No reactor coolant pumping is needed once the system is started.

2.4.3.1.1 Containment Pressure - The weight penalty associated with designing the reactor for MHD pressure may be approximated as follows:

a. Assume a domed cylindrical pressure vessel of 12-inch diameter and 40-inch length made of Cb-1Zr. This size and material are typical of the MHD type reactor

b. Assume that the reactor pressure vessel would have a minimum design pressure of 50 psia

c. Assume that the reactor pressure vessel design stress for 20,000 hour operation is 1000 psi. This low design stress is quite conservative for temperatures below $\sim 2000^{o}F$. More advanced alloys of Cb can provide much greater creep strength.

Calculating a minimum vessel wall thickness:

$$t = \frac{Pr}{\sigma} = \frac{50 \text{ psi} \times 6 \text{ in.}}{1000 \text{ psi}} = 0.3 \text{ in.}$$

Design for 150 psia would revise this to:

$$t = \frac{150 \text{ psi} \times 6 \text{ in.}}{1000 \text{ psi}} = 0.9 \text{ in.}$$

An increase of 0.6 inch in wall thickness.

The surface area of the vessel is about 1500 square inches and the wall material density is 0.32 pounds per cubic inch, so the weight increase would be:

$$1500 \text{ in}^2 \times 0.6 \text{ in} \times 0.32 \text{ lb/in}^3 \approx 300 \text{ lb.}$$

Since the weight penalty is only about 300 pounds even with the conservative material and design stress selection, the additional complexity and weight of a separate reactor loop, pump and heat source heat exchanger would constitute a greater penalty. In weight comparison, the heat source heat exchanger alone, with one side designed for 150 psi, would weigh almost as much.

2.4.3.1.2 Cesium Bubbles - The second-listed incentive for a two-loop system is to keep cesium bubbles out of the reactor. The fluid conditions at the MHD generator inlet behind the upstream diffuser are such that all remaining cesium should be dissolved. If any bubbles do still exist at the generator exit they may still dissolve when static pressure is increased from ~40 psia to ~ 150 psia in the downstream diffuser. If still not dissolved, any cesium bubbles would more likely follow the bypass line (~ 80 to 85 percent of the flow) rather than enter the reactor line (~ 15 to 20 percent of the flow). Lastly, if the reactor core is of one-pass design, as is most likely, cesium bubbles would collect in the inlet or outlet plenum rather than in core fluid passages where they would be swept through. Collection of cesium vapor bubbles in one of the reactor fluid plena is not expected to have a significant effect on reactor performance.

2.4.3.1.3 Coolant Activation - Radioactivity in the reactor coolant may reach areas near the payload in a one-loop system which may cause radiation damage. In the lithium-cooled MHD reactor two basic sources of coolant radioactivity can be identified - leakage of fission products from reactor core fuel elements into the coolant and irradiation of the coolant itself during its passage through the reactor. An assessment of fuel element leakage has not been made yet but coolant irradiation has been considered. Three nuclear reactions are of interest:

$$Li^6 + n \longrightarrow H^3 + \alpha$$

$$Li^7 + n \longrightarrow Li^8 + \gamma$$

$$Cs^{133} + n \longrightarrow Cs^{134} + \gamma$$

The first of these reactions poses no high radiation threat to equipment since tritium is a weak β emitter. However, the Li^6 reaction does produce non-reactive, non-condensible helium, which can buildup in the system. The tritium will react with lithium to form LiH. The Li^6 reaction can be suppressed by using lithium coolant which is at least 99.9 percent the Li^7 isotope. Such Li^7 enriched lithium is available; natural lithium is already ~93 percent Li^7. The Li^7 reaction is of interest because of the Li^8 isotope

formed emits a very high energy β ($\sim$ 13 Mev). However, its half-life of 0.85 seconds is so short that most should decay before coming past the shield; this delay time can be extended by including an enlarged section in the reactor outlet line. In addition, the MHD loop itself keeps the lithium from approaching the payload.

2.4.3.1.4 Cs^{134} Activity - The Cs^{133} (n, γ) Cs^{134} reaction produces two isomers, the 2.9 hour half-life Cs^{134m} and the 2.3 year Cs^{134}. These nuclides can be formed by irradiation in the reactor of the cesium dissolved in the lithium stream (natural cesium is 100 percent Cs^{133}). In order to evaluate this activity, one must have good knowledge of:

a. Cesium flow distribution (residence time in reactor, residence time near thepayload, mass flow rates, and total inventory

b. Definition of the reactor neutron flux by neutron energy level for each reactor region of interest (annulus, inlet plenum, core, and outlet plenum)

c. Cs^{133} cross section data for each energy level of interest

d. Location of sensitive components with respect to the activated cesium.

Since the system, and especially the reactor, designs are both conceptual at this time the cesium activation was analyzed by using the best available information, making estimates, where necessary, and trying to keep the analysis conservative.

Figure 2-16 depicts the mass/flow/time model which was set up to represent the cesium distribution in the system. The flow distributions and cesium inventory are based on initial baseline values. The radiation source is identified as the lowest of five radiator sections and it was assumed that 10 pounds of the calculated 31 pound cesium inventory of that radiator section would be one foot away from the payload. The cesium flow through the reactor will vary with system operating temperature and pressure (varying cesium solubility in lithium); the calculated baseline design value was used.

The Cs^{133} (n, γ) cross sections which were used are listed in Table 2-8. The 29-hour Cs^{134m} was assumed to undergo 100 percent decay to 2.3 year Cs^{134} with the emission of a 0.13 Mev γ . The

DESIGN LIFE = 14,000 HRS

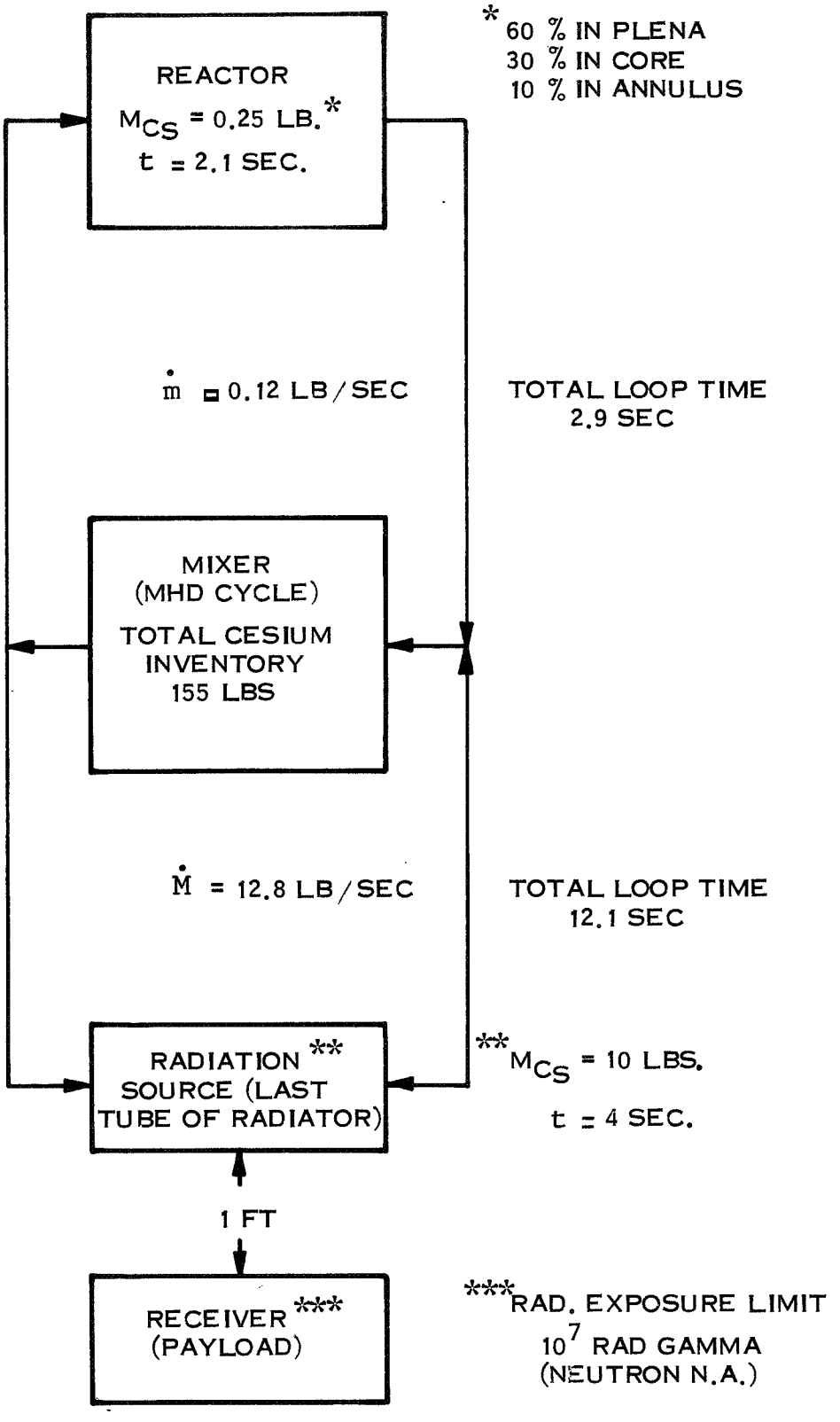

Figure 2-16. MHD Cesium Mass/Flow/Time Model

TABLE 2-8. CESIUM - 133 (n, γ) CROSS SECTIONS

Thermal Neutrons

Production of 2.9 hour Cs^{134m}		σ = 2.6 barns
Production of 2.3 year Cs^{134m}		σ = 29 barns

0.215 ev $\leq$ En $\leq$ 10 kev

$\overline{\sigma}$(n γ) $\approx$ 5 barns	Cs^{134m}	σ = 0.5 barns
	Cs^{134}	σ = 5 barns

En = 20 kev

	Cs^{134m}	σ = 0.09 barns
	Cs^{134}	σ = 1 barn

Estimates for High E_n Range

E_n	σ 134m (barns)	σ 134 (barns)
10 to 100 kev	0.04	0.4
0.1 to 0.4 Mev	0.007	0.07
0.4 to 1.4 Mev	0.001	0.01
1.4 to 10 Mev	0.0004	0.004

decay of Cs^{134} was assumed to be:

a. 30 percent 0.3 Mev β^- decay to Ba^{134} followed by Ba decay with the emission of a single 1.75 Mev γ.

b. 70 percent 0.68 Mev β^- decay to Ba^{134} followed by Ba decay with the emission of a pair of γ of energies 0.8 and 0.6 Mev.

The activation rate in the reactor

$$A = \int_E \int_V \Sigma (E)\ \phi (E, \vec{r})\ d V\ d E$$

requires a knowledge of the reactor neutron fluxes in various regions of the reactor. Since the MHD reactor design is still conceptual the following values were used:

FLUX (nv)

Group	Core	Annulus	Plena
1	7×10^{13}	10^{13}	4×10^{12}
2	1.4×10^{14}	2×10^{13}	10^{13}
3	1.4×10^{14}	3×10^{13}	10^{13}
4	10^{14}	5×10^{13}	3×10^{13}
5	1.5×10^{13}	4×10^{13}	8×10^{13}
Thermal	10^{10}	5×10^{11}	2×10^{13}

These flux values are expected to be somewhat conservative for the MHD reactor since they are more closely related to reactor designs with a softer neutron energy spectrum

The reactor average group fluxes were weighted for the time spent in the various reactor regions (see model in Figure 2-16), and

the average group fluxes ϕ g were used to calculate activated nuclei per second

$$A = V_{Cs} \sum_{g=1}^{6} \Sigma g \phi g$$

where

$$\Sigma g = \sigma g \frac{\rho_{Cs} N}{A_{Cs}}$$

A_{Cs} = molecular weight of cesium

$$\rho_{Cs} = \frac{M_{Cs}}{V_{Cs}}$$

M_{Cs} = mass of cesium

For Cs^{134m} this results in

$$A^m = 3.5 \times 10^{13} \text{ nuclei per sec.}$$

For Cs^{134} this, and Cs^{134m} decay, gives

$$A^{134} = 3.8 \times 10^{14} \text{ nuclei per sec.}$$

Since Cs^{134} has a half-life of 2.3 years its decay is not negligible, so correcting for decay and the 10/155 fraction which is close to the payload, the number of activated nuclei contributing dose to the payload is calculated.

$$N = 2.6 \times 10^{20} (1 - e^{-\lambda t})$$

where

N = nuclei contributing dose

λ = Cs^{134} effective decay constant

t = time

The following dose-to-flux conversion factors were used for the emissions of interest:

0.6 Mev	$C = 8.4 \times 10^5$ photons/cm^2sec per R/hr
0.8 Mev	$C = 6.5 \times 10^5$ photons/cm^2sec per R/hr
1.75 Mev	$C = 3.5 \times 10^5$ photons/cm^2sec per R/hr

Assuming a point source geometry with no attenuation by the pipe walls or structure the dose as a function of time was calculated:

$$D(t) = \frac{1}{C} \int_0^t \frac{(3.6 \times 10^3)\, N \lambda}{4 \pi r^2} \, d t$$

to get the following results:

Time (Hrs)	Total Integrated Dose (R)
5,000	2.5×10^5
10,000	9.2×10^5
15,000	1.9×10^6
20,000	3.3×10^6

The highest dose rate resulting from these calculations, 3.3×10^6R, is about one-third of the allowable payload dose. The dose rate at nominal design life, 14,000 hours, is about 15 percent of allowable. In view of the conservatisms of the calculation, Cs^{134} activation and consequent irradiation of the payload is not considered a severe enough problem to warrant changing to a two-loop system. It should be noted that Cs^{134} activation should be reappraised in the future, when more specific information is available, to verify this conclusion.

2.5 SELECTION OF INITIAL DESIGN PARAMETERS

In order to provide a basis on which to conduct configuration trade-offs and design comparisons, a set of initial design parameters for the baseline design was drawn up. This analysis is based on a 300 kWe net output system with an 1800°F nominal inlet temperature and assumes:

a. Only 15 percent of the lithium flow is heated in the reactor with the bulk of the flow passing directly from the diffuser to the nozzle inlet through the bypass line

b. The vapor conditions at the recuperator exit correspond to 50 percent of the lithium vapor condensing in the recuperator with the remaining 50 percent assumed to condense in the de-superheater section of the main radiator.

2.5.1 SYSTEM CONDITIONS

Figure 2-17 presents the temperature, pressure, flow rate and energy transfer conditions existing in the powerplant primary system while Figure 2-18 shows the corresponding conditions in the shield-reflector cooling loop and the auxiliary cooling loop. Symbols are defined as follows:

T = Fluid temperature in °F

P = Fluid pressure in psi

W = Fluid flow rate in lbs/sec

Q_t = Thermal energy transfer in kW

Q_e = Electrical energy transfer in kW

Q_r = Nuclear radiation energy transfer in kW.

The encircled numerals are the cycle station designations used in the computer analysis (see Appendix II).

The previously mentioned assumption that only 15 percent of the lithium flow passes through the reactor results in a 120°F reactor coolant temperature rise compared to the average 18°F temperature change in the lithium circuit. The lower reactor flow rate reduces the reactor feed line piping size required and the pressure drop within the reactor. The total pressure drop of ten psi assumed in the cycle calculations is arbitrarily evenly divided between the reactor and piping.

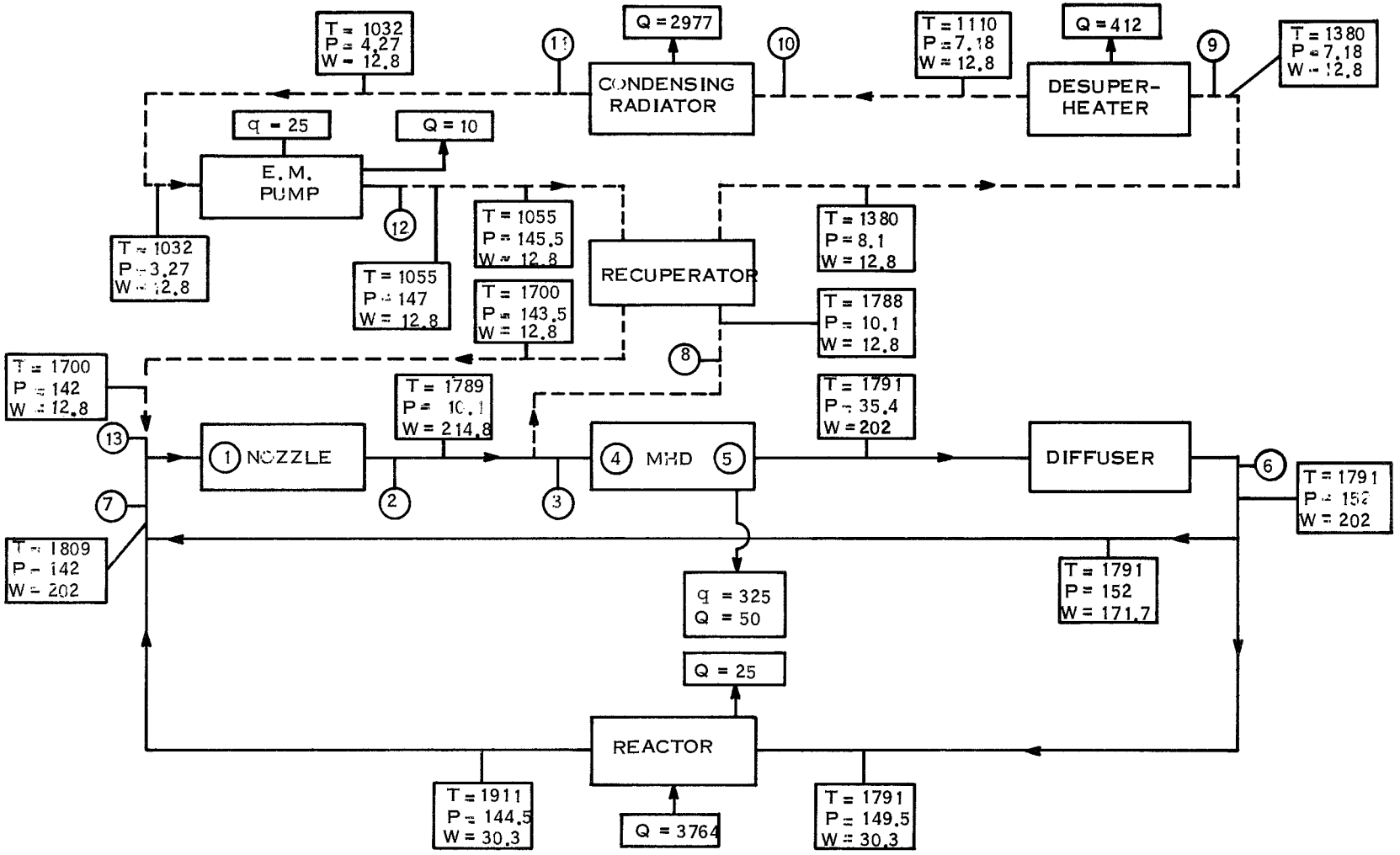

KEY

T = TEMPERATURE IN °F
P = PRESSURE IN LBF / IN^2
W = MASS FLOW RATE IN LBM / SEC
Q = THERMAL ENERGY IN KWT
q = ELECTRICAL ENERGY IN KWE

Figure 2-17. Liquid Metal MHD Power System (Initial Baseline Design)

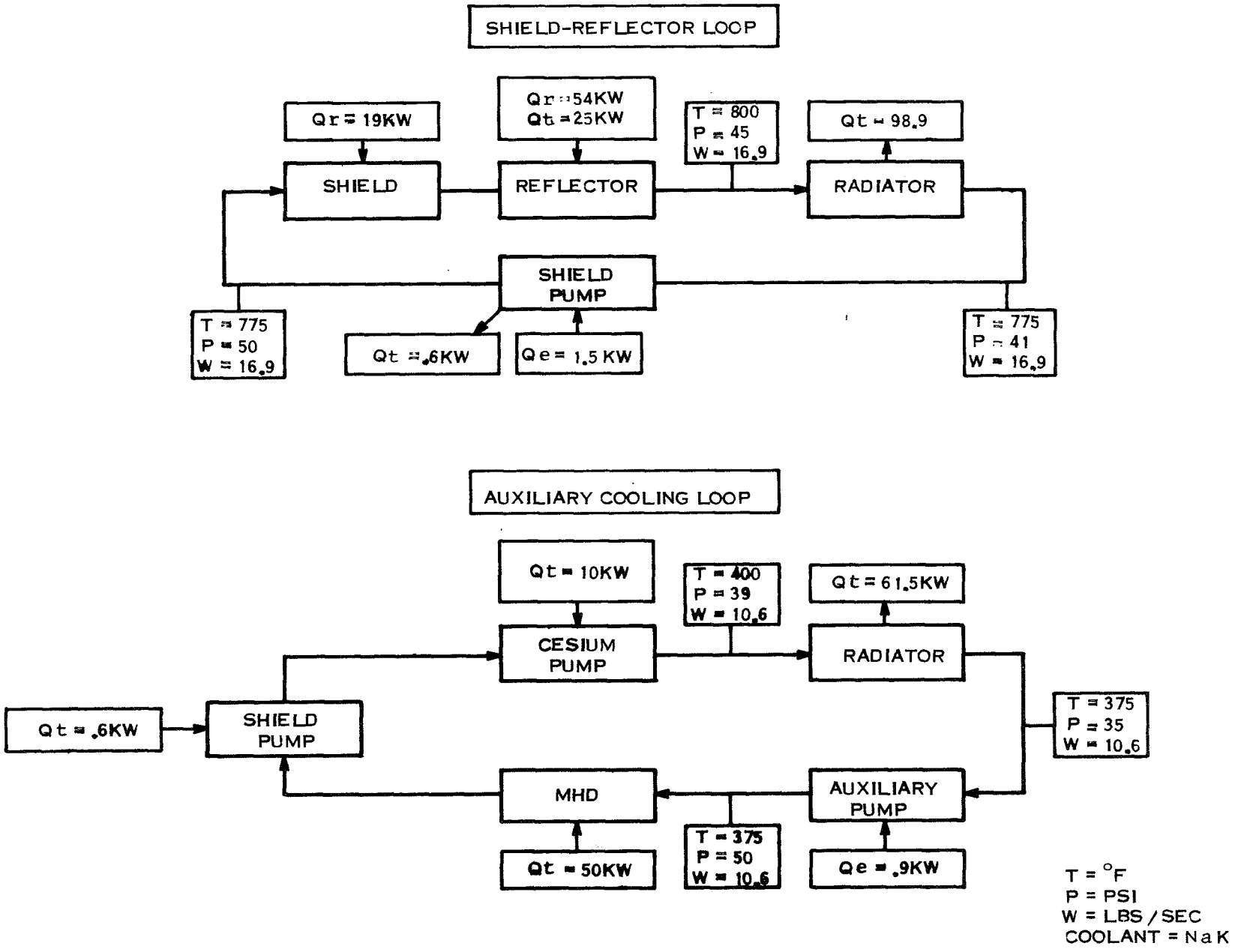

Figure 2-18. Auxiliary Loops for Liquid Metal MHD Power System

The JPL cycle program calculates a station nine fluid temperature of 1672°F on the assumption that all the lithium vapor entering the recuperator condenses. Actually, only a portion of lithium will condense, so the conditions shown on Figure 2-17 arbitrarily assume 50 percent of lithium condenses in the recuperator with the remaining 50 percent condensing in the desuperheater.

The fluid pressure at the pump inlet was arbitrarily decreased to 3.27 psi to provide a one psi ΔP in the liquid cesium return lines of the condensing radiator. Later investigations may show that this return line ΔP can be provided by a portion of the ΔP assigned to the condensing radiator by the cycle calculation assumptions.

The apportioning of the pressure drops to the recuperator and the attached vapor and liquid piping is arbitrary and subject to modification if so indicated by the layout investigations.

The secondary cooling loops were arbitrarily separated into an 800°F shield-reflector cooling loop and a 400°F auxiliary cooling loop. Forty percent of the electrical power to the shield and cesium pumps is assumed to be removed by the cooling circuits while the MHD cooling requirement is estimated at 50 kW.

The net electrical power is the MHD output less the cesium, shield and auxiliary pump requirements. For the conditions shown on Figures 2-17 and 2-18, this net power is 297.6 kW. The corresponding thermal energy input to the reactor is 3764 kW which does not include the estimated nuclear radiation deposited in the shield (19 kW) and the reflector (54 kW). The 54 kW reflector heat can be eliminated if a radiatively cooled reactor is chosen. The calculated cycle efficiency is ~ 7.95 percent.

2.5.2 RADIATOR AREAS

The radiators defined to date, their temperatures and areas are as follows:

COMPONENT	TEMPERATURE (°F)	AREA (FT^2)
Condensing Radiator	1032 to 1110	1285
Desuperheater	1110 to 1380	132
Shield Radiator	800	60
Auxiliary Radiator	400	190

The condensing radiator and the desuperheater are actually two sections of one radiator with a combined area of ~1420 square feet in a triform configuration. The radiators still to be evaluated are the main PC radiator, the payload and thruster PC radiators and the generator excitation radiators.

2.5.3 CONDENSING RADIATOR

The basis for the condensing radiator is the design described in Table 2-9.

TABLE 2-9. INITIAL BASELINE DESIGN CONDENSING RADIATOR

Area	1285 square feet
Panel Length	11 feet
Primary Duct Width	3.86 inches
Primary Duct Height	2.51 inches
Vapor Chamber Output Diameter	0.75 inch
Total Number of Vapor Chambers	3400
Vapor Chamber Weight	2440 pounds
Primary Duct Weight	594 pounds
Total Weight	3034 pounds

2.5.4 DESUPERHEATER

The desuperheater input conditions are as follows:

Heat rejection = 412 kW

T_{in} = 1380°F

T_{out} = 1110°F

from which the effective radiating temperature of 1235°F and the radiating area of 132 square feet are calculated. By area ratio, the weight of the vapor chambers is determined to be 250 pounds. The vapor duct design is based on 12.8 pounds per second of vapor flow with straight configuration, the duct weight is calculated as 86 pounds. The total desuperheater weight is 336 pounds.

2.5.5 RECUPERATOR

The recuperator is assumed to be a bundle of tubes with external axial

fins arranged in triangular array within a cylindrical shell. The high pressure liquid cesium flows inside the tubes with the high temperature-low pressure vapor flowing countercurrently down the finned exterior of the tubes. A summary of the recuperator characteristics is given in Table 2-10.

TABLE 2-10. RECUPERATOR CHARACTERISTICS

Overall diameter (in.)	17
length (in.)	32
Weight (lbs. wet)	395
Finned Tubes	
Number	160
Length (in.)	24
I.D. (in.)	.25
Wall thickness (in.)	.03
Fins	
Number/tube	24
Height (in.)	.45
Thickness (in.)	.02
Efficiency	.695
Shell Thickness (in.)	.10
Temperatures (^{o}F)	
Vapor inlet	1788
Vapor outlet	1380
Liquid inlet	1055
Liquid outlet	1700
Log-mean ΔT	181
Pressure Drops (psi)	
Liquid	.15
Vapor	2.0
Flow Rates, Liquid and Vapor, lbs/sec.	12.8

2.5.6 LITHIUM LOOP

The lithium loop consists of the reactor feed lines and the reactor bypass line with conditions as shown in Table 2-11.

TABLE 2-11. LITHIUM LOOP CHARACTERISTICS

	Reactor Feed Line	Bypass Line
Flow rate, lbs/sec	30.3	171.7
Length, feet	22	7
Pressure drop, psi	5	10
Pipe ID, inches	2.6	3.3
Pipe wall thickness	0.20	0.25
Pipe weight	144.5	73.5
Fluid weight	22.5	11.5
Total weight	167	85

The estimated inventory in the piping, accumulator and reactor is 130 pounds. Assuming a spherical accumulator configuration, the required accumulator diameter is 15 inches, and the accumulator wall thickness is 0.6 inches. The resulting weight of the wet accumulator is 145 pounds. The total weight of the lithium piping loop including the accumulator is 397 pounds.

2.5.7 CESIUM LOOP

The cesium loop consists of the following components:

a. Vapor feed lines to desuperheater

b. Liquid return lines from condensing radiator

c. Liquid piping from pump to recuperator and from recuperator to nozzle

d. Cesium pump

e. Cesium accumulator

f. Recuperator (previously defined).

The characteristics of each of these components is discussed separately below.

2.5.7.1 Cesium Vapor Feed Lines

The cycle pressure drop of three psi between stations 8 and 9 is arbitrarily divided as two psi across the recuperator and one psi in the

vapor ducting in the diagram of Figure 2-17. However, in sizing the vapor ducting, a two psi drop is needed to achieve reasonable duct sizes. Modification of cycle conditions and/or recuperator sizing will be required to provide this necessary pressure drop.

The desuperheater - condensing radiator is assumed to have five bays in parallel from a fluid flow viewpoint, with the bays stacked axially down the spacecraft length. Each bay is approximately 11 feet in axial length. The vapor duct is assumed to vary in diameter along its length, decreasing in diameter at the front end of each bay. The desuperheater duct in each bay draws off vapor from the main duct at the front end of each bay. The front end of the first bay is assumed to be at the recuperator exit so only 80 percent of the vapor enters the main vapor duct with the remainind 20 percent being diverted into the first bay desuperheater. A run of 11 feet carries the vapor duct to the front end of the second bay where another 20 percent of the vapor is diverted, etc. Therefore, the vapor duct is 44 feet long with the first 11 feet carrying 80 percent of the total vapor flow, the second 11 feet 60 percent, etc. The inner duct diameter of each 11 foot length is as follows:

First section is 8.7 inches

Second section is 7.8 inches

Third section is 6.7 inches

Fourth section is 5.2 inches

The wall thickness needed for the largest diameter section is 0.35 inches from an internal pressure consideration but meteoroid armor requirements exceed the pressure requirements. A duct wall of 0.083 inches surrounded by a bumper shield 0.055 inches thick is required to achieve a 0.95 non-penetration reliability. The resultant duct weight is 304 pounds and the bumper weight is 236 pounds for a total vapor duct weight of 540 pounds. The separation between the duct and bumper is 0.625 inches.

2.5.7.2 Cesium Liquid Return Lines

The liquid return lines run the full length of the desuperheater - condensing radiator, about 55 feet. Although the cycle calculation does not provide pressure drop for this pipe section, a ΔP of 1 psi was assumed. The liquid return line can be tapered or staggered in diameter similar to the vapor duct but the constant diameter pipe was assumed. The calculated pipe I.D. required is 1.42 inches and the pipe wall thickness is determined by meteoroid protection requirements. A pipe wall of 0.072 inches with a bumper thickness of 0.048 inches at a separation distance of 0.6 inches is needed for a 0.95 non-penetration probability. The

resultant pipe weight is 143 pounds, the bumper weight is 177 pounds and the liquid cesium weight is 142 pounds for a total weight of 462 pounds for the return lines.

2.5.7.3 Cesium Pump-to-Nozzle

The pump to recuperator section of cesium piping is assumed to be five feet long with a pressure drop of 1.5 psi. The resultant pipe diameter is 1.25 inches and its total weight is 13.5 pounds.

The recuperator-to-nozzle section of cesium piping is assumed to be two five-foot long sections, one to each nozzle, each having a pressure drop of 1.5 psi. The resultant pipe diameters are 1.0 inch and the combined weight of both sections is 20 pounds.

2.5.7.4 Cesium Pump

The cesium pump flow rate is 12.8 pounds per second and the required pressure rise is 145 psi. A dc pump providing these conditions weighs 85 pounds while an ac pump weighs an estimated 218 pounds.

2.5.7.5 Cesium Accumulator

The cesium inventory in the piping, recuperator, radiator, etc., is estimated at 155 pounds. The volume change from room to operating temperature is approximately 20 percent so a spherical accumulator is estimated to have a diameter of 11 inches. Assuming a wall of thickness of 0.125 inches, the total weight of the accumulator plus included cesium is 50 pounds.

2.5.7.6 Cesium Loop Summary

A weight summary of the cesium loop including the recuperator previously described is as follows:

Vapor feed lines	540 pounds
Radiator return lines	462 pounds
Piping, pump-to-nozzle	34 pounds
Pump	85 pounds
Accumulator	50 pounds
Recuperator	395 pounds
Total	1566 pounds

2.5.8 SECONDARY LOOPS

There are two secondary loops as shown in Figure 2-18; a shield-reflector cooling loop and an auxiliary cooling loop. The shield-reflector cooling loop is assumed to operate at 800°F, the upper temperature limit for the lithium hydride material in the shield. The auxiliary cooling loop is limited to 400°F which is dictated by the desired operating temperature for the MHD generator magnetic and electrical materials. The two loops are described separately below. If a radiatively cooled reactor is used, the reflector cooling portion of this loop can be omitted.

2.5.8.1 Shield-Reflector Loop

The heat dissipation load for this loop is 98 kW. The radiator required is estimated to be 60 square feet in area and weighs 224 pounds. These values are based on an assumed area limit of 0.7 and a corresponding weight multiplier of 1.3.

The shield loop piping is assumed to be five feet in length and the NaK coolant flow rate is 16.9 pounds per second. The optimum pipe diameter is calculated to be 1.92 inches, so the piping weight is 12 pounds for an assumed pipe wall thickness of 0.06 inches. The associated accumulator is estimated to weigh 35 pounds.

The total coolant pressure drop is estimated as 9.6 psi so the weight of a dc pump is 30 pounds while an ac pump weighs 75 pounds.

The total weight of the shield-reflector cooling loop is 302 pounds.

2.5.8.2 Auxiliary Cooling Loop

The auxiliary cooling loop cools the electrical components in the system, the MHD generator, the cesium pump and the shield loop pump. The MHD generator cooling load of 50 kW consists of 15 kW from the coil windings plus an estimated 35 kW thermal loss by the lithium stream. In both the cesium and shield loop pumps, the cooling load is assumed to be 40 percent of the electrical input power. The remaining 60 percent is deposited in the fluid being pumped. Of course, the total electrical input power of the auxiliary loop pump is deposited in the NaK coolant of the auxiliary loop.

The area of the auxiliary radiator is estimated as 190 square feet and its weight as 705 pounds for an assumed area limit of 0.7 and a corresponding weight multiplier of 1.3.

The length of the auxiliary loop piping is assumed to be 10 feet. Its

optimum pipe diameter is 1.7 inches and its total weight is 19 pounds. The weight of the corresponding accumulator is estimated as 45 pounds.

The total pressure drop in the auxiliary loop is approximately 15 psi. A dc pump providing the necessary flow rate and pressure rise weighs 33 pounds and a similar ac pump weighs 82 pounds.

The total weight of the auxiliary cooling loop is 802 pounds.

2.6 CONFIGURATION TRADEOFFS

Since the MHD spacecraft is expected to be rather long with many heavy pieces of equipment, configuration tradeoffs were conducted to determine the most attractive design arrangement.

2.6.1 GENERAL ARRANGEMENT GUIDELINES

To begin, some general conclusions were drawn about spacecraft arrangement:

a. The ion thruster subsystem includes a significant amount of electronic control and power conditioning equipment. Since this equipment will have radiation exposure limits equivalent to the payload, the payload and thruster subsystem should be located together at one end of the spacecraft with the nuclear reactor at the opposite end.

b. The ion thruster subsystem has a characteristic diameter of about ten feet in order to provide adequate mounting area for the thrusters. A nuclear reactor of the type needed here is of small diameter, no more than about three feet. Since a radiation shadow shield will be needed between the reactor and the payload/thruster area, the minimum shield diameter and weight will be obtained by locating the shield next to the reactor.

c. Working in a ten foot diameter envelope, the MHD power system requires a total radiator section of some 60 to 70 feet long. Since separation of the reactor and payload/thruster area minimizes shielding thickness requirements, the radiators shall be located in a continuous section between the reactor and the payload/thruster area.

d. The MHD power generating equipment is linked to the nuclear reactor by at least two lithium coolant pipes and is connected to the payload/thruster area by the main power output cables. In addition, the MHD power generating equipment apparently does not include any items which are especially sensitive to radiation. Since the power output cables can be kept small (MHD raw output is ~ 300 Hz, ~ 600 Vac), the preferred location for the MHD equipment is just behind the radiation shield, near the reactor.

With these guidelines as the starting point, the preliminary arrangement studies and configuration tradeoffs were conducted.

2.6.2 MHD EQUIPMENT BAY

The MHD nozzle assembly, the MHD generator, the excitation capacitors, the recuperator, and other closely related equipment are to be located in one section or bay. Some of these items, such as the MHD generator and nozzle assembly, must be located next to one another in order to function. Others should be close together for efficient design; for example, the excitation capacitors should be close to the MHD generator to minimize the length and, consequently, the I^2R losses of the connecting cables which carry the large exciting currents which run from the capacitors to the generator and back. (The MHD generator exciting current is about four times greater than its output power current).

Arrangement of the MHD bay was studied to determine the minimum diameter envelope which could contain this equipment so that if it is located just behind the radiation shield, the shield subtended angle (and weight and volume) would be minimized. The MHD nozzle assembly was first laid out using dimensions taken from the computer analysis of the baseline system. A 40-inch nozzle length was assumed since the JPL investigators indicated that extension beyond this length was not worthwhile. The downstream diffuser half-angle can vary from three degress to five degrees; a three degree half-angle was assumed in order to calculate the longest diffuser.

Using the nozzle assembly as the basis, the key piping and component items identified and sized in Subsections 2.4 and 2.5 were arranged to establish the MHD equipment envelope size. Figure 2-19 shows an arrangement which uses a single recuperator; Figure 2-20 shows an arrangement which uses two recuperators, one for each side of the nozzle. In both cases, the cylindrical segments flanking the diffuser are available for capacitor location providing more than the estimated three cubic feet required, an exposed surface which can reject $\sim$1500W of heat, and a simple interface to insulate the capacitors from the hot MHD equipment. Aside from the capacitors, the MHD stators and pump windings are the only items in the MHD bay which do not operate at $\sim 1800^{\circ}F$. It was therefore assumed that the MHD bay would be insulated on the outside surface of the envelope with the insulation envelope also providing micrometeoroid protection. The internal components (MHD stators, etc.) which do not run at high temperature would be internally insulated and provided with a piped cooling system. The insulated exterior surface of the MHD bay can then be used as the mounting surface for this auxiliary cooling system.

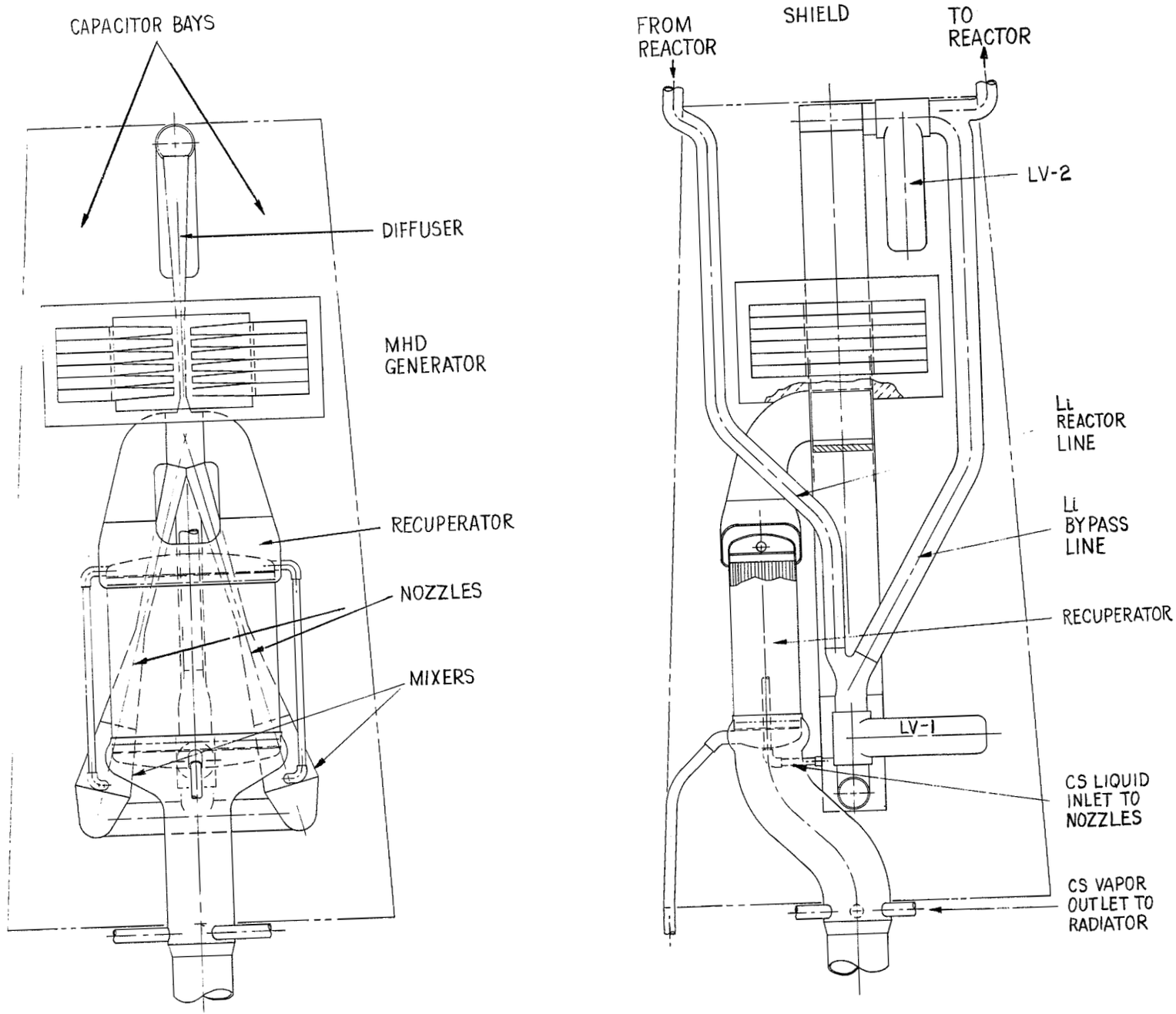

Figure 2-19. MHD Equipment Arrangement with One Recuperator

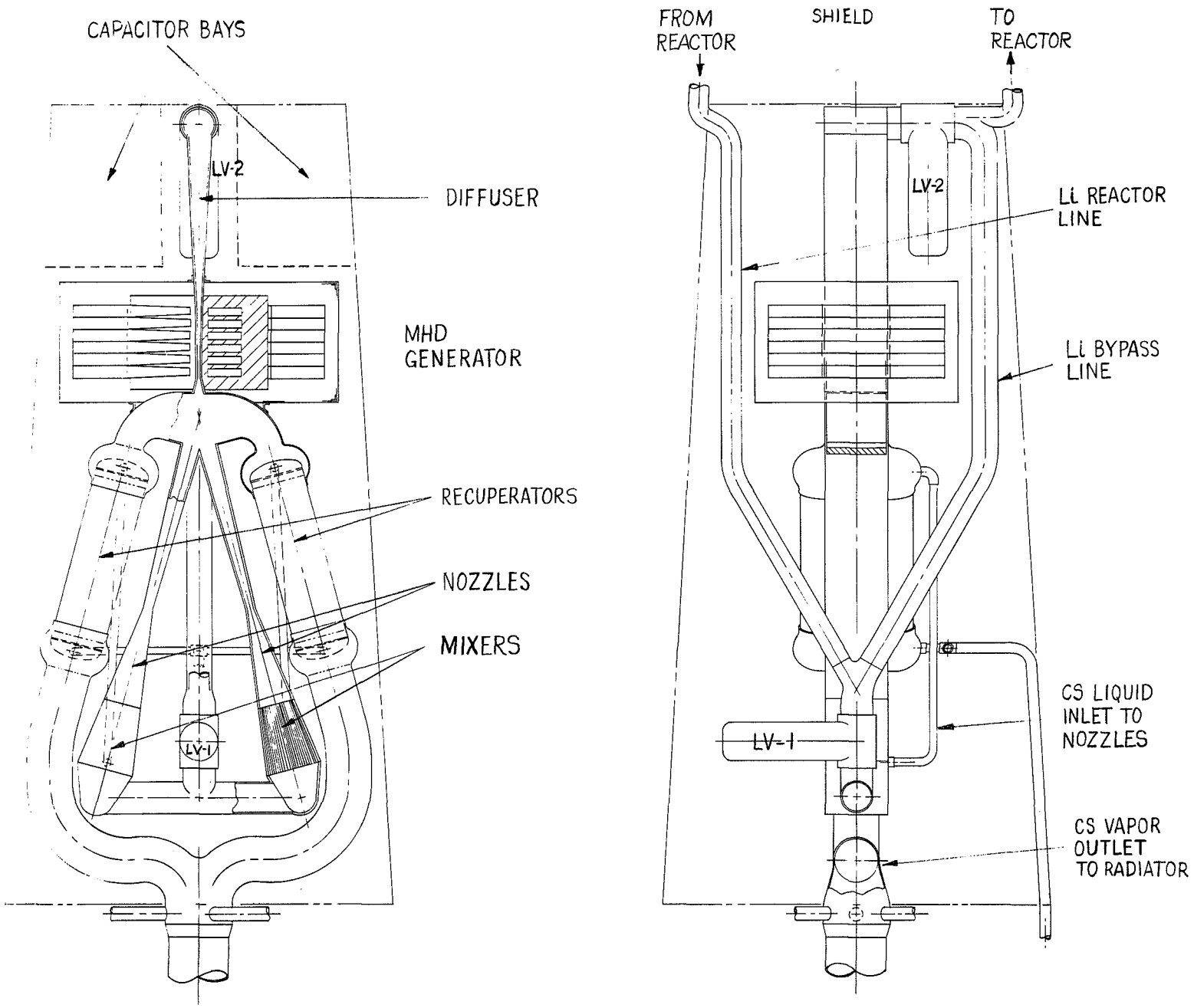

Figure 2-20. MHD Equipment Arrangement with Two Recuperators

The arrangements shown in Figures 2-19 and 2-20 show that the MHD equipment can be encased in a cone frustum about ten feet long with upper and lower diameters of 44 inches and 58 inches. These diameters can be reduced somewhat by canting the MHD nozzle assembly and using a single recuperator or relocating the dual recuperators.

2.6.3 SPACECRAFT STRUCTURE

2.6.3.1 Candidate Configurations

Based on the MHD equipment arrangement possibilities which were available, five general configurations for the MHD spacecraft were drawn up. Since the Thermionic Spacecraft Study found that a cylindrical or conical radiator was lighter than a triform radiator (Reference 6), configurations with conical radiators were considered here even though the study guidelines specify a triform radiator.

Configuration No. 1 (Figure 2-21) uses a conical radiator with the radiation shield shadow projected to full diameter (ten foot nominal, nine and one-half foot actual) at the top of the payload bay. In this configuration, as in the other four, a 190 square foot secondary radiator is assigned and the MHD equipment is assumed to be located inside this radiator. In Configuration No. 1, the MHD bay is a bit slender with upper and lower diameters of 36 inches and 53 inches, but has extra length at 16.4 feet so it is reasonable to assume that all MHD equipment could be arranged in this bay.

Configuration No. 2 (Figure 2-22) differs from No. 1 only in that the MHD equipment bay is relocated down near the payload instead of just behind the radiation shield. This relocation might be made to reduce launch loads imposed on the main radiator or to move MHD equipment to a lower radiation region if the use of radiation sensitive components is found necessary.

Configuration No. 3 (Figure 2-23), using a conical/cylindrical radiator, projects the radiation shield shadow to full diameter about halfway down the spacecraft. This shield angle covers an envelope behind it which accommodates the MHD by configurations discussed in the preceding sections.

Configuration No. 4 (Figure 2-24) projects the same shield angle but with a triform radiator and a triangular shield and MHD equipment bay. This size and shape MHD bay should accommodate all the equipment.

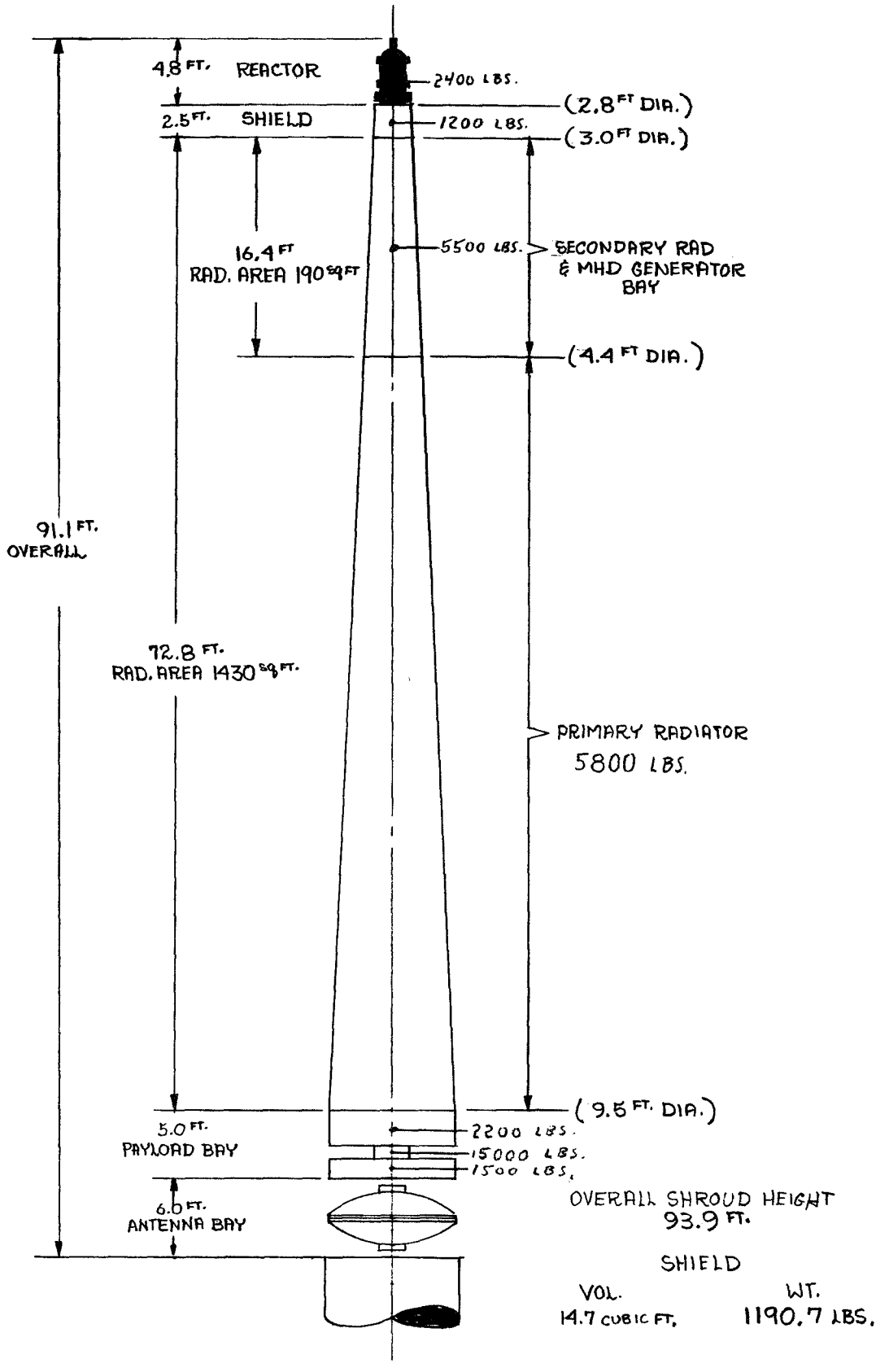

Figure 2-21. MHD Spacecraft Configuration No. 1, Conical Radiator

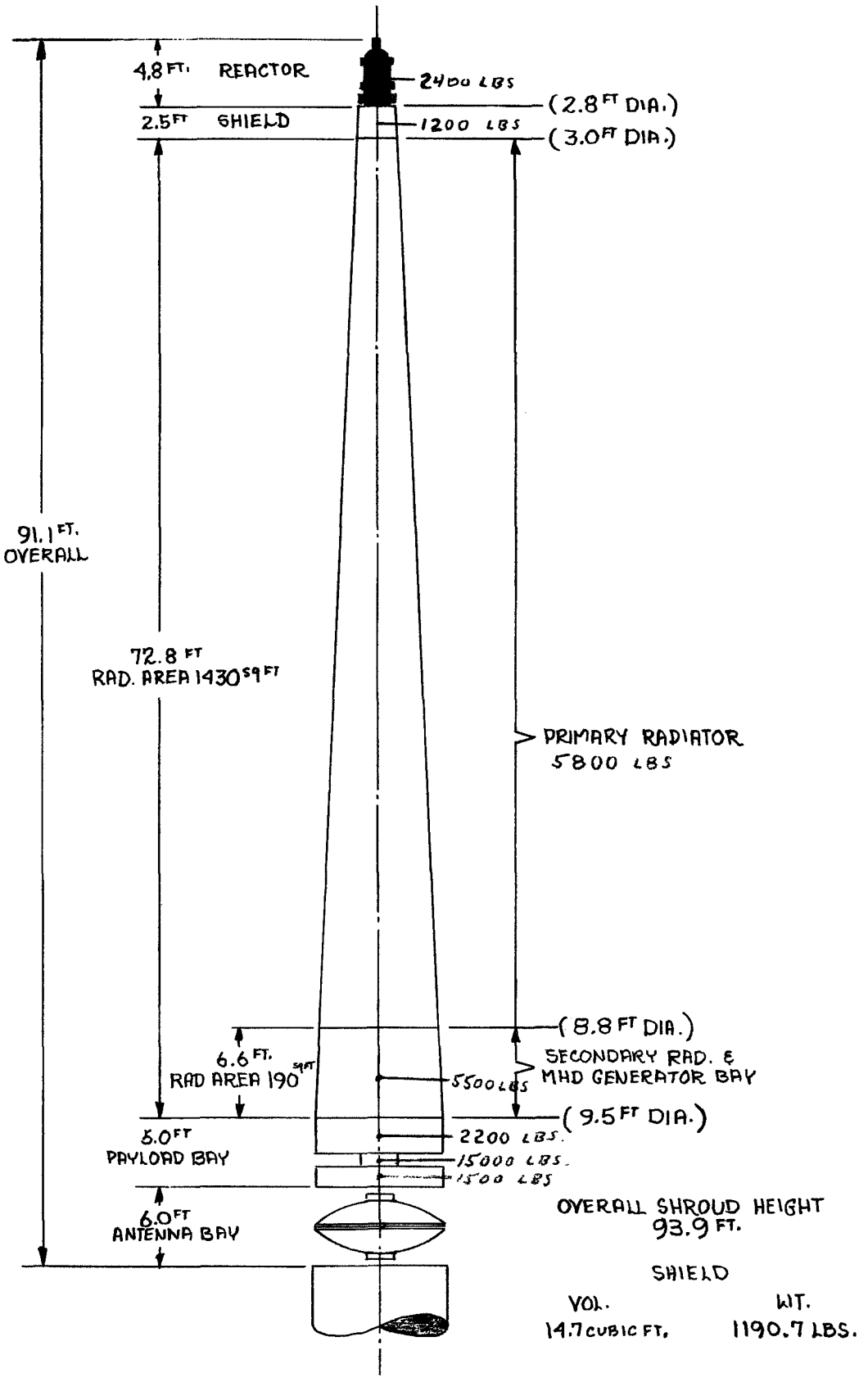

Figure 2-22. MHD Spacecraft Configuration No. 2, Conical Radiator

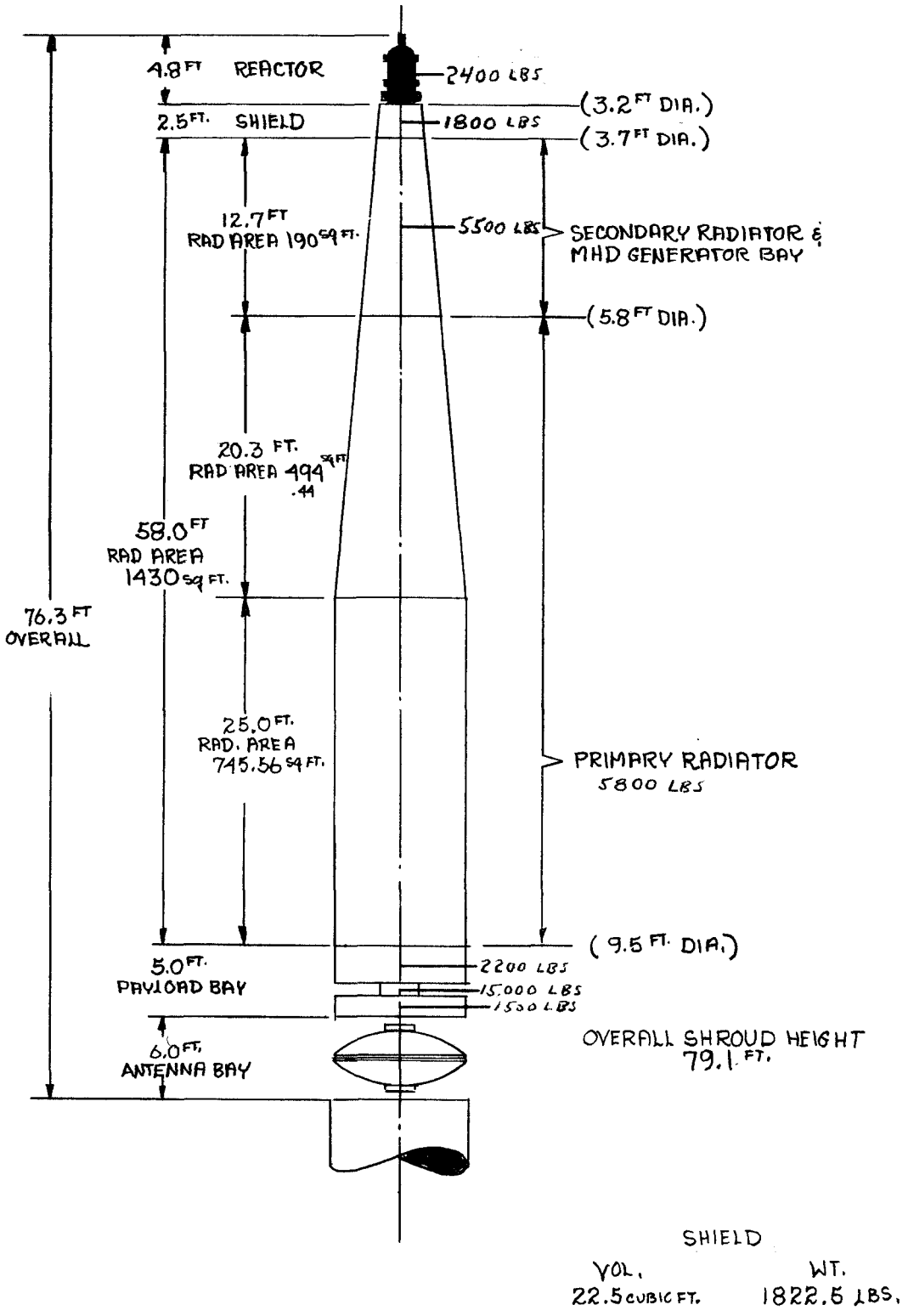

Figure 2-23. MHD Spacecraft Configuration No. 3, Conical and Cylindrical Radiator

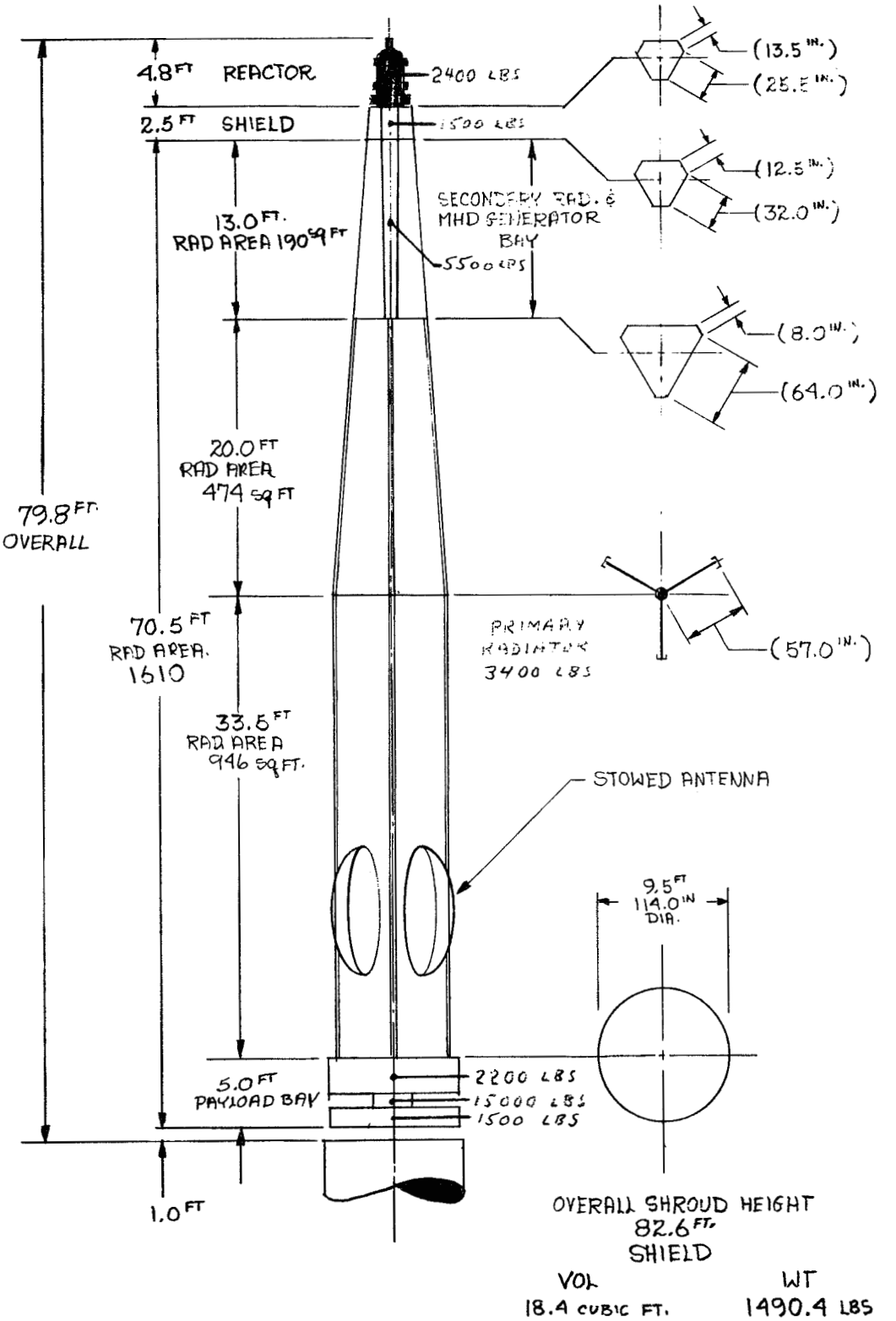

Figure 2-24. MHD Spacecraft Configuration No. 4, Triform Radiator

Configuration No. 5 (Figure 2-25) uses the triform radiator and projects the shield shadow to full diameter at the aft end of the MHD bay. This arrangement provides the shortest spacecraft and a roomy MHD equipment bay, but at the expense of increased shield weight.

In order to provide weights to be used in structural evaluation, the weights listed in Table 2-12 were assumed; these weights are based on Subsection 2.5 calculations with the shield weights calculated on the bases of 80 pounds per cubic foot, assuming lithium hydride with three and one-half percent stainless steel density for structure and containment and approximately 10 pounds per cubic foot allowance for shield cooling equipment.

2.6.3.2 Structural Analysis

The purpose of this analysis is to define the structural requirements for the five candidate spacecraft configurations to enable them to survive the static and dynamic load environments. The results of this study will be factored into the selection of a basic configuration.

The candidate configurations consist of two conical configurations, one cylindrical-conical configuration and two triform configurations. In each case, the spacecraft is cantilevered from the booster interface and no structure ties exist between the shroud and the spacecraft.

Two load conditions were considered in the analysis, representing the combined static and dynamic loadings at Stage I burnout and at Stage II burnout. These are shown below:

Stage I Burnout - 3 g's lateral and 6 g's axial.
Stage II Burnout - 0.67 g's lateral and 4 g's axial.

These load conditions constitute the limiting design cases according to the booster manufacturer (Reference 7).

This analysis was limited to the primary radiator section of the spacecraft. Maximum use was made of the structural material configured for thermal requirements. The additional structure required to meet the combined static and dynamic load conditions was then identified and sized.

A summary of the additional structural weight requirements along with the maximum lateral tip deflections for each configuration is presented in Table 2-13. It should be noted that Configurations

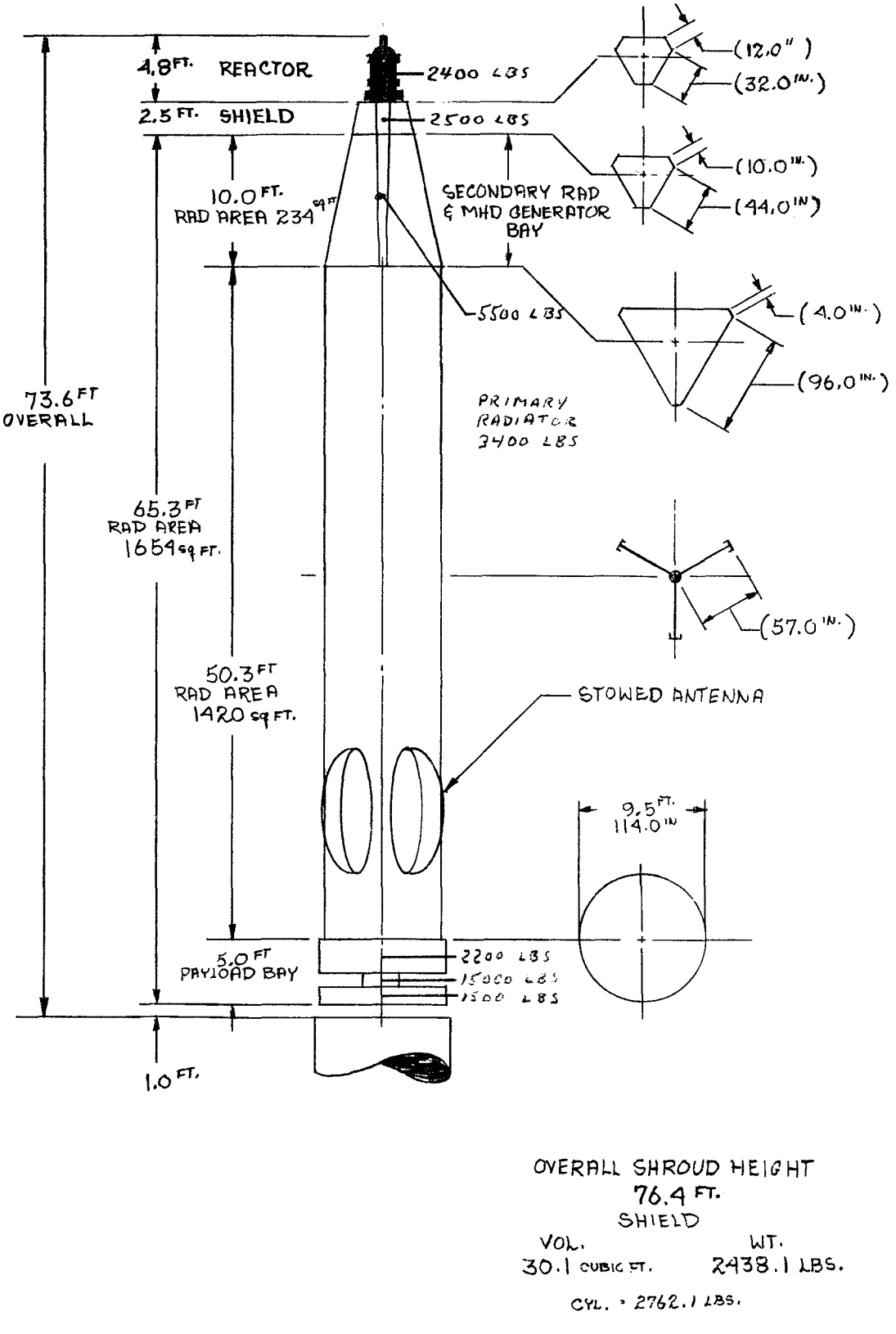

Figure 2-25. MHD Spacecraft Configuration No. 5, Triform Radiator

TABLE 2-12. MHD SPACECRAFT - WEIGHT ESTIMATES FOR CONFIGURATION TRADEOFF

ITEM		WEIGHT, POUNDS
Reactor		2400
Radiation Shield		1200 to 2500 *
Primary Radiator		3400 to 5800 **
MHD Bay		5500
Lithium Loop	400	
Cs loop	1570	
Auxiliary Cooling Loop	780	
MHD Nozzle Assembly	250	
MHD Generator	1500	
Capacitors	500	
Cables, Insulation, Etc.	500	
Payload		2200
Thruster System		1500
Propellant		15,000

* Varies with included angle; assumes 30 inch LiH with no gamma shield needed.

** 3400 pounds if triform geometry; 5800 pounds if cylindrical.

TABLE 2-13. SPACECRAFT WEIGHT AND TIP DEFLECTION SUMMARY

Configuration No.	ΔW_T	ΔW_L	ΔW_D	W_L	W_0	S_{TIP}
1	3920	3920	0	37,500	37,500	22.8
2	980	980	0	34,580	34,580	22.0
3	1030	1030	0	35,140	35,140	12.5
4	2450	250	2200	33,950	31,750	12.0
5	2370	224	2146	34,870	32,724	12.3

NOTES

All weights in pounds

ΔW_T - Total additional structural weight required

ΔW_L - Non-disposable additional structural weight required

ΔW_D - Disposable additional structural weight required

W_L - Total spacecraft weight at lift-off

W_0 - Total spacecraft weight in orbit

S_{TIP} - Maximum lateral tip deflection - inches

1, 3, 4 and 5 each have the 5500 pound MHD generator and secondary radiator bay located near the tip of the spacecraft in contrast to Configuration No. 2 which has the MHD generator and secondary radiator bay located near the booster interface. Therefore, the loading in the secondary radiator is considerably lower for Configuration No. 2 resulting in lower structural weight. Configuration No. 3 has a comparably low structural weight because of its shorter overall length, larger bending moment of inertia, and the same number of load paths in each bay (18 vapor ducts in each bay).

The primary radiators of Configurations 1 and 2 consist of six longitudinal elements and having the shape of truncated cones with each conical element made up of a number of flat radiator panels as shown in Figure 2-26. Configurations 1 and 2 have two elements of 24 panels, two of 12 panels and two of 6 panels. Configuration No. 3 has two cylindrical elements and two conical elements containing 18 panels each.

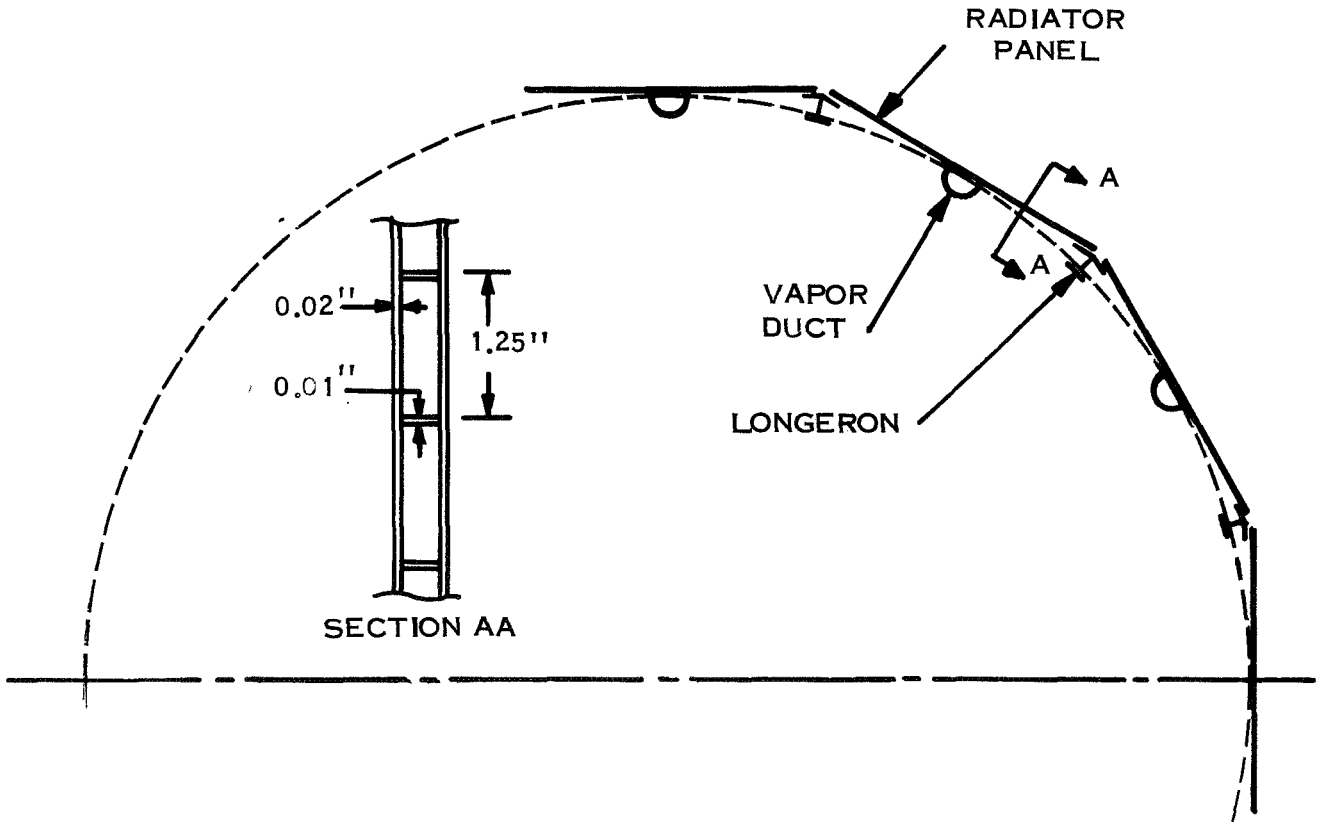

Figure 2-26. Cylindrical/Conical Radiator, Typical Cross-Section

A stability analysis of the 0.02-inch thick radiator panel skins employed in Configurations 1, 2 and 3 has shown that buckling will occur at about 8,000 psi, far below the 46,500 psi working stress of the 301-1/2 hard stainless steel structural material. Therefore, the panel skins were neglected as load carrying elements except in shear. The longitudinal loads are carried by the vapor ducts and the longerons located at the junctions of adjacent radiator panels. Four horizontal frames per conical or cylindrical element prevent buckling of the vapor duct and longerons. Because of the varying number of radiator panels in the conical elements of Configurations 1 and 2, load path discontinuities for the ducts and longerons exist at the junction of the conical elements. Therefore, shear panels have been provided at these junctions to redistribute the loads.

The conical-cylindrical configurations were assumed to have no disposable structure since the between-panel longerons and between-bay shear panels are expected to be impractical to jettison. Therefore, the structure sized for the maximum launch load must be carried throughout the complete mission.

The primary radiators of the triform configurations consist of flat panel elements maintained in a Y configuration by semibulkheads located at the junction of each longitudinal element. The length of a typical element is ten feet to twelve feet. Configuration No. 4 contains three 33.5-foot rectangular sections at the lower end and three 20-foot tapered sections at the upper end. Configuration No. 5 contains three 50.3-foot rectangular sections. The triform configurations have been designed using disposable structure to support the maximum Stage I burnout loads, leaving only that structure required to support the Stage II burnout loads to remain with the spacecraft throughout the mission.

To support the maximum Stage I burnout loads, 6.0 g's axial and 3.0 g's lateral, three disposable heavy channel sections are placed at the edge of the radiator and are joined to the launch vehicle at the base by a Marman clamp arrangement. Shear pins on 12-inch centers transmit the loads from the radiator structure to the support channels. Stabilizing bracing of 1-1/4 inch diameter tubes provide lateral and torsional stability. A typical section of this disposable structure is shown in Figures 2-27 and 2-28.

The remaining structure, required to support the Stage II burnout loads, 4.0 g's axial and 0.67 g's lateral, consists of light channels permanently attached to the edges of the radiator.

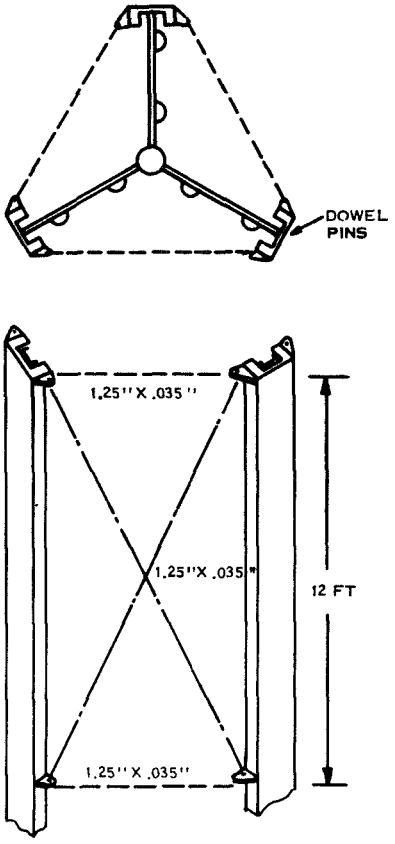

Figure 2-27. Triform Configuration, Typical Section with Stabilizing Bracing

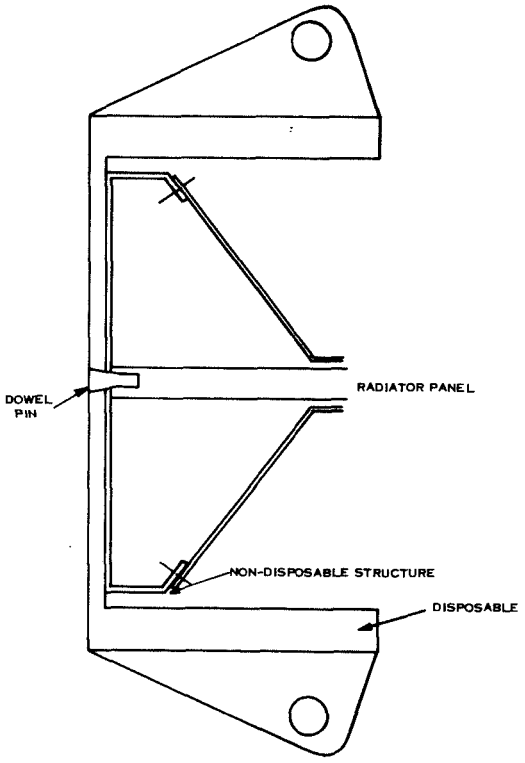

Figure 2-28. Triform Support Structure

In this appraisal, no methods of taking structural loads through a suitable reinforced flight fairing were considered. The flight fairing, at full diameter, offers the optimum bending moment of inertia per pound of material. However, reaching the load path would require that the payload and fairing diameters coincide or that load spreader members are included at suitably frequent intervals. It is not expected that a significantly lighter structural weight can be obtained by doubling up on the fairing; by using the separate structure, the analysis is simplified. An additional benefit of separate structure is that the payload is then acoustically isolated from the fairing; this is expected to be of significant advantage in the final design of small, poorly supported loads such as hoses and electrical leads.

Conclusions from this Structural Analysis include:

a. The fundamental frequency of the selected configuration should be calculated and compared with the booster requirements. It is anticipated that the resulting frequency will be on the order of one Hz which is below the current booster requirement of ~three Hz. The lower frequency can probably be accommodated by design changes in the booster autopilot

b. The effects of using aluminum in place of stainless steel for the disposable support structure of the triform designs should be analyzed. Stainless steel was chosen to eliminate differential thermal expansion. Since the MHD radiator is launched at low temperature, it may be possible to achieve attractive weight savings by using aluminum

c. The effects of locating the MHD generator and secondary radiator bay near the booster interface should be investigated.

2.6.4 CONFIGURATION CHOICE

The structural analysis preceding indicates that the triform radiator offers lower net weight than the conical radiator, so it will be used in the baseline design. The apparent success of the triform configuration here and its failure for the thermionic reactor spacecraft can be ascribed to the fact that the MHD radiator derives significant strength from the cesium vapor ducts. The conduction fin radiator in the thermionic reactor spacecraft uses many small tubes.

The configuration with the MHD bay located at the bottom of the radiator (No. 2) seems to offer significant structural weight savings, suggesting synthesis of a new configuration using a triform radiator with the MHD bay at the aft end. The attraction of this idea dims when one considers some of the problems and weights that were omitted from Configuration No. 2 in order to simplify its analysis. An estimate was made of the increase in lithium inventory, piping, and pumping that would accompany relocation of the MHD bay. If the reactor line size calculated for the baseline design were retained the pipe and coolant alone would increase in weight by approximately 1,000 pounds and the reactor line pressure drop would increase by approximately 30 psi. In addition, the lithium accumulator, the startup pump, etc. would have to increase in size. One can conclude, then, that relocation of the MHD bay to the aft end is possible but not attractive.

Configuration No. 4 will therefore be used as the basis for the baseline design arrangement.

2.7 POWERPLANT DESIGN

2.7.1 REACTOR AND SHIELD CHARACTERIZATION

The MHD power system requires a nuclear reactor heat source which can operate with coolant outlet temperatures ranging from 1600 to 2200°F. If possible, the reactor should be lithium-cooled in order that there is at least an option to use the reactor coolant directly in the MHD cycle. Since no reactors of this type are under active development at present, it is important to base MHD reactor parameter estimates on reactor development work which has been done. The following reactor design characteristics were generated on the basis of the PWAR-20 SNAP-50 design of 2.2 MW output (Reference 8). These characteristics are considered representative for an MHD reactor with minimum development time and risk. Extrapolations to other power levels and temperatures are based on data in Reference 9. Size extrapolation assumes that core size grows only in diameter and not in length, with core sectional area proportional to power. This assumption will give a conservative shield size estimate. The reactor design characteristics are listed in Table 2-14. Figures 2-29 and 2-30 show the size and weight variation with output power and Figure 2-31 shows an elevation view of the baseline design (3.75 MW) reactor and shield.

TABLE 2-14 MHD REACTOR DESIGN CHARACTERISTICS

Reactor Type (spectrum)	Fast
Design Life (full power hours)	20,000
Fuel	95% dense UC/UN
Coolant	Lithium
Coolant Outlet Temperature	Nominal 2000°F Range 1700 to 2300°F
Inlet to Outlet Coolant Temperature Difference	Nominal 100°F Range 75 to 125°F
Reactor Coolant Pressure Drop	Nominal 10 psi
Reactor Coolant Inlet Pressure	Nominal 53 psia*
Estimated Shield Thicknesses For 10^{12} nvt (> 1 Mev) and 10^{7} rad γ at 50-foot separation	30 inches LiH no γ shield

* Higher as necessary to suit MHD cycle conditions.

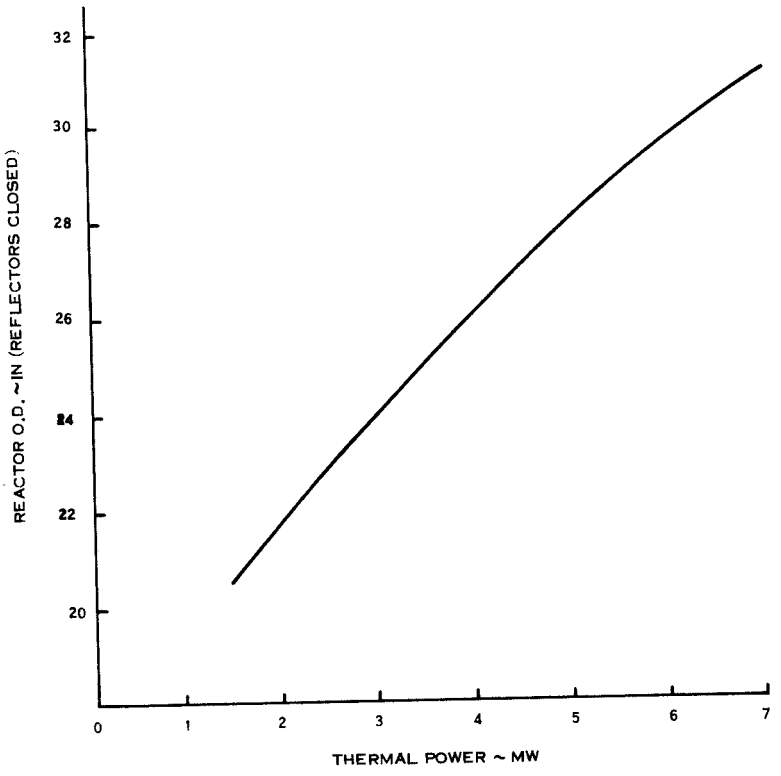

Figure 2-29 MHD Reactor Diameter

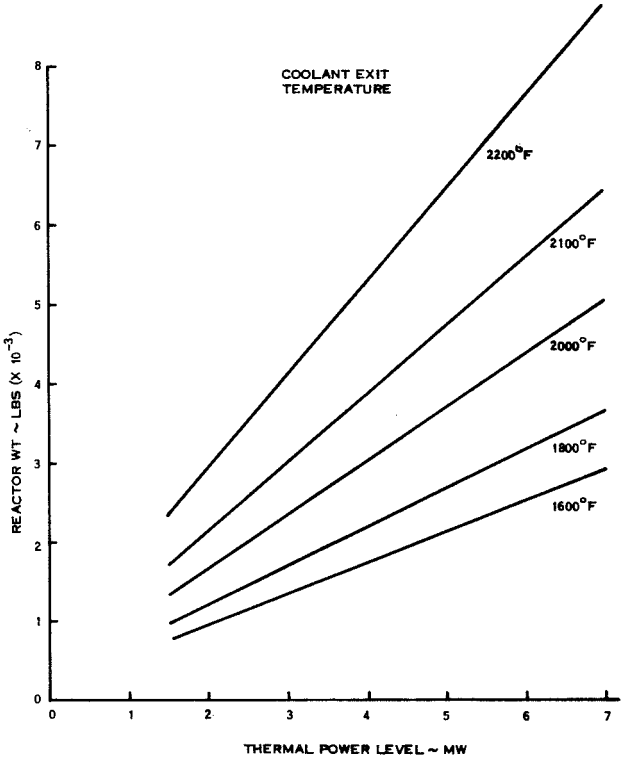

Figure 2-30 MHD Reactor Weight

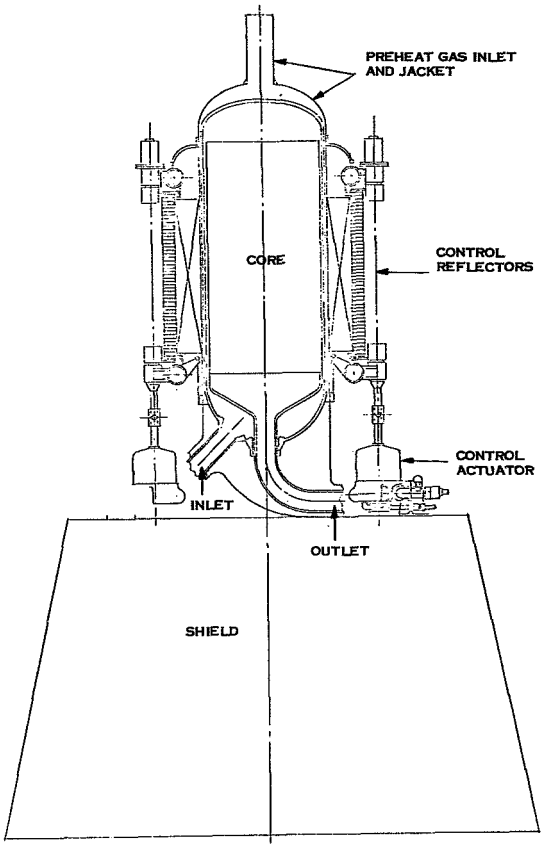

Figure 2-31. MHD Reactor and Shield

The reactor shown in Figure 2-31 uses six reflector shutters for control. The control drive shown in Figure 2-31 and in detail in Figure 2-32 is based on a nutating gear drive which may be used with a liquid-cooled drum control system and derives from a hydrogen flow control valve actuator which was designed by Bendix Corporation Aerospace Division for NASA in the NERVA program (Reference 10). This control drive actuator can be liquid cooled through the connections provided. This actuator can be used for a compact configuration. If desired, a more conventional drive could be installed below the shield with extension shafts running through the shield to the control reflectors. The actuator design could then be simpler but weight would probably be greater and the drives would occupy space below the shield which is desired for MHD equipment.

2.7.2 MHD GENERATOR DESIGN

In selecting the baseline design parameters (Subsection 2.5) the auxiliary radiator was assumed to operate at 400°F removing the heat from the MHD generator. For calculation of electrical winding losses in the MHD generator it was assumed that the temperature difference between the winding coils and the auxiliary coolant is negligible; at the same time, the need to test this assumption by some analysis

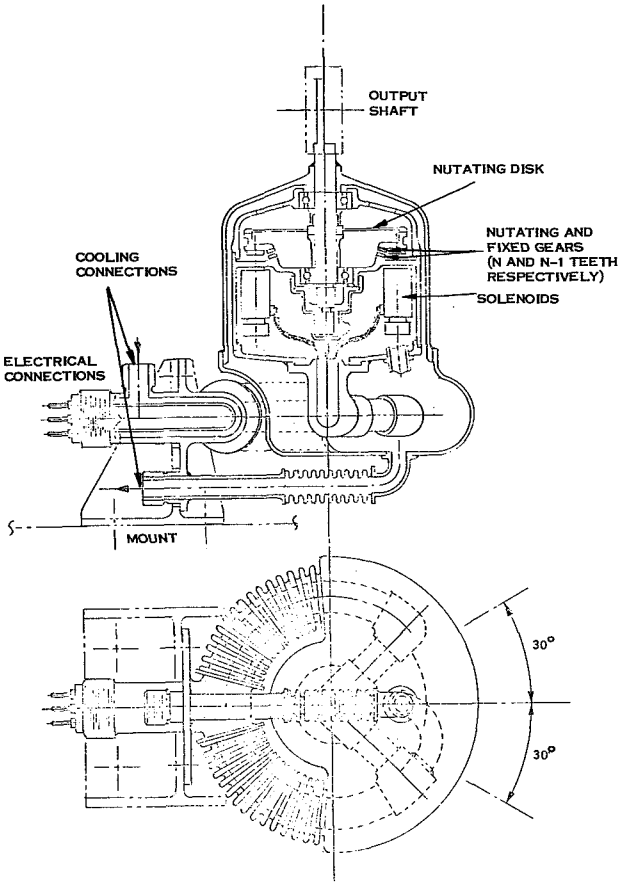

Figure 2-32. MHD Reactor Control Actuator

was reviewed for possible modifications by which the generator could be cooled without degrading its electrical performance.

The heat to be removed from the generator stators consists of 25 to 50 kW conducted into the iron from the hot lithium channel and 5 to 15 kW generated in the copper coils by I^2R loss. The copper temperature must be controlled to 400°F or so to minimize these I^2R losses and the iron must be kept well below its Curie temperature, about 1000°F (Curie temperature of iron $\approx$1400°F), to keep its magnetic permeability high.

Several techniques for cooling the stator are being investigated. Coolant passages may be installed in the stator above the slot transverse to the channel or coolant passages may be installed along and parallel to the channel wall. The geometries are indicated in Figures 2-33 and 2-34. Coil dissipation may be transferred to the stator and removed by the stator coolant or conducted through the coils transverse to the channel and removed from the coil sections outside the stator block. A scheme for cooling the coils as they cross over the stator is shown in Figure 2-35. A third stator cooling possibility is to transfer energy from stator to coils and then cool the coils as in Figure 2-35.

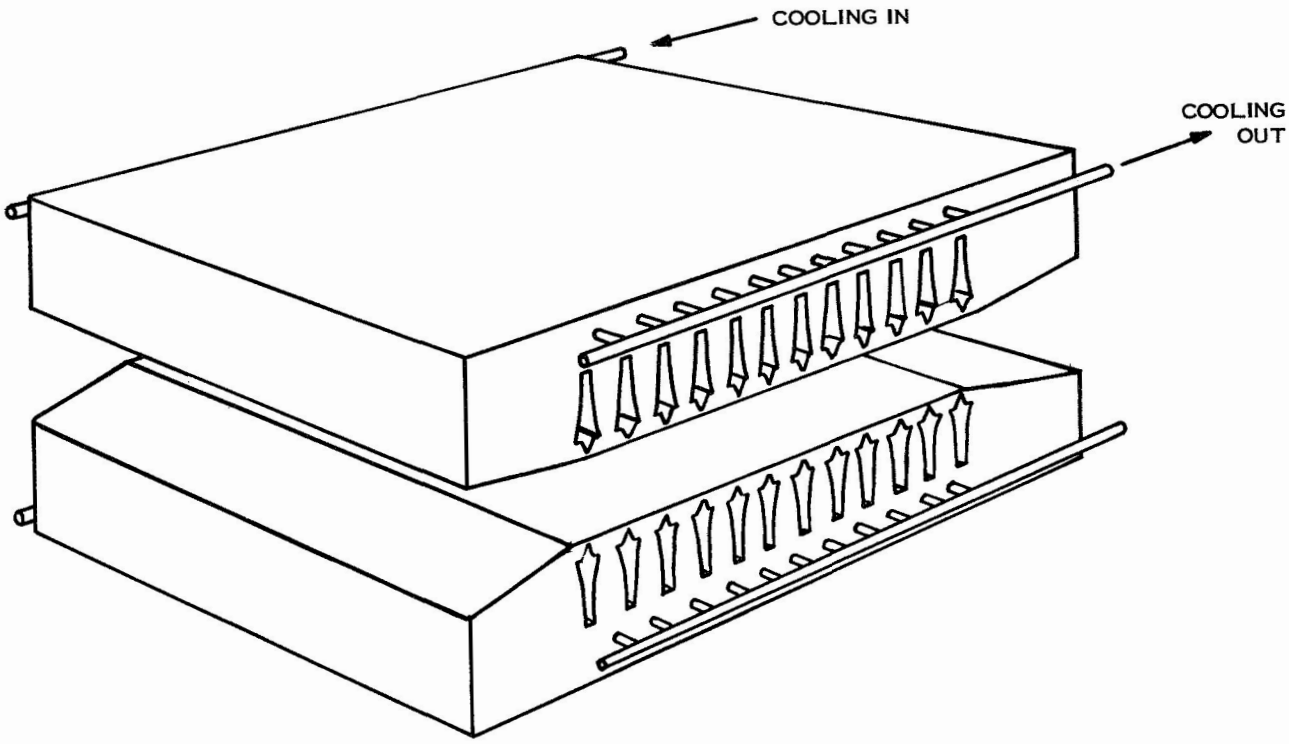

Figure 2-33. Cooling Pipes in MHD Stator Block

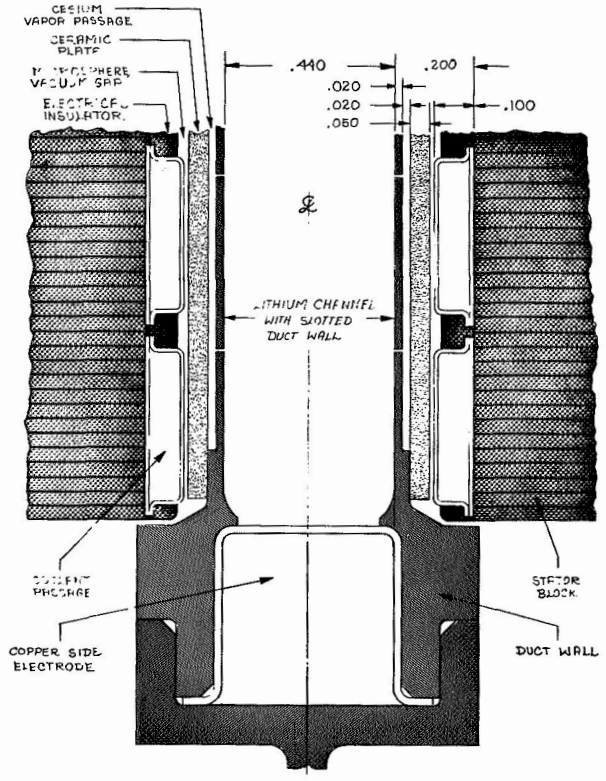

Figure 2-34. MHD Stator Cooling Passages at Lithium Duct Face

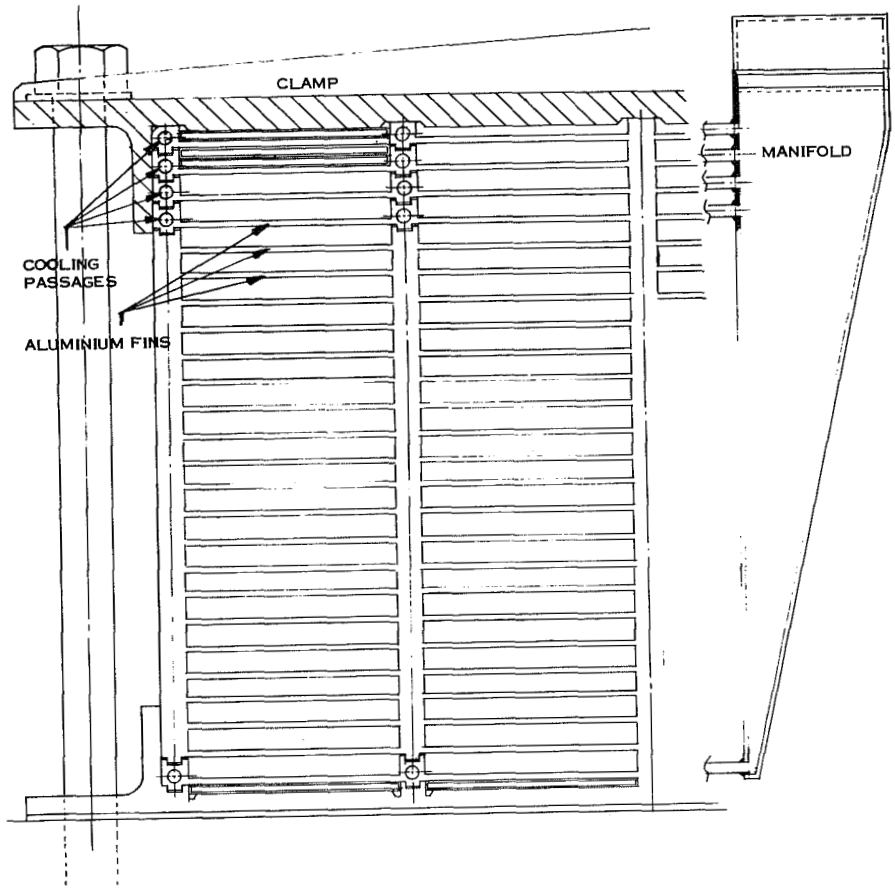

Figure 2-35. Actively-Cooled External Winding Loom

Considering now the cooling technique shown in Figure 2-33, the stator temperature gradient perpendicular to the channel from the channel wall to a coolant passage would be about 800°F including transfer of coil dissipation into stator. Cooling the coil independently reduces the gradient to about 700°F. This technique results in an acceptable stator temperature near the channel only if the coolant temperature is rather low.

Cooling the stator using NaK in 0.010-inch channels as shown in Figure 2-34 is feasible considering pumping power, pressure drop, etc. With the NaK temperature increase 10 to 20°F, pumping power is 48 to 8 watts with pressure drop 0.7 to 0.2 psi. The stator gradient due to transferring coil dissipation into the stator would be about 100°F.

Due to the difference in desired temperature levels of the stator and the coils and the gradient across the coil insulation, it does not seem practical to cool the coil through the stator. An independent cooling scheme such as shown in Figure 2-35 has been considered for removing the coil dissipation only. Gradients of about 5°F would exist in the aluminum structure while the insulation gradient would be about 40°F (6 mils of silicone rubber). Gradients along the length of the coils, transverse to the channel, would be approximately 100°F.

The final possibility - cooling stator and coils with the aluminum structure of Figure 2-35 depends again on the gradients across insulation. In this case, the gradient from stator to coil is in the right direction - stator hotter - but the magnitude is also about four times larger due to the energy quantities involved. Gradients in the stator would be about 300°F perpendicular to the channel and 230°F transverse to the channel. Coil gradients along the length would be about 300°F and there would be gradients of as much as 150 to 170°F across the coil insulation (6 mils of silicone rubber).

A magnitude has not been given for the gradient across the stator-coil insulation. The heat transfer area there is about 1/6th of the area in contact with the aluminum structure thus gradients across 6 mils of silicon rubber would be six times those given above. If energy is to be transferred between stator and coil, the coil insulation will have to be a good thermal conductor to lower the temperature differences given above.

These cooling techniques are being evaluated in order to identify realistic temperatures for the auxiliary radiator and the associated winding temperatures. There will be no attempt to develop one or more of these techniques to detailed design in this phase of the study.

2.7.3 RADIATOR DESIGN

Study guidelines for the MHD spacecraft specify the use of a triform vapor chamber fin radiator with condensing cesium as the primary fluid. As previously mentioned (Subsection 2.6, Configuration Trade-offs) the cone/cylinder configuration is being retained as a possible alternative. Various heat rejection system studies conducted at General Electric have indicated that consideration of radiator structural requirements often decreases the attractiveness of flat panel radiators. Although these conclusions have been based on conduction fin radiator analyses, they might be expected to be valid for vapor chamber fin radiators as well.

Work currently in progress at General Electric under the Vapor Chamber Radiator Study, NAS 3-10615, includes evaluation of four design concepts which are applicable to the MHD radiator. These concepts include:

a. Cylindrical or elliptical tube/fin

b. Rectangular channel

c. Hexagonal honeycomb

d. Rectangular channel/fin

These gemoetries were compared on the basis of utilization in a cone cylinder, load bearing radiator for the advanced Rankine cycle. Radiator inlet and outlet temperatures were 1200 and 980°F, respectively. Vapor chamber construction was assumed to be stainless steel; wicking material was assumed to be 150 by 150 mesh screen. Sodium, potassium and cesium were the candidate fluids.

Radiator weights for each combination of geometries and fluids were calculated over a range of parameters as illustrated in Figures 2-36, through 2-39. A comparison of the vapor chamber fin specific weight versus vapor chamber condenser length is shown in Figure 2-40. The "A" and "C" designations refer to a 0.020 inch and 0.010 inch fin thickness, respectively. During this phase of the study potassium and cesium were excluded from further study due to sodium's superior performance (see Figure 2-41).

In order to obtain a more complete evaluation of the overall radiator weight the vapor chamber fin results were combined with an analysis of the primary ducts. Two duct geometries were examined as shown in Figures 2-42 and 2-43. Figure 2-42 shows an unpenetrated duct whereas the duct in Figure 2-43 is penetrated by the vapor chamber fin. A summary of the thermally optimum total radiator weights including primary ducts, vapor chambers, wicks, and fluid inventory is presented in Table 2-15.

The next step in the radiator geometry evaluation was consideration of additional structural members required to support a 15,000 pound powerplant during a Saturn V launch where the radiator is the aerodynamic fairing. Table 2-16 summarizes the complete radiator system weight including structural weight. The lightest weight is obtained using Configuration No. 2 with an unpenetrated duct.

Fabricability of these concepts was also investigated. The easiest geometries to fabricate are cases 1 and 4, however, 2 was also felt to be possible. The fabrication of geometry 3 was judged to be extremely difficult since each honeycomb section must be sealed from adjacent cells.

A final comparison of the concepts on the basis of thermal, structural and fabrication considerations is presented in Figure 2-44. A rating has been assigned to each geometry under each criteria. In view of these results, the concepts, in order of preference, are: rectangular channel, cylindrical and rectangular channel/fin, and hexagonal honeycomb.

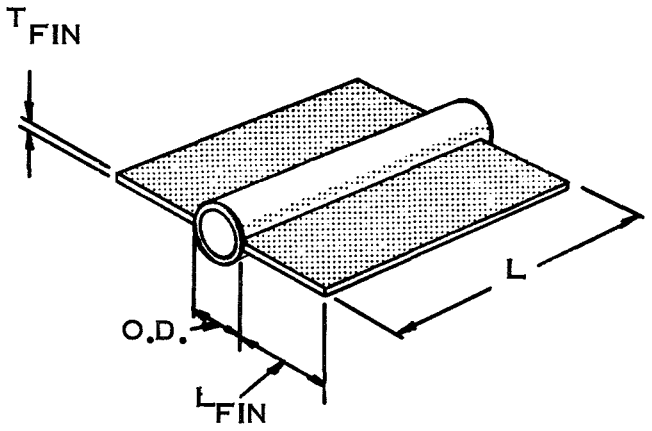

PARAMETERS EVALUATED

LENGTH (L) = 0.50', 1.0', 1.5', 2.0'

O. DIAMETER (O.D.) = 0.500", 0.750", 1.000"

FIN THICKNESS (T_{FIN}) = 0.010", 0.020", 0.040"

FIN LENGTH (L_{FIN}) = 0.000", 0.125", 0.250", 0.500"

TUBE THICKNESS = 0.015

Figure 2-36. Concept 1, Cylindrical or Elliptical Tube Fin

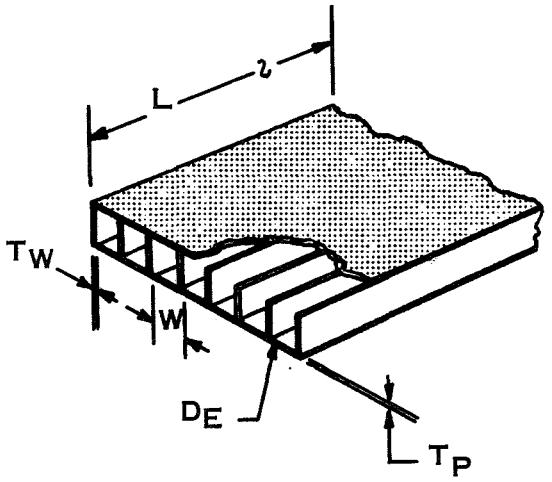

PARAMETERS EVALUATED

LENGTH (L) = 0.500', 1.000', 1.500', 2.000'

EQUIV. DIA. (D_E) = 0.250", 0.500", 0750"

CHANNEL WIDTH (W) = 0.250", 0.375", 0.500", 0.750"
1.000", 1.500"

PLATE THICKNESS (T_P) = 0.015" 0.023"

INNER WALL THICKNESS (T_W) = 0.010"

Figure 2-37. Concept 2, Rectangular Channel

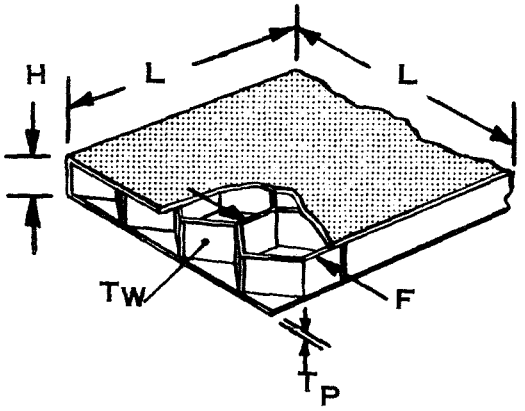

PARAMETERS EVALUATED

LENGTH (L) = 0.50', 1.00', 1.50', 2.00'

DISTANCE ACROSS FLATS (F) = 0.250", 0.500", 1.000", 2.000", 3.000"

HEXAGON HEIGHT (H) = 0.250", 0.500", 0.750"

PLATE THICKNESS (T_P) = 0.005", 0.010", 0.020"

INNER WALL THICKNESS (T_W) = 0.005", 0.010", 0.020"

Figure 2-38. Concept 3, Hexagonal Honeycomb

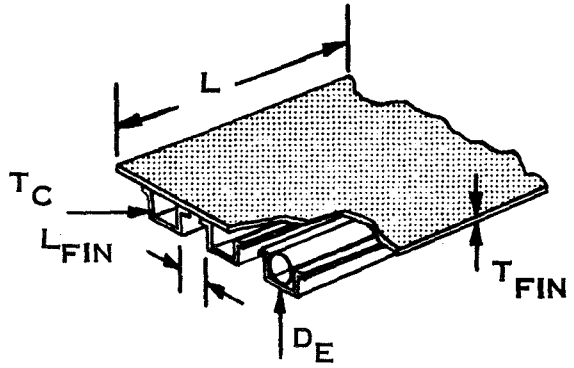

PARAMETERS EVALUATED

LENGTH (L) = 0.50', 1.00', 1.50', 2.00'

EQUIV. DIA. (D_E) = 0.500", 0.750", 1,000"

FIN THICKNESS (T_{FIN}) = 0.010", 0.020", 0.040"

FIN LENGTH (L_{FIN}) = 0.000", 0.125", 0.250", 0.500"

CHANNEL THICKNESS (T_C) = 0.015"

Figure 2-39. Concept 4, Rectangular Channel Fin

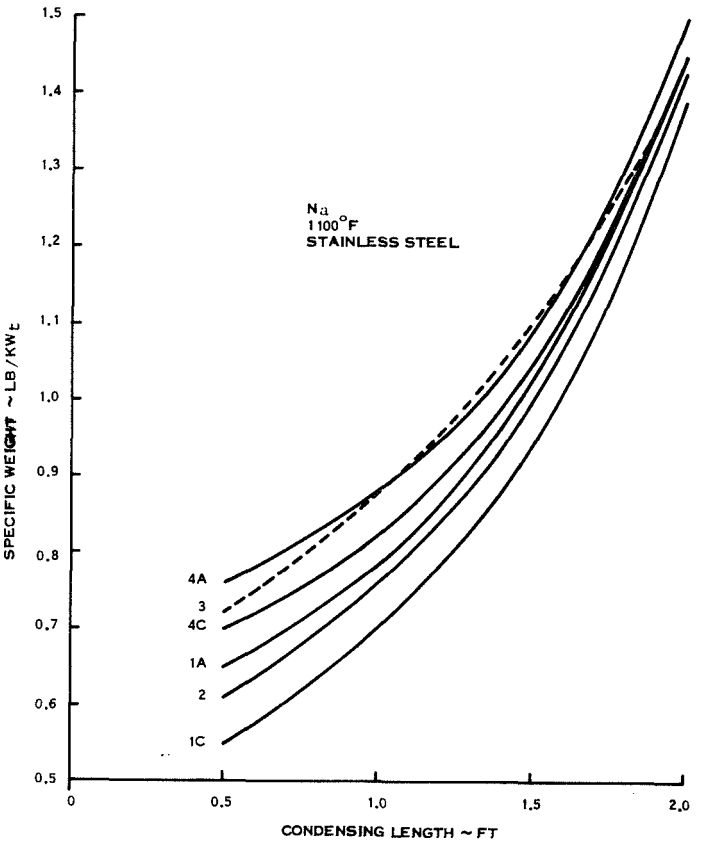

Figure 2-40. Comparison of Condensing Configuration

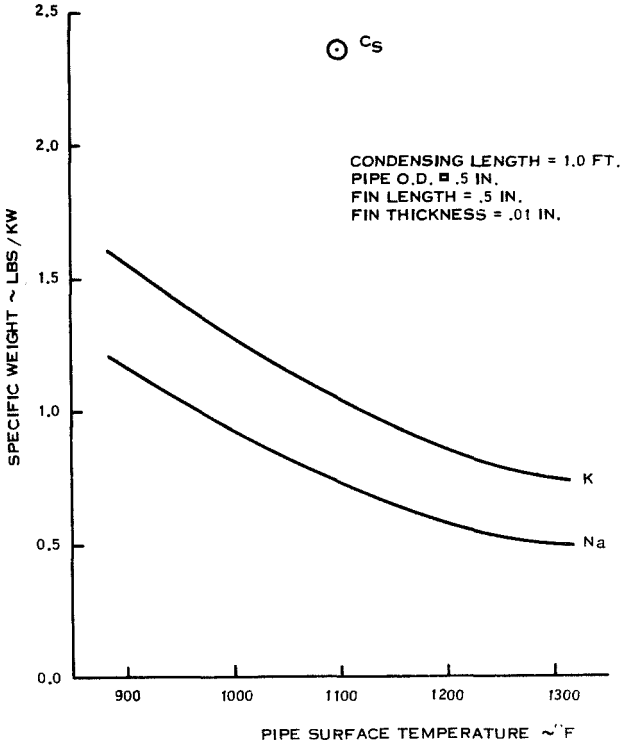

Figure 2-41. Fluid Comparison Finned Cylinder Geometry

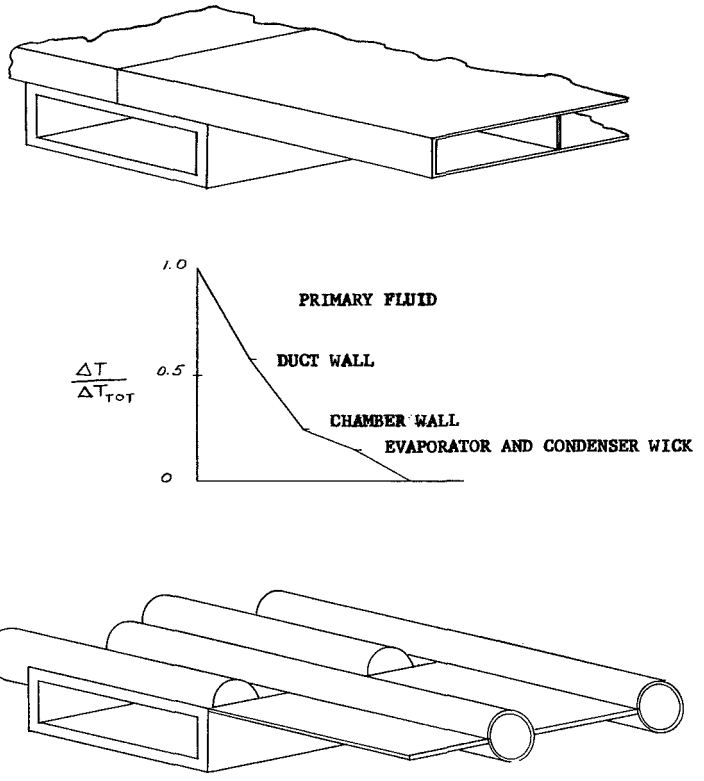

Figure 2-42. Duct - Chamber Concepts - Unpenetrated Duct

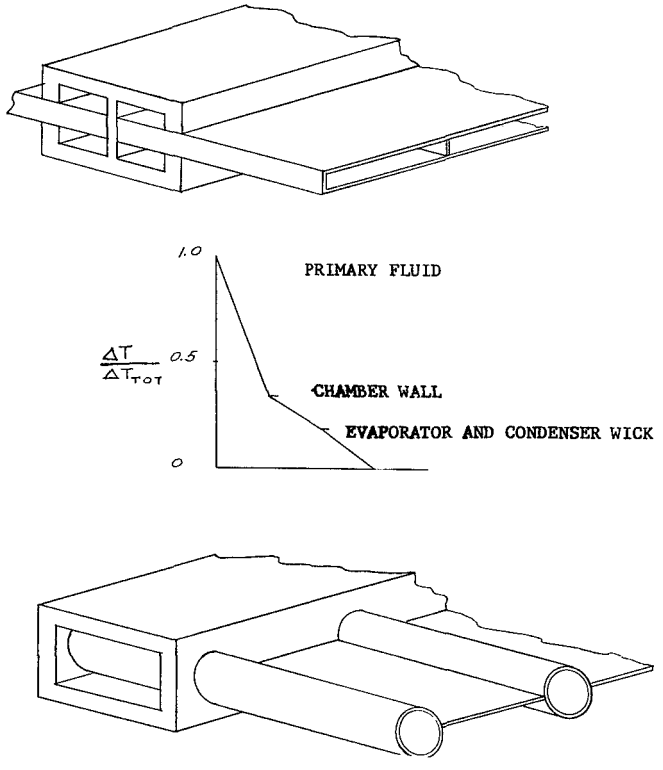

Figure 2-43. Duct - Chamber Concepts - Penetrated Duct

TABLE 2-15. SUMMARY OF RADIATOR WEIGHTS
(NO STRUCTURAL CONSIDERATIONS)

CONFIGURATION (OPEN DUCTS)	WEIGHT (LBS.)	AREA (FT^2)	NUMBER OF CHAMBERS
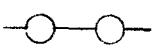 1, 10 mil fins	1510	855	11,500
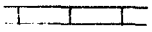 2	1670	630	9,200
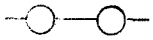 1, 20 mil fins	1700	800	8,500
 4, 10 mil fins	1710	885	8,900
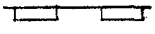 4, 20 mil fins	1850	860	6,550
 3	2500	950	281,000
(CLOSED DUCTS)			
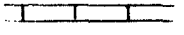 2	1520	750	11,100
 1, 10 mil fins	1800	1000	12,800
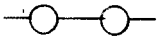 1, 20 mil fins	1950	950	9,050
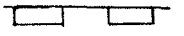 4, 10 mil fins	1980	990	8,950
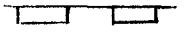 4, 20 mil fins	2075	950	7,700
 3	2850	1370	405,000

TABLE 2-16. SUMMARY OF RADIATOR WEIGHTS

CONFIGURATION (OPEN DUCTS)	AREA FT^2	NO. OF CHMB'S	WEIGHT RAD.	RINGS REQ'D	RING WT-LBS	REQ. SHEET THK.	SHEET WT.	TOTAL WT.
1, 10 mil fins	855	11,500	1510	6	303	.019	363	2176
2 15 mil plates	630	9,200	1670	4	195	.018	166	2031
1, 20 mil fins	800	8,500	1700	6	283	----	---	1983
4, 10 mil fins	885	8,900	1710	6	314	.019	375	2399
4, 20 mil fins	860	6,550	1850	6	305	----	---	2155
3 .5"cell(.0075")	950	281,000	2500	6	324	.0095	155	2979
(CLOSED DUCTS)								
2 15 mil plates	750	11,100	1520	4	232	.018	197	1949
1, 10 mil fins	1000	12,800	1800	10	560	.018	382	2742
1, 20 mil fins	950	9,050	1950	10	532	----	---	2482
4, 10 mil fins	990	8,950	1980	8	436	.023	470	2886
4, 20 mil fins	950	7,700	2075	8	418	----	---	2493
3 .5" cell(.0075")	1370	405,000	2850	8	464	.011	362	3676

CONFIGURATION	THERMAL	STRUCTURAL	FABRICATION	TOTAL RATING (LOW IS GOOD)
1 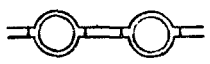	1 HIGH RATIO OF FLOW AREA TO HEAT PIPE CIRCUMFERENCE MINIMUM WEIGHT	4 LOW LOAD AREA AND SMALLER PRIMARY DUCT RADIUS OF GYRATIONS CAUSE LOCAL AND PANEL INSTABILITIES	1 CONSIDERED ON A PAR WITH (4) IF EXTRUSION IS USED	6
2 	1 HIGH EFFECTIVE RADIATOR TEMP. GOOD EVAPORATOR INTERFACE MINIMUM RAD. AREA	1 THERMALLY DEFINED GEOMETRY MORE CLOSELY MEETS LOCAL AND PANEL STABILITY REQUIREMENTS	2 SOMEWHAT MORE DIFFICULT THAN (1) OR (4) BUT USE OF FLANGES PERMITS GOOD BRAZE	4
3 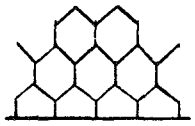	3 GOOD EVAPORATOR INTERFACE POOR HEAT TRANSFER	2 INCREASED RADIATOR AREA REQUIREMENTS NECESSITATE LARGER BAYS ∴ THUS INCREASE PANEL INSTABILITY	3 CONSIDERED VERY DIFFICULT IN THE CHARGING & SEALING OF CHAMBERS	8
4 	2 GOOD METEOROID RESISTANCE AREA COMPARABLE TO (1), HIGHER WEIGHT	3 LOW LOAD AREA AND SMALL PRIMARY DUCT RADIUS OF GYRATION CAUSE LOCAL AND PANEL INSTABILITIES	1 CONSIDERED TO BE SIMPLE TO FABRICATE BY WELDING OR BRAZING	6

Figure 2-44. Evaluation Summary and Recommendations

2.7.4 ELECTRICAL SYSTEM

Reasonable estimates have been made of size, weight and equipment efficiency of some of the MHD spacecraft electrical equipment; however, further study and tradeoff analyses will be performed prior to determining an overall system minimum size and weight, and maximum efficiency.

2.7.4.1 Requirements

The primary functions of the electrical system are to convert the electrical power developed by the magnetohydrodynamic (MHD) generator to forms suitable for use by the various electrical loads and to distribute the electrical power with proper protection and control.

A tabulation of the spacecraft loads and their electrical requirements is given in Table 2-17. Thruster power requirements are shown in Table 2-18. The main portion of the electrical power is required by the ion thruster screen grids which require about 7.2 kW each at 3100 volts dc. A total of 37 thrusters are on the spacecraft of which 31 are active and 6 are spares.

Because details of the electrical characteristics of the magnetohydrodynamic (MHD) generator are not complete, characteristics corresponding to these several operating conditions are not available. For preliminary design purposes, the output was assumed as follows:

MHD Generator

Power	300 kWe
Voltage	600 Vac, 3Ø, Y connected
Frequency	275 Hz
Excitation	1300 kVAR, 261.6 mfd

The electrical system must be designed to provide power to the loads under the following conditions during the flight:

a. Full power operation (300 kW) at beginning of mission (BOM)

b. Full power operation (300 kW) at end of mission (EOM)

c. Ten percent power operation (30 kW) during coast. During this period, the thrusters are inoperative and the only loads connected are hotel loads and payloads.

TABLE 2-17. SPACECRAFT ELECTRICAL LOAD REQUIREMENTS

ITEM	FUNCTION	POWER REQUIRED - kW
Cesium Pump	Returns cesium condensate to MHD cycle	25
Shield Pump	Cools shield	0.12
Auxiliary Pump	Cools MHD generator, pumps, etc.	0.1
Reactor Controls	Controls reactivity of reactor	2.0
Thrusters	Propulsion	240.0
Payload	Science and Communications	1.0
Guidance and Control	Thrust vector control - ion engines	0.5
System Controls	Protection, switching and control of electrical system	0.5

TABLE 2-18. THRUSTER POWER REQUIREMENTS

TABLE 2-3. THRUSTER POWER SUPPLY REQUIREMENTS

Supply Number	Supply Name	Type	Output (1)	NOMINAL RATING					MAX. RATING			Control Range, A
				Volts	Amps	Watts	Reg. %	Peak Ripple	Volts	Amps	Amps Limit (2)	
1	Screen	DC	V	3100	2.32	7200	1.0(V)	5	3200	2.32	2.60	2.0 - 2.4
2	Accelerator	DC	F	2000	.02	40	1.0(V)	5 @ 0.2 A	2100	0.20 (3)	0.21	---
3	Discharge	DC	V	35	8.3	290	1.0(V)	2	150 @ 50 mA	9 @ 37V	10	7.5 - 9.0
4	Mag. - Man.	DC	F	15	.7	11	1.0(I)	5	20	1.0	1.0	---
5	Cath. Htr. (4)	AC	F	10	4.0	40	5.0	5	11	4.4	4.1	---
6	Cath. Keeper	DC	F	10	0.5	5	1.0(I)	5	150 @ 50 mA	1.0 @ 20 V	1.0	---
7	Main Vapor.	AC	V	0.6	1.0	1	Loop	5	8 (5)	2.0	2.2	0.5 - 1.5
8	Cath. Vapor	AC	V	0.3	0.5	1	Loop	5	8 (5)	1.0	1.1	0.2 - 0.8
9	Neut. Cath. Htr.	AC	F	10	2.0	20	5.0	5	11	2.2	2.2	---
10	Neut. Vapor.	AC	V	0.3	0.5	1	Loop	5	8 (5)	1.0	1.1	0.2 - 0.8
11	Neut. Keeper	DC	F	10	0.5	5	1.0(I)	5	150 @ 50 mA	1.0 @ 20 V	1.0	---

(1) V = Variable, F = Fixed

(2) Current limit or overload trip level.

(3) Current at this level for less than 5 min. at low repetition rate.

(4) Needed only during startup or until discharge reaches 3A.

(5) Startup only.

2.7.4.2 System Description

The electrical system preliminarily proposed for use with the MHD generator is shown in Figure 2-45. In this system approximately 80 percent of the 300 kW, 3 phase output is transformed and converted to 3100 volts dc, whereas the remaining power is distributed at the 600 volts ac, 3 phase, generated output level.

The high voltage bus provides power to all of the screen electrodes of the ion engine thrusters. The 3100 volt transmission level is established by the voltage requirements of the screens.

The 600 volts ac, 3 phase distribution bus provides power to the remaining spacecraft loads including the several power supplies required for each thruster, as well as hotel and payloads. The 600 volts ac level was selected as the generator output so that power distribution could be done at a sufficiently high voltage to minimize cable lose without requiring power conversion. Any higher voltage is considered inconvenient because of handling and component selection problems and should not be used except where necessary. Since typical 50-turn MHD generator coils produce voltages on the order of 700 volts, the choice of 600 volts as reference is considered reasonable.

Power to the hotel loads and to the thruster auxiliary power supplies and to the payloads is distributed by means of two busses; one group of loads are near the generator and one group at the thruster payload area. Figure 2-45 shows the two busses and associated loads.

The weight of the electrical system is shown on Table 2-19, with the breakdown on the high voltage converter on Table 2-20. Electrical system power losses are identified on Table 2-21.

2.7.4.3 High Voltage Power Distribution

2.7.4.3.1 Transformer Selection - In order to minimize transmission cable loss, the 600 volts ac is transformed as close to the MHD generator as practical. With ac voltage generated, voltage increase is performed using a single, liquid cooled, three phase transformer. The output is rectified and regulated by use of a Silicon Controlled Rectifier (SCR) set and then the three dc outputs are connected in parallel and filtered to create the high voltage distribution bus.

The selected transformer is approximated to be 12 by 12 by 24 inches high, of which the height has an allowance of ten inches for coolant connections. The weight is estimated to be 100 pounds. Power losses in the transformer are about 4 kW, and hollow conductor wire is used for heat removal.

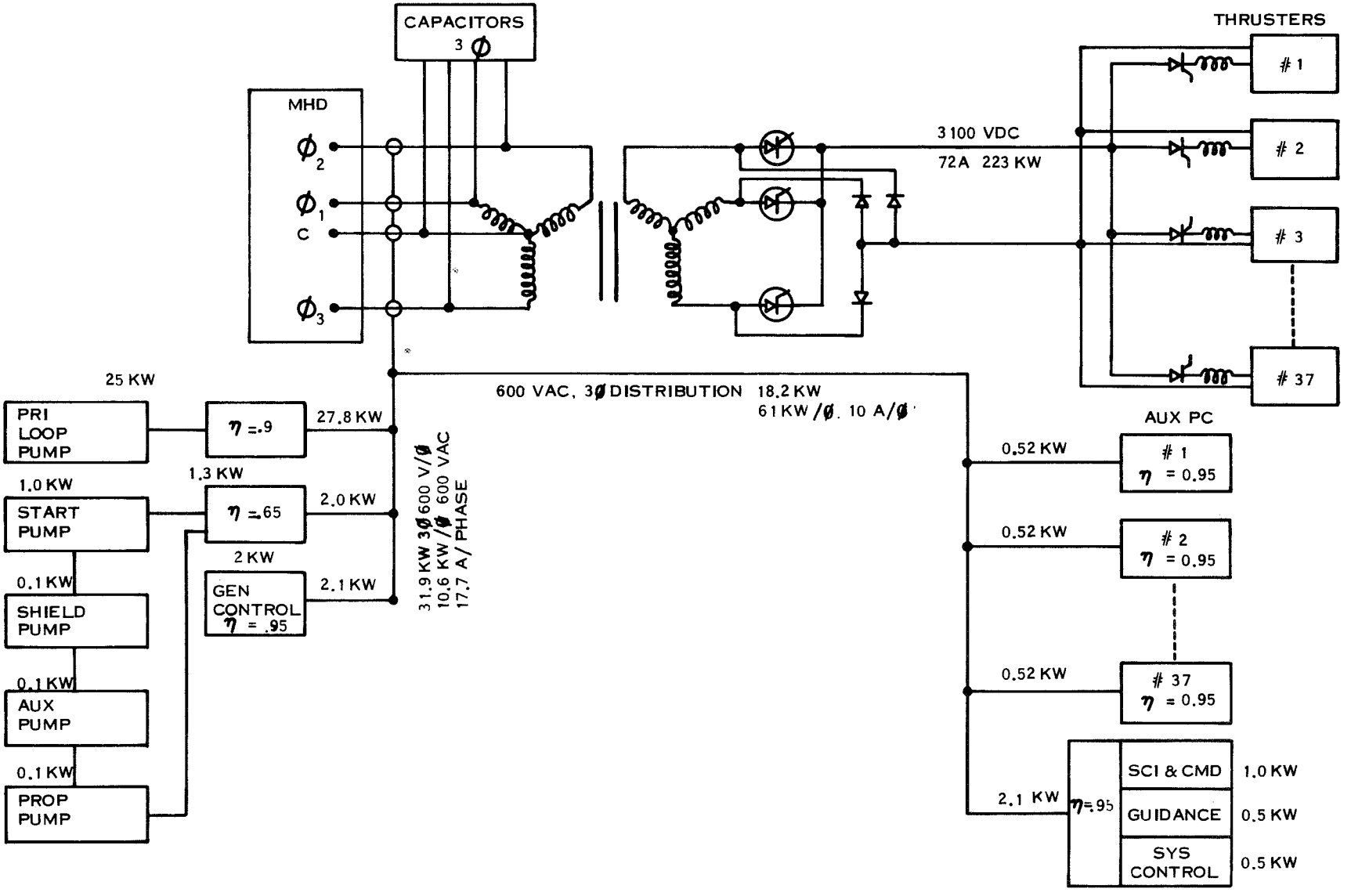

Figure 2-45. MHD Spacecraft Electrical Power System

TABLE 2-19. ELECTRIC SYSTEM WEIGHT SUMMARY

Capacitors	450
High Voltage Converters	163.5
Auxiliary Power Conversion	277
Thruster Auxiliary PC	272
Power Distribution Cables	*
Screen Supply Interrupters	460
	*

* Later

TABLE 2-20. HIGH VOLTAGE CONVERTER WEIGHT BREAKDOWN

HV Converters	
Transformer	100.0
Rectifiers	3.0
Control Circuits	0.5
Wire, Brackets, Heat Paths	60.0
	163.5

TABLE 2-21 ELECTRIC SYSTEM POWER LOSSES

HV Converters	
Transformer	4,000
Rectifiers	660
Control Circuits (voltage control)	8
Total HV PC	4,668
Screen Supply Interrupters	1,250
EM Pump Power Conditioning	3,500
Payload Power Conditioning	50
Generator, Spacecraft Control Power Conditioning	155
Total Power Conditioning Losses	9,623
Total Capacitor Losses	*
Total Transmission Cable Losses	*
Total Power Losses	*
Overall Efficiency for 300 kWe MHD Generator System	*

* Later

2.7.4.3.2 Rectifier Selection - Rectification and voltage regulation is performed by phase controlled Silicon Controlled Rectifiers (SCR's). In an ac circuit the SCR must be triggered into conduction at the desired instant of time during the half-cycle of the applied voltage wave during which the anode is positive. In the phase controlled circuit, initiation of conduction is delayed by an angle so that the SCR conducts for only a predetermined portion of the positive half-cycle. In this manner the average power delivered to the load can be varied, and when coupled with a filter, the output results in a voltage regulated dc bus.

When the line voltage reverses every half-cycle, the SCR will be automatically commutated off and consequently will not require special circuits. The unit selected for this application is the GE-SCR type C145PB, with a repetitive Peak Reverse Voltage (PRV) of 1200 volts and a 55 ampere rms limit. Due to the type of circuit, the PRV for the SCR would be 1.4 (load voltage), and consequently would require four SCR's in series for each phase.

The SCR can be used in series circuits, however some form of forced voltage sharing becomes mandatory. For the purposes of this study it will be assumed that there is proper voltage sharing.

Power loss in each SCR, assuming close to 180 degree conduction angle and 24 amperes (average) would be 55 watts each (average).

Each group of four SCR's are mounted on an aluminum heat-sink as shown below. Combined weight is approximately one pound per phase.

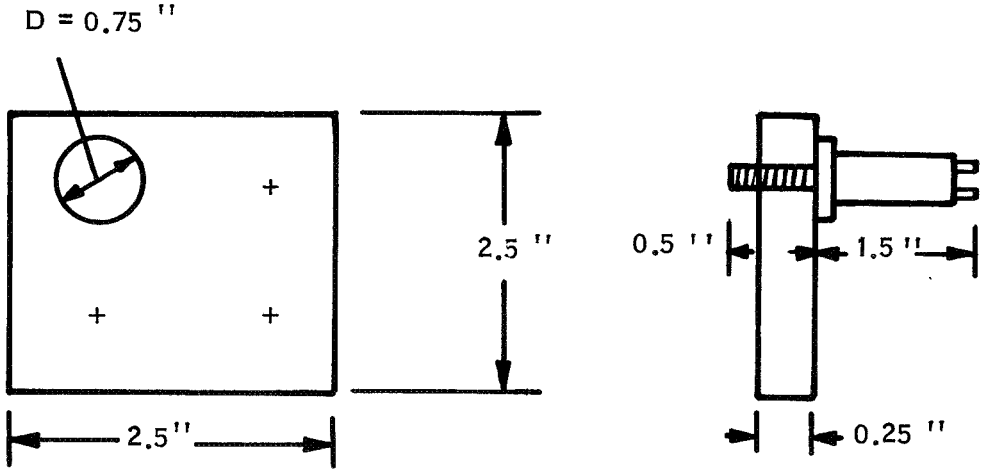

2.7.4.4 Low Voltage Power Distribution

An ac three-phase distribution was selected for the hotel and auxiliary power system in order to realize simplified power conditioning and reduced copper losses.

With ac being generated and distributed, the inverter stage of all the power conditioners can be eliminated thereby raising the efficiency of conversion. The remaining losses would be transformation and rectification.

Analysis shows that the same amount of power may be transmitted a fixed distance with a fixed line loss with only three-fourths of the amount of copper that would be required for single-phase, or one-third more copper is required for single-phase than would be necessary for three-phase.

2.7.4.5 Capacitor Selection

The voltage of the MHD generator depends upon the magnetizing component on the stator current, and unless the load calls for a component equal to this component, the generator will not operate. The function of the capacitors which are connected in parallel with the MHD generator is to adjust the power factor of the load on the generator to that at which it can deliver the required power. The capacitors must not only supply whatever lagging current is required by the load but must also supply a lagging current equal to the leading magnetizing current of the generator. For the purpose of the study the load will be assumed to require no compensation.

Computer analysis has shown that about 1300 KVAR must be supplied and that the capacitor must be 261.6 mfd. Assuming this to be a machine total, 433 KVAR and 87.2 mfd are required for each phase.

A limited industry search has shown that no units are available without development; however, the technology exists for designing a capacitors to meet the requirements.

General Electric Company, Large Capacitor Department has made an estimate of the size and weight of a bank of capacitors and reports that for the three phase machine, the capacitor would be 12 by 12 by 36 inches and weigh 450 pounds.

2.7.4.6 Thruster Screen Interrupters

The electric system configured for the MHD generator is based on the use of a common thruster screen supply with individual static-circuit interrupters for each thruster.

The interrupters operate immediately upon the development of a fault and series inductors provide the energy necessary to clear the fault, as well as providing momentary, transient circuit isolation during faults. In order to minimize system weight, it is assumed that electro-mechanical switches for permanent circuit interruption are not required.

Each individual thruster screen is fed from the common high voltage bus at the thrusters through a series network consisting of a high speed electronic switch (SCR) and a series reactor (L). The SCR interrupts the circuit between screens in the event of arcs within the thrusters, as detected by a sudden drop in voltage at the screems, the appearance of voltage across the series reactor, L, or some other signal. Following circuit interruption by the SCR, energy stored in L continues to supply power to the arc for a period of up to two milliseconds. The SCR remains off for a period of 0.2 seconds to allow time for the arc to clear and the thruster conditions to return to normal. After 0.2 seconds, the SCR is again switched on, re-establishing screen voltage and hopefully restoring full thruster operation. If, for example, the arc re-strikes two more times within a short period of time, the screen supply to that thruster and the inputs to the auxiliary power supplies for that thruster are permanently disconnected. This thruster is considered completely disabled and one of the six spare thrusters is placed automatically into operation to replace it.

During the spacecraft coast period when the thrusters are not required to operate, power to the thrusters is disconnected by the static switches in the screen supplies and by the contractors in the input circuits to the auxiliary thruster power supplies.

A simplified schematic diagram of the static switch used as the screen circuit interrupter is shown in Figure 2-46. A number of SCR's are connected in series to withstand the high voltage of the screen supply, and there are resistor networks across the SCR's and the resistor-capacitor networks to provide for proper steady state and transient voltage division.

In order that a common screen supply be feasible several factors must be considered. If all screens are fed from a common supply all are interconnected electrically. Hence, it is necessary that such interconnection be compatible with the complete electrical system, including the thruster auxiliary power conditioners. Also, it must be possible to isolate individual thrusters from the common supply in the event that the thrusters fail on momentary arc-over.

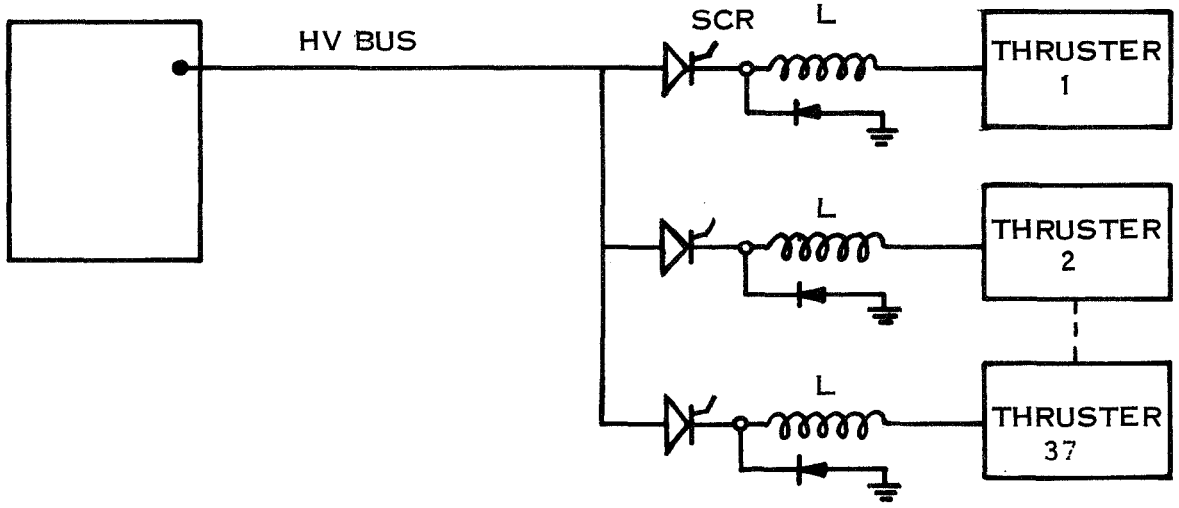

Figure 2-46. Individual Screen Circuit Interruption

2.7.4.7 Auxiliary Power Conditioning

2.7.4.7.1 EM Pump Power Conditioning - Direct current conduction electromagnetic pumps have been initially selected for use with the MHD generator system. These pumps require very high current at very low voltage, specifically, for the primary pump, 5000 amperes at 0.5 volt. Special, additional power conditioning equipment, therefore, is necessary. Using conventional power conversion schemes for very low voltage, efficiencies of less than 50 percent are encountered. With ac-dc conversion, the voltage drop in the output rectifiers approximates or exceeds the output voltage required and hence the efficiency is poor.

In order to obtain the extremely low dc output voltage required at the pumps, standard low-voltage conversion to a higher output voltage is performed and several pumps are connected in series. Now, with the rectifiers dropping 0.7 volts dc and the output typically 10 volts dc, an efficiency or approximately 90 percent is realizable.

Two power conditioners are used in the system. One feeds the cesium pump which requires 25 kWe. The other feeds the startup pump, auxiliary pump, the shield pump, and the propellant pump, requiring an

estimated 1.3 kWe total. The cesium pump is assumed to be divided into 20 parallel fluid ducts, requiring 0.5 volts for each duct, all connected in series. The conditioner would have an efficiency of 90 percent as previously mentioned.

The remaining pumps are single duct machines, which when connected in series require a power conditioner to supply 1.3 kW at 2.0 volts dc. Efficiency for this supply would be approximately 65 percent, but for this relatively low power level the loss would be about 0.7 kW.

A standard 8 pound/kWe output has been applied for weight estimation for the main EM pumps. The characteristics of the power conditioning for the EM pumps are summarized on Table 2-22.

TABLE 2-22. AUXILIARY POWER CONDITIONING CHARACTERISTICS

COMPONENT APPLICATION	POWER INPUT kWe	POWER CONDITIONER EFFICIENCY PERCENT	WEIGHT POUNDS	POWER LOSSES WATTS(e)
Main EM Pumps	27.8	90	220	2800
Auxiliary EM Pumps	2.0	65	12	700
MHD Generator Control	2.1	95	15	105
System Control	0.50	95	10	25
Spacecraft Guidance Control	0.50	95	10	25
Special Ion Engine Units	16.1	95	272	---*
Payload Units	1.0	95	1.0	50
Totals			549	3705

* Included in ion engine allocation

An important consideration in making the initial decision to use dc conduction pumps was the reactive power weight penalty occasioned by using ac induction pumps. For example, considering the five pumps in the system, using three-phase ac power, required an estimated 1150

pounds for power conditioning. This would be approximately equivalent to 30 pounds/kVA, which with a 0.55 power factor would be about 50 pounds/kW. Largely, the weight would be increased due to the capacitors necessary for correction of the power factor and to the cabling cross-sectional area increase necessary to handle the reactive volt-amperes. Further study will be performed with the dc/ac pump trade-off.

2.7.4.7.2 Other Auxiliary Power Conditioning - Auxiliary power conditioning is also required for the following operations:

a. MHD generator control

b. System control

c. Special ion engine units

d. Spacecraft guidance and control

e. Payload

The weight of the power conditioning for all these units, except the special ion engine units, is greater than the 8 pounds/kWe output employed for the main EM pumps because of the smaller size of these special purpose units, as shown on Table 2-22. The weights presented for the special ion thruster units are those provided by JPL. The efficiency of these auxiliary units is as shown on Table 2-22. No losses are shown for the special ion engine units, since this power loss is already factored into the ion thruster efficiency, used to calculate the beam power.

3. CONCLUSIONS

The following conclusions are drawn.

1. The calculations of system parameters requires iterative use of the two programs MHDGN and MHDCY. In addition, desired parameters such as MHD generator weight and radiator weight are not calculated directly. It would be very useful if these two programs could be combined and modified to calculate significant weight values directly.

2. The one-loop MHD system appears to be more attractive than a two-loop configuration, although the effects of fission product leakage from reactor fuel elements has not been evaluated. The effects of such leakage should be evaluated.

3. In order to shut down the MHD system during the flight coast period and Jupiter operations, it would be necessary to provide an auxiliary power system of approximately 30 kWe output. The inclusion of shutdown and restart capability and a separate power system requires a more complex plant design. On the other hand, it is not unreasonable to assume that the MHD system can be operated at reduced power levels. If it cannot, a relatively small power-flattening shunt can be incorporated.

4. The triform geometry appears most attractive for the direct condensing vapor chamber radiator, since auxiliary structure is most easily incorporated and most easily jettisoned from it. The radiator net weight can then be minimized for both launch and electric-propelled flight.

5. The Configuration No. 4 of Section 2.6 with the MHD equipment up near the reactor is the most attractive basis for development of the baseline design.

6. The temperature difference between the MHD generator windings and the auxiliary cooling fluid and radiator is not yet sufficiently defined for spacecraft design detail to proceed.

7. The rectangular channel vapor chamber using sodium is the most attractive design for the primary radiator.

8. The interface between MHD generator output and the electrical power and distribution system needs more definition.

4. RECOMMENDATIONS

The following recommendations are made based on the first quarter's work and the specific conclusions drawn in Section 3.

1. Combine the MHDGN and MHDCY programs into a single program to calculate MHD parameters, with additional subroutines to calculate MHD generator weights and radiator area and weights.

2. Assume a one-loop system for the baseline MHD system, but evaluate the effects of reactor fuel element leakage.

3. Assume that the MHD system will operate at partial power level.

4. Use the triform geometry for the baseline design primary radiator.

5. Use Configuration No. 4 as the model for the baseline spacecraft.

6. Complete the MHD generator cooling analysis to determine a realistic temperature difference between windings and coolant.

7. Base the radiator design on rectangular channel vapor chambers with sodium fluid.

8. Investigate and clarify the electrical interface and interactions between the MHD generator and the power distribution system.

5. NEW TECHNOLOGY

No new technology items have been identified.

6. REFERENCES

1. GESP-7011, A Design Study For a Thermionic Reactor Power System For a Nuclear Electric Propelled Unmanned Spacecraft, Quarterly Progress Report Number 1, May 23, 1969.

2. Thrust Subsystem Design for Thermionic-Electric Spacecraft Study, JPL Memo T. Masek to N. Simon, February 20, 1969.

3. Elliott, David G., "Variable-Velocity MHD Induction Generator With Rotating-Machine Internal Electrical Efficiency", AIAA Journal, Volume 6,Number 9, pp. 1695 - 1702, September 1968.

4. Elliott, D. G. et. al., "Theoretical and Experimental Investigation of Liquid-Metal MHD Power Generation," Electricity from MHD, Volume II, International Atomic Energy Agency, Vienna, 1966, pp. 995 - 1018.

5. Personal Communication Dr. D. G. Elliott to R. M. Bernero, September 2, 1969.

6. GESP-7013, A Design Study For a Thermionic Reactor Power System For a Nuclear Electric Propelled Unmanned Spacecraft, Quarterly Progress Report No. 2, August, 1969.

7. GE-PIR Number U-1K25-072, J. Garrity,J. Cokonis to W. Z. Prickett, Addendum To Structural/Dynamic Analysis of Thermionic Spacecraft Configurations, August 4, 1969.

8. PWAC-445, Preliminary Design of the 2 MWt Reactor and Shield (PWAR-20) For The SNAP-50/SPUR Powerplant, December 30, 1964.

9. PWAC-643, SNAP-50/SPUR Program Engineering Progress Report, July 1, 1964 to September 30, 1964.

10. PWAC-457, 35 and 300 kWe SNAP-50/SPUR Powerplants For The Manned Orbiting Space Station Application.

APPENDIX I

Computation of Variable-Velocity MHD Induction Generator Performance (Program GENERATOR)

by

D. G. Elliott

Jet Propulsion Laboratory
California Institute of Technology
Pasadena, California

Appendix I
Computation of Variable-Velocity MHD Induction Generator Performance (Program GENERATOR)

D. G. Elliott
Jet Propulsion Laboratory

This document describes the assumptions, analysis, and procedures employed in calculating generator efficiency and other performance parameters for a variable-velocity MHD induction generator with the slip and field varied to provide an internal electrical efficiency equal to that of a rotating generator. End losses are suppressed by compensating poles and electrically-insulating vanes.

The analysis is the one presented in Ref. 1, with a modified winding arrangement and with equations for additional parameters. The computer program for the analysis is GENERATOR.

I. GENERATOR DESCRIPTION

The generator analyzed is shown in Fig. 1, a drawing of the 325-kW lithium generator discussed in Ref. 1. The design shown is intended for use with a surface-impingement separator and is unsymmetrical, with the cesium vapor exhaust on one side and the slot for the upstream compensating pole on the other. The generator used with an impinging-jet separator would be sym-

metrical and have the upstream compensating winding in two slots like the downstream winding, and this is an option in the program.

Referring to Fig. 1, the lithium, with some cesium vapor, leaves the separator and enters the capture slot of the generator. In the upstream diffuser the pressure of the mixture is raised to dissolve the cesium. The upstream diffuser is also the upstream compensating pole region, and it contains axial insulating vanes for suppression of shunt end currents and eddy currents from the compensating field.

The liquid stream leaving the upstream compensating pole flows through the traveling-wave region of the generator (the 24.9-cm center section of the generator in Fig. 1). The traveling-wave region has a polyphase winding in slots in the upper and lower laminated-iron stator blocks and has copper electrodes on each side (canned in a refractory metal) for axially completing the fluid current loops.

After leaving the traveling-wave region, at reduced velocity, the lithium flows through the downstream compensating pole region which, like the upstream compensating pole region, has insulating vanes for suppression of electrical losses. The downstream compensating pole region also serves as the inlet section of the downstream diffuser.

II. GENERATOR ANALYSIS ASSUMPTIONS

The assumptions employed in analyzing the generator are as follows:

1. The slip and the field are varied to maintain rotating-machine internal electrical efficiency $\eta_0 = (1 + s)^{-1}$ at each point, where s is the slip $(U - U_s)/U_s$ between the fluid velocity U and the magnetic field wave velocity U_s.
2. The pressure is constant from inlet to exit of the traveling-wave region.

3. The losses in the generator consist only of (1) fluid ohmic losses from the fluid current necessary for the required retarding force, (2) shunt end currents and eddy currents in the compensating poles, (3) wall friction, (4) winding loss, and (5) the increase in those losses due to the limitations on field amplitude and slot area from iron saturation. There are no losses from: (1) variation of magnetic field and current density across the height of the channel, (2) boundary layer currents, (3) increased friction due to MHD effects, (4) ohmic losses in the copper side-electrodes, (5) departure of the magnetic field from sinusoidal waveform, and (6) eddy currents in the walls.

Assumption 1 requires the generator to operate with the product of field and wave velocity, BU_s, held constant from the inlet to the exit of the traveling-wave region. With this constraint, the current in the fluid is the same at every point as it would be in a constant-velocity generator and the efficiency of power generation in the fluid is $(1 + s)^{-1}$ at every point. The possible disadvantage of a constant-BU_s design is that the field in the upstream part of the generator must be lower than would be optimium at the same fluid velocity in a constant velocity generator, because of the reduced upstream field required to maintain BU_s = constant while not saturating the iron at the downstream end. The possibility of higher overall efficiency with a departure from the constant-BU_s case assumed here has not been explored.

Assumption 2, constant pressure in the traveling-wave region, is adopted for simplicity. There is a possibility of higher cycle efficiency with a pressure rise in the generator, because of lower velocity and friction loss and because of reduced pressure recovery requirement in the downstream diffuser, but pressure-rise operation has not been explored.

Assumption 3 is the key one. Five loss mechanisms are adopted as being

the only significant ones. All other losses, six of which are enumerated, are assumed to be negligible. The arguments for neglecting the six losses enumerated will be reviewed briefly.

1. Field and current density variation across the channel height

The efficiency of a constant-velocity generator using the exact field equations (both x and y variations accounted for) was calculated by Pierson (Ref. 2) and the results compared with the "slit-channel case" ($B_x = 0$ and $B_y = \text{const}$) assumed here. Pierson found negligible efficiency decrease using the exact equations when $\pi b/L \ll 1$, where b is the channel height and L is the wavelength. In a typical lithium generator such as the one in Fig. 1, the value of $\pi b/L$ is 0.2, and there was no more than 0.1% efficiency loss at this value in Pierson's analysis.

2. Boundary-layer currents

Boundary-layer currents of high density flow in the near-stationary part of the fluid near the wall. If the velocity profile is a fully-developed 1/7-power profile extending to the center of the channel, then the internal electrical efficiency cannot exceed 0.78 (Ref.3). But there is evidence (Ref. 4) that the velocity profile is highly flattened in the generator, in which case the boundary-layer shunt currents may cause only negligible losses. There is also the possibility of designing the generator with a wall that is retracted from the boundary of the flow, giving a "free-jet" effect which could further flatten the velocity profile.

3. Friction increase

Friction increase due to MHD effects has been studied and found to exist, but only by about 10% at ratios of Reynolds number to Hartmann number of interest in this application. To account for this and other possible effects, a factor of increase in friction of 1.3 is employed in the program.

4. Side-electrode losses

The ohmic losses in the canned copper side-electrodes can be reduced as much as desired by giving them a large cross section, but at some point they begin to interfere with the coils. Thus, this loss reduces to an optimization problem between coil loss and axial-conductor loss. Preliminary design studies have indicated that the side electrodes can have sufficient area for negligible loss if skin effect is not too great, but further studies are required.

5. Non-sinusoidal waveform

The loss due to the finite number and width of the winding slots was analyzed in Ref. 5. An efficiency loss of 3 percentage points was calculated for the generator of Fig. 1 employing 24 slots, instead of the 12* shown. The calculations were pessimistic in that they did not consider the smoothing out of the waveform that occurs in practice due to fringing. Hence, a 15 deg spacing between slots can be expected to give negligible loss compared with a continuous current sheet.

6. Wall currents

Operation without wall currents requires achievement of a wall which is both thermally and electrically insulating. A slotted, cesium-purged refractory-metal wall with ceramic between it and the stator, and a vacuum interface with the stator, is the present concept.

The net effect of excluding the six losses enumerated is to make the calculations optimistic by an amount which might only be a few percentage points but could be much larger. Pending further experiments, the present analysis will be considered to predict the generator performance ultimately achievable after careful development.

* 11 actual TW slots plus a half sector at each end with the currents included in the end slot currents

III. ANALYSIS

The program is based on the analysis presented in Ref. 1. The only change is that the slots are spaced in increments of current-angle Ψ that are evenly divisible into 180 deg, thus permitting the downstream slots to be in series with the upstream slots. With this arrangement, the number of phases is half the number of slots. The "nominal" number of slots is 360 divided by the slot spacing $\Delta\Psi$ in deg. The actual number of slots is a few less because the current span of the winding is less than 360^{o}. The last traveling-wave slot is the last slot which has a sector entirely inside the traveling-wave region; if a slot sector extends beyond the end of the traveling-wave region, that slot is deleted and the previous slot becomes the last slot.

In the following analysis, only the equations added to the Ref. 1 analysis will be derived. The others will merely be recopied in the form used in the program.

A. Input Quantities

The specified quantities are:

$\dot{m}$ = flow rate

U_1 = inlet velocity to the traveling-wave region

U_2 = exit velocity from the traveling-wave region

c = channel width

ρ = fluid density

μ = fluid viscosity

σ = fluid electrical conductivity

I_{ec_1} = eddy-current ampere-turns in the upstream compensating pole

I_{ec_2} = eddy-current ampere-turns in the downstream compensating pole

L_{c_1} = length of the upstream compensating pole

L_{c_2} = length of the downstream compensating pole

b_{c_1} = mean channel height in the upstream compensating pole

b_{c_2} = mean channel height in the downstream compensating pole

b_w = minimum (exit) channel wall thickness

α = ratio of winding loss (including iron loss) to solid-fill DC loss of slot portion of coils

T_c = coil temperature

B_s = saturation field of the iron

N = nominal number of slots

B_1 = rms field at the inlet of the traveling-wave region

B. General Calculations

1. Flow-dependent quantities and coil conductivity

The inlet height of the traveling-wave region is

$$b_1 = \frac{\dot{m}}{\rho U_1 c} \tag{1}$$

and the exit height is

$$b_2 = \frac{\dot{m}}{\rho U_2 c} \tag{2}$$

The inlet hydraulic diameter is

$$D_h = 4 \frac{\text{Area}}{\text{Perimeter}}$$

$$= \frac{2 b_1 c}{b_1 + c} \tag{3}$$

The inlet Reynolds number is

$$Re = \frac{\rho U_1 D_h}{\mu} \tag{4}$$

Substituting U_1 from Eq. (1) and D_h from Eq. (3) the Reynolds number is

$$Re = \frac{2\dot{m}}{\mu(b_1 + c)} \tag{5}$$

The skin friction factor C_f is one quarter of the pipe friction factor f, which can be calculated from the Prandtl relation, Eq. (6-56) of Ref. 6. Multiplying by 1.3 to cover any increase due to MHD effects, the skin friction coefficient is

$$C_f = \frac{1.3}{[4 \log_{10}(2 \text{ Re } C_f^{\frac{1}{2}}) - 1.6]^2} \tag{6}$$

In Ref. 1, the factor (1 + b/c) accounting for the small contribution of side-wall friction is dropped from the friction equation and assumed included in C_f. Therefore, C_f is corrected by the average factor.

$$C_{f_{corr}} = C_f \left[1 + \frac{b_1 + b_2}{2c}\right] \tag{7}$$

The fluid input power to the traveling-wave region is the kinetic energy change.

$$P_m = \frac{\dot{m}}{2} (U_1^2 - U_2^2) \tag{8}$$

The traveling-wave iron gap is assumed in Ref. 1 to be constant. The required gap is the exit height plus twice the exit wall thickness.

$$g = b_2 + 2b_w \tag{9}$$

The compensating pole iron gaps are

$$g_{c_1} = b_{c_1} + 2b_w \tag{10}$$

and

$$g_{c_2} = b_{c_2} + 2b_w \tag{11}$$

The electrical conductivity of copper at 20°C is 1.7241 μ ohm-cm, and the temperature coefficient is 0.00393 $^{\circ}C^{-1}$. Hence the coil

conductivity in mho/m is

$$\sigma_w = \frac{10^8}{1.7241\,[1 + 0.00393(T_c - 20)]} \tag{12}$$

2. Inlet-field-dependent quantities

The inlet Hartman number, a measure of the ratio of electrical to friction forces, is given by Eq. (35) of Ref. 1,

$$H_{a_1} = \left(\frac{\sigma\, b_1\, B_1^2}{\rho\, U_1\, C_f}\right)^{\frac{1}{2}} \tag{13}$$

The optimum inlet slip, the value that balances friction loss against ohmic loss for maximum internal efficiency at the inlet, is given by Eq. (34) of Ref. 1.

$$s_1 = (1 + H_{a_1}^2)^{-\frac{1}{2}} \tag{14}$$

With the inlet slip known, the inlet values of the slip-dependent factors in Eqs. (38), (39), and (40) of Ref. 1 can be calculated. The slip-dependent factor in the x-equation, Eq. (38), is

$$Z_1(s) = s^{\frac{1}{2}}(1 + s)^{\frac{1}{2}} - \tfrac{1}{2} \ln\left\{\left[\frac{(1 + s)^{\frac{1}{2}}}{s^{\frac{1}{2}}} - 1\right] \Big/ \left[\frac{(1 + s)^{\frac{1}{2}}}{s^{\frac{1}{2}}} + 1\right]\right\} \tag{15}$$

The slip-dependent factor in the P_0-equation, Eq. (39) of Ref. 1, is

$$Z_2(s) = 4 \sin^{-1}\left(\frac{1 + s}{2}\right)^{\frac{1}{2}} + \frac{(2 + s)(1 - s)^{\frac{1}{2}}}{(1 + s)^{\frac{1}{2}}} \tag{16}$$

The slip-dependent factor in the θ-equation, Eq. (40) of Ref. 1, is

$$Z_3(s) = \sin^{-1} s - \ln\left[\frac{1 + (1 - s^2)^{\frac{1}{2}}}{s}\right] + (1 - s^2)^{\frac{1}{2}} \tag{17}$$

(The last term was misprinted with a minus sign in Ref. 1.)

The values of these three factors at s_1 are Z_{1_1}, Z_{2_1}, and Z_{3_1}, respectively.

The inlet wave velocity from the definition of slip, Eq. (5) of Ref. 1, is

$$U_{s_1} = \frac{U_1}{1 + s_1} \tag{18}$$

The exit slip making $B_2\ U_{s_2}$ equal to $B_1\ U_{s_1}$ can be calculated from Eq. (37) of Ref. 1. Setting $U = U_2$ and $s = s_2$ in that equation and rearranging, s_2 can be expressed as

$$s_2 = s_1 \left[\frac{(1 + s_1)(1 - s_2)}{(1 - s_1)(1 + s_2)}\right]^{\frac{1}{2}} \left(\frac{U_2}{U_1}\right)^2 \tag{19}$$

This equation can be solved by iteration, successively substituting s_2 on the right side, with $s_2 = s_1$ as the initial guess.

The frequency is found by substituting $\theta = 2\pi$ and $s = s_2$ in Eq. (40) of Ref. 1 and solving for ω.

$$\omega = \frac{4\ \pi\ U_1\ H_{a_1}\ C_f}{b_1\ (1 + s_1)[Z_{3_1} - Z_3(s_2)]} \tag{20}$$

The gross output power, the power generated in the fluid, is given by Eq. (39) of Ref. 1.

$$P_0 = \frac{\dot{m}\ U_1^2}{2s_1}\left(\frac{1 - s_1}{1 + s_1}\right)^{\frac{1}{2}} [Z_{2_1} - Z_2(s_2)] \tag{21}$$

The voltage induced by the gap flux in each coil turn is given by Eq. (28) of Ref. 1.

$$V_0 = c\ B_1\ U_{s_1} \tag{22}$$

The inverse of the first factor in Eq. (40) of Ref. 1 is

$$K_1 = \frac{2\ C_f\ U_1\ H_{a_1}}{\omega\ b_1\ (1 + s_1)} \tag{23}$$

The first factor in Eq. (38) of Ref. 1 is

$$K_2 = \frac{b_1}{2 C_f} \left(\frac{1 + s_1}{H_{a_1}} \right)^{\frac{1}{2}} \tag{24}$$

C. Slip and Coordinate for Each Slot Sector

The generator is divided into 2N equal increments of current angle, Ψ, where Ψ is the ωt difference between the instant of peak winding current at x = 0 and the instant of peak winding current at the x-coordinate of interest. Thus, at position K the current angle is

$$\Psi = \frac{K \pi}{N} \tag{25}$$

Slots 0, 1, 2, 3,$\cdots$ are located at K = 0, 2, 4, 6,$\cdots$. The boundaries of the sector served by slot 0 (by the traveling-wave component of the current in that slot) are at K = 0 and 1. The boundaries of the sector served by slot 1 (K = 2) are at K = 1 and 3. The boundaries of the sector served by slot 2 (K = 4) are at K = 3 and 5, and so on. The sector boundaries are indicated by the vertical tick marks along the x-axis in Fig. 1. If the generator has 12 slots, as in Fig. 1, the last slot is at K = 24 and the traveling-wave component of the current in that slot serves the sector bounded by K = 23 and K = 24.

From Eq. (26) of Ref. 1, the field angle at the K'th position is

$$\theta = \Psi + \beta_1 - \beta \tag{26}$$

where β is the upstream phase shift of the winding current peak from the field zero due to the fluid current, and β_1 is the value of β at the inlet. Substituting Ψ from Eq. (25), the field angle is

$$\theta = \frac{K \pi}{N} + \beta_1 - \beta \tag{27}$$

The one exception is the last slot, for which $\theta = 2\pi$. In the generator program, values of θ are calculated from Eq. (26) for K = 0, 1, 2,$\cdots$ until a value of K is encountered for which $\theta > 2\pi$, showing that the end of the traveling-

wave region has been passed. The winding is then terminated in one of two ways: (1) if K is even, the slot for that K is moved upstream to $\theta = 2\pi$, and the last slot number is K/2; (2) if K is odd, the last previous slot is moved downstream to $\theta = 2\pi$, and the last slot number is (K - 1)/2. The sketch below shows the first type of termination, for a case where $\theta > 2\pi$ is encountered at K = 46.

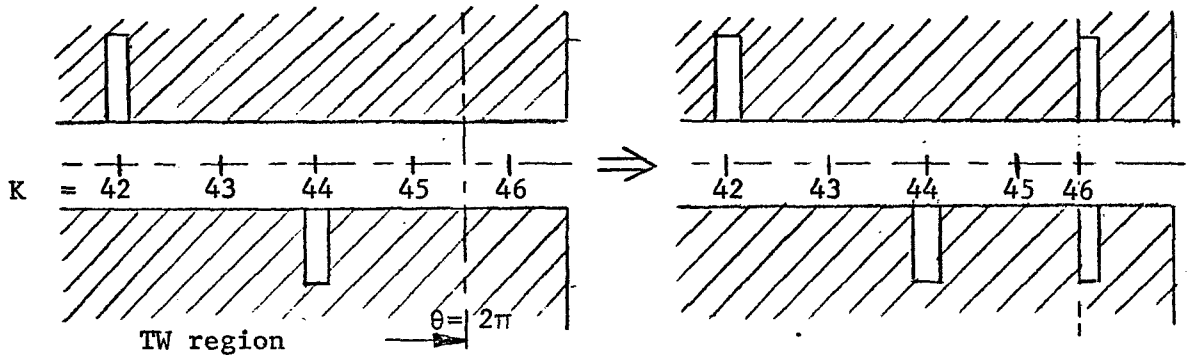

Termination with even K

The effect is to shorten the half-sector served by the traveling-wave component of the current in the last slot.

The sketch below shows the second type of termination, for a case where $\theta > 2\pi$ is encountered at K = 45.

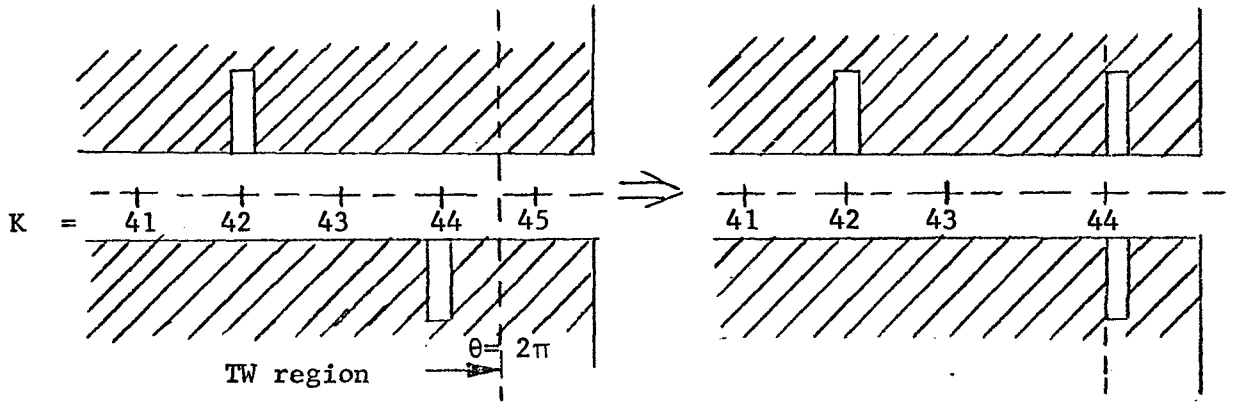

Termination with odd K

The effect is to lengthen the half-sector served by the traveling-wave component of the current in the last slot, but at most to one full sector width. The reason is to avoid having to cut a slot in the stator block less than a half-sector width from the end, as would be the case if a slot were cut at the

original K = 44 position (left, above) and then another slot cut at $\theta = 2\pi$ for the compensating winding. The desired termination is done in the program by setting

$$K = K - K \bmod 2 \tag{28}$$

and

$$\theta(K) = 2\pi \tag{29}$$

when a K value is encountered for which $\theta > 2\pi$. Thus, in the first sketch above, K = 46 - 46 mod 2 = 46 - 0 = 46. In the second sketch, K = 45 - 45 mod 2 = 45 - 1 = 44. (In Step 4.10 of the program, where this is done, Eq. (28) is written with K - 1 in place of K on the right side, because K is incremented once beyond the $\theta > 2\pi$ value on leaving Step 4.05.)

With θ known, the slip at the K'th position can be calculated from Eq. (40) of Ref. 1. The equation can be partially solved for s as follows.

$$s = \exp\left(Z_{3_1} - Z + \ln(1 + Z) - \tan^{-1}(s/Z) - K_1\theta\right) \tag{30}$$

where $Z = (1 - s^2)^{\frac{1}{2}}$ and Z_{3_1} and K_1 are the constants given by Eqs. (17) and (23), respectively.

Eq. (30) can be solved iteratively by successively substituting s on the right side starting with the s value for the previous K as the initial guess.

Next, the fluid velocity at K is calculated from Eq. (37) of Ref. 1.

$$U = U_1 \left[\frac{(1 - s_1)(1 + s)\, s^2}{(1 - s)(1 + s_1)\, s_1^2}\right]^{\frac{1}{4}} \tag{31}$$

The fluid channel height is

$$b = \frac{\dot{m}}{\rho U c} \tag{32}$$

The wave velocity, from Eq. (5) of Ref. 1, is

$$U_s = \frac{U}{1 + s} \tag{33}$$

The field required for constant BU_s, from Eq. (6) of Ref. 1, is

$$B = \frac{B_1 U_{s_1}}{U_s} \tag{34}$$

The rms fluid current per unit length is given by Eq. (10) of Ref. 1.

$$I'_f = \sigma b B U_s s \tag{35}$$

The total (winding plus fluid) current per unit length can be considered to be made up of two conponents: (1) the current required for a constant field of rms value B and (2) the current required for the field gradient dB/dx. The first component is given by Eq. (22) of Ref. 1.

$$I'_B = \frac{g B \omega}{\mu_0 U_s} \tag{36}$$

The second component is given by Eq. (23) of Ref. 1.

$$I'_{\Delta B} = \frac{g (dB/dx)}{\mu_0} \tag{37}$$

For constant BU_s, dB/dx is equal to $-(B/U_s)\, d/dx\, [U/(1 + s)]$. The derivative can be evaluated from Eqs. (37) and (38) of Ref. 1. After considerable algebraic manipulation, the result is

$$I'_{\Delta B} = \frac{g B_1 U_{s_1}^2 H_{a_1} C_f}{\mu_0 b_1 (1 - s^2)^{\frac{1}{2}} U_s^2} \left[1 - \frac{2s(1 - s)}{1 + s - s^2}\right] \tag{38}$$

The phase shift β is given by Eq. (25) of Ref. 1.

$$\beta = \tan^{-1}\left(\frac{I'_f - I'_{\Delta B}}{I'_B}\right) \tag{39}$$

If this value does not agree with the value assumed in calculating θ from Eq. (27), the new value is substituted in Eq. (27) and the steps from Eq. (27)

to Eq. (39) are repeated. An exception is the last slot where it is not necessary to iterate for θ since θ is specified as 2π.

Finally, the x-coordinate at K is calculated from Eq. (38) of Ref. 1.

$$x = K_2 [z_{1_1} - Z_1(s)] \tag{40}$$

D. Winding Calculations

The current in each slot is made equal to the required winding current per unit length at the slot position times the length of the sector to be served by the slot. The sector length for the (J/2)'th slot (K/2 is now the number of the last slot) is

$$\Delta x = x(J + 1) - x(J - 1) \tag{41}$$

For the first slot (J = 0) the sector length is $\Delta x = x(1)$, and for the last slot (J = K) the sector length is $\Delta x = x(K) - x(K - 1)$. Eq. (41) provides the correct values of Δx if $x(-1)$ and $x(K + 1)$ are set equal to 0 and $x(K)$, respectively.

1. Traveling-Wave Slot

From Eq. (24) of Ref. 1 and the definition of β, Eq. (25) of Ref. 1, the winding current per unit length is related to the two components of the total current according to the following phasor diagram.

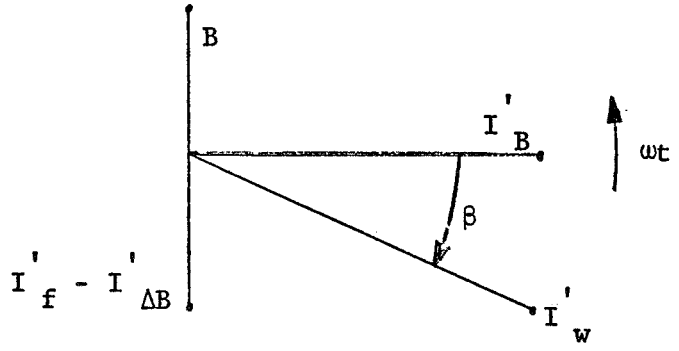

It can be seen that the winding current per unit length is

$$I'_w = \frac{I'_B}{\cos \beta} \tag{42}$$

Hence, the winding current in a traveling-wave slot is

$$I_w = \frac{I'_B \Delta x}{\cos \beta} \tag{43}$$

The base width of the slot is given by Eq. (31) of Ref. 1.

$$w_1 = 2\Delta x(1 - B_m/B_s) \tag{44}$$

where B_m is the peak field, $B/\sqrt{2}$, and the B_s is the saturation field of the iron.

The slot shape is parabolic, and the depth of the slot if the sides extended until they met at a sharp point would be the value given by Eq. (32) of Ref. 1.

$$D = \frac{B_s w_1^2}{\sqrt{2}\, \mu_0 I_w \sin \Delta\Psi} \tag{45}$$

where $\Delta\Psi$ is the current angle increment per sector $2\pi/N$.

The slot can be truncated to 75% of D with only an 8% loss of area. Furthermore, most of the winding loss occurs in the last few slots; therefore, all of the slots can be truncated to 75% of the depth of the last inboard slot ($J = K - 2$) with little penalty in winding loss. Accordingly, the depth of all the slots is set at

$$D_0 = 0.75\, D(J = K-2) \tag{46}$$

For the parabolic shape the width at any distance y from the sharp-pointed bottom is $w = w_1(y/D)^2$. Hence the width of the truncated bottom is

$$w_2 = w_1 \left(1 - \frac{D_0}{D}\right)^2 \tag{47}$$

The area of the slot with the sharp bottom is $w_1 D/3$, and the area removed by truncation is $w_2(D - D_0)/3$. Hence, the area of the truncated slot is

$$A = [w_1 D - w_2(D - D_0)]/3 \tag{48}$$

Eq. (61) of Ref. 3 gives the average voltage per turn induced by the slot flux in a sharp-pointed parabolic slot. The slot flux voltage is little different for a truncated slot. The voltage is

$$V_s = 0.4\, V_0 \left| \frac{B_s}{\sqrt{2}B} - 1 \right| \tag{49}$$

where V_0 is the gap-flux voltage given by Eq. (22).

2. End Slot

The end slot currents required for the compensating field are given by Eq. (27) of Ref. 1. In addition, the end slots carry the traveling-wave currents for the first and last sectors. From Eq. (24) of Ref. 1 the traveling-wave currents in the first and last slots, $\theta = 0$ and 2π, respectively, are

$$I_{w_{0,K}} = I'_B \Delta x \cos \omega t + (I'_f - I'_{\Delta B}) \Delta x \sin \omega t \tag{50}$$

To maintain the desired compensating field in the presence of the eddy currents I_{ec_1} and I_{ec_2} in the compensating pole regions, the end slot current must be changed by $-I_{ec_1}$ upstream and $-I_{ec_2}$ downstream, in phase with the eddy currents. The peak positive upstream eddy current occurs when the upstream compensating field is zero and increasing. This takes place at $\omega t = \pi/2$; hence, the counterbalancing winding current required is

$$\Delta I_{w_1} = -I_{ec_1} \sin \omega t \tag{51}$$

The peak positive downstream eddy current occurs when the downstream compensating field is zero and decreasing. This takes place at $\omega t = \pi/2$, and the counterbalancing winding current required is

$$\Delta I_{w_2} = -I_{ec_2} \sin \omega t \tag{52}$$

Adding the compensating current from Eq. (27) of Ref. 1, the traveling-wave current from Eq. (50), and the eddy-current counterbalancing currents from Eqs. (51) and (52), the total end-slot currents are

$$I_{\frac{1}{2}} = \left[(I'_f - I'_{\Delta B})\, \Delta x \mp \frac{g\, B_1}{\mu_0} - I_{ec_{\frac{1}{2}}} \right] \sin \omega t + \left[I'_B\, \Delta x + \frac{g_{c_1}\, B_1\, U_{s_1}}{\mu_0\, \omega\, L_{1_{\frac{2}{2}}}} \right] \cos \omega t$$

$$= I_a \sin \omega t + I_b \cos \omega t \tag{53}$$

In Ref. 1, g_{c_1} and g_{c_2} are assumed equal to g, the traveling-wave gap, and the upstream and downstream compensating pole areas are assumed equal, $A_{c_1} = cL_1 = A_{c_2} = cL_2$. Eq. (27) of Ref. 1 is still

valid, however, with unequal gaps and areas and is so used in Eq. (53).

The angle between the total current and the cosine component is adopted as the angle reference for the end slot currents.

$$\beta_c = \tan^{-1}(I_a/I_b) \tag{54}$$

The rms magnitude is then

$$I = \frac{I_b}{\cos \beta_c} \tag{55}$$

The end slots can be made rectangular and tilted outward as required to avoid saturation. The width is arbitrarily made equal to the compensating pole length or to the slot depth, whichever is least. The two cases are sketched below.

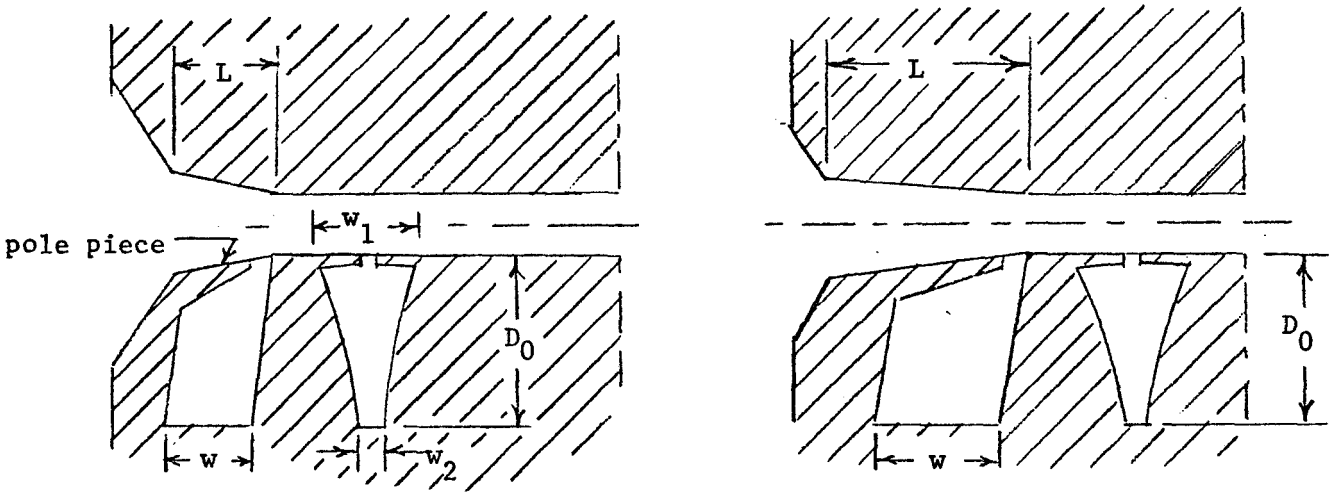

$L < D_0 \Rightarrow w = L$ $\qquad$ $L > D_0 \Rightarrow w = D_0$

The slot area, neglecting the pole piece, is

$$A = w D_0 \quad \text{(one slot)}$$

or

$$A = 2w D_0 \quad \text{(two slots)} \tag{56}$$

The voltage induced by the slot flux is derived using the sketch below.

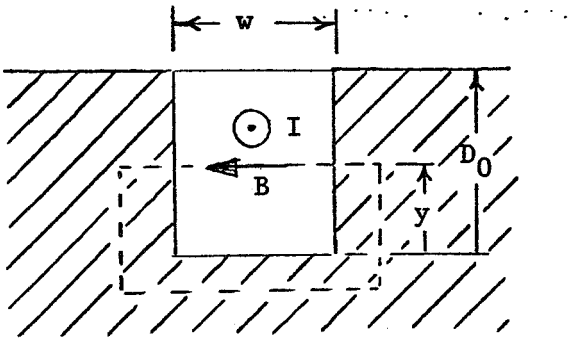

The current inside the loop is Iy/D_0. The field at y is, therefore,

$$B = \frac{\mu_0 I y}{D_0 w} \tag{57}$$

The flux linking a winding turn at y is

$$\phi = \int_y^{D_0} c B \, dy$$

$$= \frac{\mu_0 c I (D_0^2 - y^2)}{2 w D_0} \tag{58}$$

and the voltage induced in that turn by the slot field is

$$V(y) = \omega \phi \tag{59}$$

If there are N turns in the slot the total coil voltage is

$$V = \int_0^{D_0} V(y) \frac{dy}{D_0/N} \tag{60}$$

Substituting Eqs. (58) and (59) into Eq. (60) and integrating, the mean slot-flux voltage per turn is

$$\frac{V_s}{N} = \frac{\mu_0 \omega c I D_0}{3 w} \tag{61}$$

3. Winding Loss

The ohmic loss that would occur in one slot if the area A were solidly filled with copper and the AC/DC resistance ratio were unity would be $c I_w^2/\sigma_w A$. To account for partial fill, for ohmic loss in

the portion of the coil outside the slot, for AC/DC resistance ratio greater than unity, and for the iron loss, the solid-fill DC slot loss is multiplied by a factor of increase α. The total winding loss is then

$$P_w = \sum_{j=0}^{k} \frac{\alpha\, c\, I_w^2}{\sigma_w A} \tag{62}$$

E. Power Output and Efficiency

The net electric output from the traveling-wave region is

$$P_{e_{TW}} = P_0 - P_w \tag{63}$$

The net output from the generator as a whole is reduced from $P_{e_{TW}}$ by the amount of the eddy-current losses in the compensating pole regions, and this subtraction is made in the cycle program. The efficiency of the traveling-wave portion of the generator is defined as

$$\eta_{TW} = \frac{P_0 - P_w}{P_m} \tag{64}$$

This equation completes the analysis needed for purposes of cycle analysis.

F. Additional Details for Slot Sectors

The gross power output from the fluid in sector J is given by Eq. (39) of Ref. 1.

$$\Delta P_0 = \frac{\dot{m}\, U_1^2}{2\, s_1} \left(\frac{1 - s_1}{1 + s_1}\right)^{\frac{1}{2}} [Z_2(s_{J-1}) - Z_2(s_{J+1})] \tag{65}$$

From Eq. (36) of Ref. 1 the local internal efficiency is $(1 - s)/(1 + s)$. Hence the fluid input power in sector J is

$$\Delta P_m = \Delta P_0 \left(\frac{1 + s}{1 - s}\right) \tag{66}$$

The local electrical efficiency is $(1 + s)^{-1}$. Hence, the fluid input power due to electrical retarding force is

$$\Delta P_{m_e} = \Delta P_0 (1 + s) \tag{67}$$

From the equations for dP_r and dP_0 presented following Eq. (11) of Ref. 1, the fluid ohmic loss in sector J is

$$\Delta P_r = \Delta P_0 \, s \tag{68}$$

The friction loss is the difference between ΔP_m and ΔP_{m_e}.

$$\begin{aligned} \Delta P_f &= \Delta P_0 (1 + s) \left(\frac{1}{1 - s} - 1 \right) \\ &= \Delta P_r \left(\frac{1 + s}{1 - s} \right) \end{aligned} \tag{69}$$

The power induced in each slot is equal to the product of the gap-flux voltage V_0 (which is the same for every slot) and the in-phase component of the slot current. From Eqs. (1) and (28) of Ref. 1 the voltage V_0 is 180 deg out of phase with the field, as sketched below.

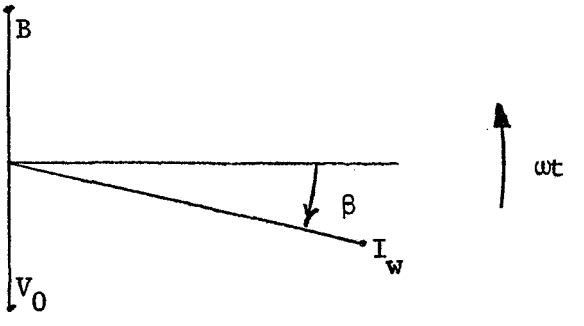

The power induced in the slot is

$$\Delta P_i = V_0 \, I_w \sin \beta \tag{70}$$

Comparing Eq. (28) of Ref. 1 with Eq. (53), the voltage V_0 is in phase with the I_a component of the end slot current. The voltage-current relationships are sketched below.

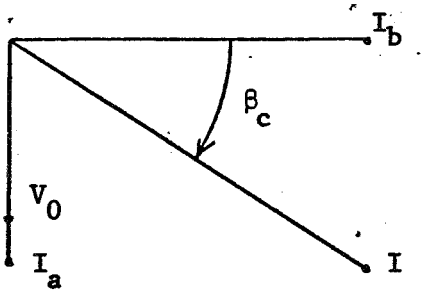

The induced power is

$$\Delta P_i = V_0 \, I \sin \beta_c \quad * \tag{71}$$

The winding loss in sector J is

$$\Delta P_w = \frac{\alpha \, \sigma \, c \, I \, \omega^2}{\sigma_w \, A} \tag{72}$$

The net power output from sector J is

$$\Delta P_e = \Delta P_i - \Delta P_w \tag{73}$$

The reactive power due to the gap flux is V_0 times the out-of-phase component of I_w. The reactive power due to the slot flux is the product of the mean slot-flux voltage from Eq. (49) or Eq. (61) and the slot current. The total reactive power in sector J is

$$\Delta P_q = V_0 \, I_w \cos \beta + V_s \, I_w \tag{74}$$

with $\beta = \beta_c$ at the end slots.

The angle between the current and the voltage at the coil terminals is

$$\beta_{I\text{-}V} = \tan^{-1} \frac{P_q}{P_e} \tag{75}$$

The terminal voltage per turn is the value V such that VI_w is the vector sum of P_e and P_q. Thus

$$V = \frac{P_q}{I_w \sin \beta_{I\text{-}V}} \tag{76}$$

---

* In the program the summation of ΔP_i includes the fluid eddy-current losses in the compensating poles and is less than P_0 by the amount of those losses, within a small error due to the more precise calculation of P_0 from the exact integral relation.

G. End-Slot Spacing

The required iron widths on the traveling-wave and outboard sides of the end slots, w_5 and w_6, respectively, can be calculated from the peak flux to be carried. The geometry is sketched below.

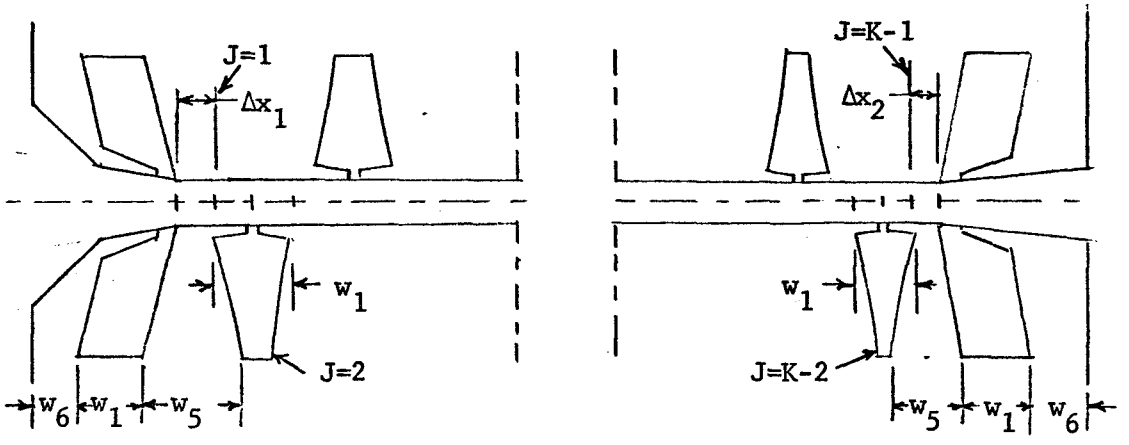

Only the iron widths for the bottom stator block need be calculated since the lower block has the smaller end-tooth widths.

The gap flux passing through the tooth between the end slot and the adjacent traveling-wave slot is

$$\phi_{g_{\frac{1}{2}}} = \sqrt{2}\, B_{\frac{1}{2}}\, (2\Delta x_{\frac{1}{2}})\, c \tag{77}$$

The width of iron that will carry this flux at saturation is $w_3 = \phi/cB_s$. Hence,

$$w_{3_{\frac{1}{2}}} = \frac{\sqrt{2}\, B_{\frac{1}{2}}\, (2\Delta x_{\frac{1}{2}})}{B_s} \tag{78}$$

The peak flux through the end slot is given by Eq. (58) with y = 0.

$$\phi_1 = \frac{\sqrt{2}\,\mu_0\, c\, I_1\, D_0}{2\, w_{1_1}} \quad \text{(one slot)} \tag{79}$$

$$= \frac{\sqrt{2}\,\mu_0\, c\, I_1\, D_0}{4\, w_{1_1}} \quad \text{(two slots)} \tag{80}$$

$$\phi_2 = \frac{\sqrt{2}\,\mu_0\, c\, I_2\, D_0}{4\, w_{1_2}} \tag{81}$$

The required iron widths are

$$w_{0_{\substack{1\\2}}} = \phi_{1_2}/(cB_s) \tag{82}$$

The required iron width for the adjacent traveling-wave slot would be half the base width w_1 if the slot continued to a sharp point since the sharp-pointed slot is based on saturation of the iron all the way to the bottom. Neglecting the small change of slot flux with truncation, the iron widths required for the traveling-wave slots adjacent to the end slots are

$$w_{4_{\substack{1\\2}}} = \tfrac{1}{2}\, w_{1_{\substack{J=2\\J=K-2}}} \tag{83}$$

The sketch below shows the phasor diagram for the currents in the upstream end slot and adjacent traveling-wave slot and for the upward (positive) flux at the root of the intervening tooth expressed in terms of the saturated iron widths w_0, w_3 and w_4.

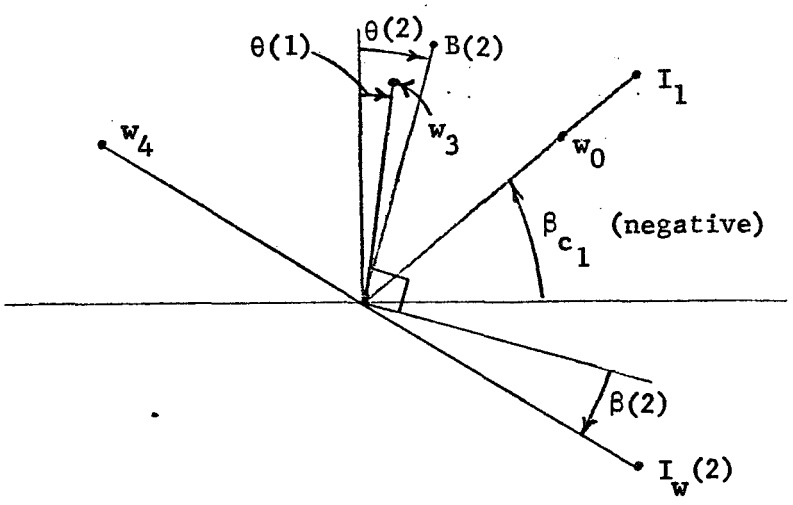

The upward flux giving rise to the w_3 requirement is in phase with the gap field at $\theta_{J=1}$. The upward flux giving rise to the w_0 requirement is in phase with I_1, and the upward flux giving rise to the w_4 requirement is 180 deg out of phase with $I_{w_{J=2}}$. From the diagram it can be seen that the vector sum of the iron requirements for the tooth to the right of the upstream slot is

$$w_{5_1} = \left\{ w_3 \cos\left[\frac{\pi}{2} - \theta(1) \right] + w_0 \cos \beta_{c_1} - w_4 \cos[\theta(2) + \beta(2)] \right\} \cos \omega t$$

$$- \left\{ w_3 \sin\left[\frac{\pi}{2} - \theta(1) \right] - w_0 \sin \beta_{c_1} + w_4 \sin [\theta(2) + \beta(2)] \right\} \sin \omega t \qquad (84)$$

$$= x \cos \omega t - y \sin \omega t \qquad (85)$$

The magnitude of the iron width requirement between the upstream slot and the adjacent traveling-wave slot is, therefore,

$$w_{5_1} = (x^2 + y^2)^{\frac{1}{2}} \qquad (86)$$

The rms compensating flux, from Eq. (8) of Ref. 1, is

$$\phi_c = \frac{c\, B_1\, U_{s_1}}{\omega} \qquad (87)$$

and, from Eq. (22),

$$\phi_c = \frac{V_0}{\omega} \qquad (88)$$

The iron requirement for this flux is

$$w_c = \frac{\sqrt{2}\, V_0}{\omega\, c\, B_s} \tag{89}$$

The phasor diagram for the flux on the left side of the upstream slot is sketched below.

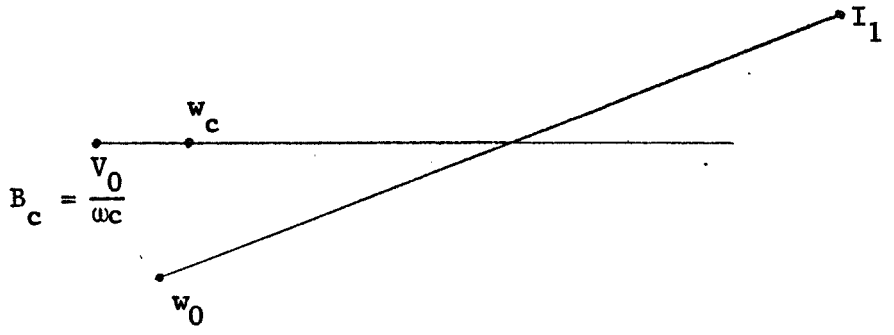

The vector sum of the iron requirements for the slot and compensating fluxes is

$$w_{6_1} = w_0 \cos \beta_{c_1} + \frac{\sqrt{2}\, V_0}{\omega\, c\, B_s} \tag{90}$$

The sketch below shows the phasor diagram for the currents in the downstream end slot and adjacent traveling-wave slot and for the upward (positive) flux at the root of the intervening tooth, expressed in terms of the saturated iron widths w_0, w_3, and w_4.

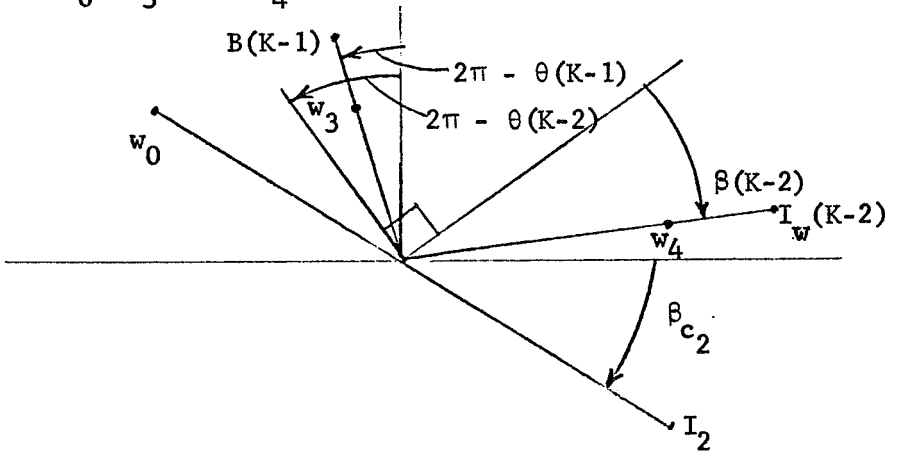

The vector sum of the iron requirements for the tooth is

$$w_{5_2} = \left\{ w_3 \cos\left[\frac{\pi}{2} - \theta(K-1) \right] - w_0 \cos \beta_{c_2} + w_4 \cos[\theta(K-2) + \beta(K-2)] \right\} \cos \omega t$$

$$- \left\{ w_3 \sin\left[\frac{\pi}{2} - \theta(K-1) \right] + w_0 \sin \beta_{c_2} - w_4 \sin[\theta(K-2) + \beta(K-2)] \right\} \sin \omega t \quad (91)$$

The phasor diagram for the flux on the right side of the downstream slot is sketched below.

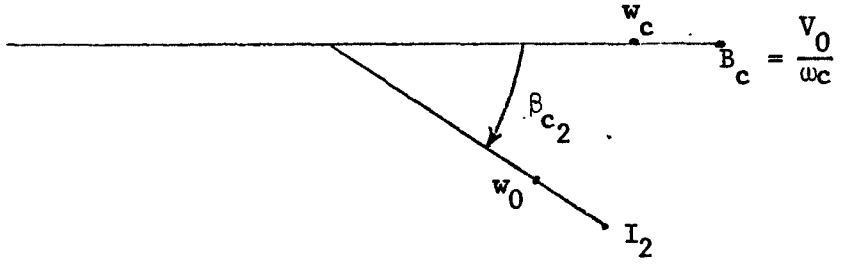

The iron requirement is

$$w_{6_2} = w_0 \cos \beta_{c_2} + \frac{\sqrt{2}\, V_0}{\omega\, c\, B_s} \quad (92)$$

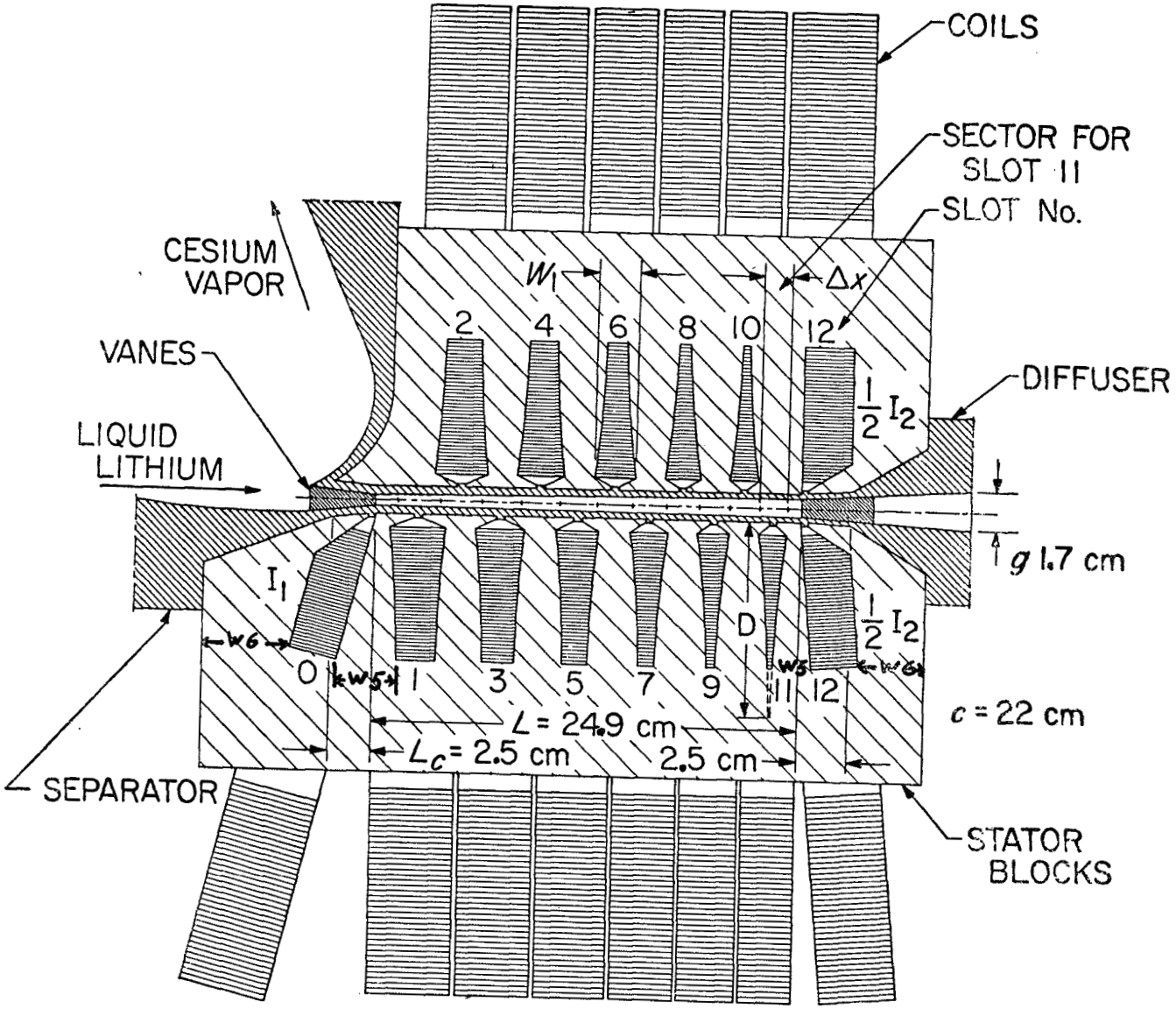

Fig. 1 Compensated, variable-velocity, lithium generator with 325 kW output.

APPENDIX II

Cycle Analysis of a Cesium-Lithium MHD Power System with an Impinging-Jet Separator (Program CYCLE-B)

by

D. G. Elliott

Jet Propulsion Laboratory
California Institute of Technology
Pasadena, California

Appendix II

Cycle Analysis of a Cesium-Lithium MHD Power System with an Impinging-Jet Separator (Program CYCLE-B)

D. G. Elliott

Jet Propulsion Laboratory

This document describes the assumptions, analysis, and procedures employed in calculating cycle efficiency and other performance parameters for a cesium-lithium MHD power system with an impinging-jet separator. The computer program for the analysis is CYCLE-B.

I. CYCLE DESCRIPTION

A cesium-lithium MHD power system with an impinging-jet separator is shown schematically in Fig. 1.

Liquid lithium and liquid cesium enter a pair of two-phase nozzles and mix at low velocity and high pressure. Heat transfer from the lithium to the cesium vaporizes the cesium. The two-phase mixture expands to low pressure at the nozzle exits, accelerating the liquid lithium to high velocity.

The two-phase jets from the nozzles impinge on each other at an angle, and the inward momentum drives the lithium drops together to form a coalesced two-phase jet of substantially reduced vapor void fraction.

The jet enters the upstream diffuser where the pressure of the cesium-lithium mixture is increased until the cesium is dissolved in the lithium. The liquid stream then enters the generator.

In the generator the stream of lithium (containing a few percent of cesium) is decelerated by electromagnetic retarding force. The force is adjusted to leave sufficient velocity for the lithium to flow through the downstream diffuser to the pressure required at the inlet of the heat source. The lithium is reheated in the heat source and returned to the nozzles.

The cesium vapor leaving the impinging-jet separator flows to a recuperator where the cesium is desuperheated, and where the lithium vapor is condensed, to the extent permitted by the heat sink capacity of the liquid cesium leaving the cesium pump.

The remaining cesium superheat is removed in a desuperheater. The saturated cesium vapor is condensed in the condenser, and the condensate is pumped to the liquid side of the recuperator by the cesium pump. After being heated in the recuperator the cesium is returned to the nozzles.

II. CYCLE-ANALYSIS ASSUMPTIONS

The assumptions employed in analyzing the cycle are as follows:

1. The concentration of cesium dissolved in the lithium is the equilibrium value for the prevailing temperature and pressure at each point in the system.
2. The nozzle exit conditions are those given by the two-phase, two-component nozzle program of Ref. 1.
3. Any liquid lithium entrained with the cesium vapor leaving the separator is separated out and returned to the impinging jets or elsewhere in the lithium loop before the cesium vapor enters the recuperator.
4. A compensated AC generator is used, and the compensating poles coincide with the upstream diffuser and with the vaned portion of the downstream diffuser.

5. The losses in the upstream diffuser consist of: (1) friction on the walls and insulating vanes (used for electrical loss reduction) corresponding to 1.3 times flat-plate skin friction and (2) electrical losses due to the AC compensating field of the generator.
6. The efficiency of the downstream diffuser without vane-friction or electrical losses is 0.85.
7. The additional losses in the downstream diffuser are: (1) friction on the insulating vanes corresponding to 1.3 times flat-plate skin friction and (2) electrical losses due to the AC compensating field of the generator.
8. There are no electrical losses in the walls of the upstream or downstream diffusers, or in the generator channel, due to the AC generator.
9. The pressure in the generator is constant from inlet to exit.
10. The temperature difference between the cesium vapor entering the recuperator and the liquid cesium leaving the recuperator is 50°K.
11. The cesium pump is driven by electric power from the MHD generator, and all power dissipated is transferred to the cesium being pumped.
12. The heat rejected by the cycle is the heat required to cool and condense the cesium vapor from the recuperator exit condition to the saturated liquid state at the condenser exit pressure, including the heat required to cool the small amount of lithium mixed with the cesium.
13. The radiating temperature at each point in the desuperheater and condenser radiators is equal to the local fluid temperature , and the emissivity is 0.9.
14. The pressure drop across the nozzle injection orifices is 5 psi, and the injection velocity is 30 ft/s.

Assumption 1, equilibrium cesium dissolving, implies transfers of several percent of cesium into and out of liquid solution in fractions of a millisecond. No information is available on cesium-lithium solution rate, and the validity of this assumption is not known. If equilibrium concentration did not occur, the nozzle performance would be improved but the efficiency of the diffusers would be decreased. Calculations assuming non-dissolving cesium in a system with a surface-impingement separator showed that the two effects would be about equal and the cycle efficiency with non-dissolving cesium would be about the same as with equilibrium dissolving. With an impinging-jet separator, however, the upstream diffuser losses with non-dissolving cesium would probably be unacceptable without some added mechanical removal of cesium vapor from the jet before entering the capture slot. Thus, the rate of cesium dissolving affects the design of the system, but it probably does not greatly affect overall cycle efficiency.

Assumption 2, the validity of nozzle exit conditions from Ref. 1, is well verified by experiments with water-nitrogen mixtures. Uncertainties in cesium-lithium properties, including the dissolving rate, could change the nozzle exit velocity a few percent from the values given by the nozzle program.

An additional requirement for Assumption 2 to be valid is that the separator duct must have about 40% more area than the nozzle exit to allow radial expansion of the cesium jet as its velocity equalizes with that of the slower liquid jet.

Assumption 3 requires removal from the cesium exhaust of a liquid flow equal to 0.5 to 1.0% of the nozzle liquid flow rate, in the case of the best present surface-impingement separators. Several times as much lithium might have to be removed with an impinging-jet separator where a curved target is not available for collecting the smaller drops. A satisfactory method of

returning the collected liquid to the lithium stream with an impinging-jet separator has not yet been demonstrated; reinjection into the impinging jets causes increased dispersion. The penalty of liquid remaining with the cesium might be preferable, since the recuperator liquid-side sink capacity would increase almost as much as the added heat load, falling short only by the 50° K minimum ΔT (Assumption 10). A velocity reduction factor is one of the inputs to the cycle analysis program, and with this factor the user can supply any penalty believed attributable to returning the lithium from the cesium exhaust. Supplying a factor of 1.0 implies that either there is no liquid loss or that all lithium is returned and remixed at full velocity with the impinging jets.

Assumption 4, the utilization of an AC induction generator, represents the best choice both for generator efficiency and ease of power conditioning. A DC generator might be thought to offer better efficiency, but the voltage across the channel in a DC generator causes shunt end currents extending farther upstream and downstream than can be suppressed by insulating vanes of reasonable length. An AC generator, on the other hand, operates at ground potential throughout the fluid, except locally in the compensating poles where relatively short insulating vanes can suppress the losses.

The second part of Assumption 4, overlapping of the compensating poles and diffusers, represents a logical combining of processes within a single region to reduce friction losses.

Assumption 5 restricts the upstream diffuser losses to 1.3 x flat-plate friction, plus electrical losses from the compensating flux. The friction losses observed in the limited tests conducted to date with vaned upstream diffusers could be correlated by applying a factor of between 2 and 3 to

flat-plate friction, or they could be correlated by an impact loss in which all of the flow intercepted by the 14 0.02-in. thick vanes (5% of the total flow) was stagnated. Another source of loss, and perhaps the most likely, is two-phase slip or shock effects at the diffuser entrance. Whatever the loss source, Assumption 5 postulates a reduction in upstream diffuser loss from an observed 2.5 x, to an assumed 1.3 x, flat-plate friction.

The electrical losses included in Assumption 5 are calculated by a procedure which agreed roughly with some limited data on a small-scale generator, but accurate experiments on the fluid electrical losses in the compensating poles are lacking.

Assumption 6, an efficiency of 0.85 for the downstream diffuser before adding vanes and electrical losses, is well verified by liquid diffuser experiments (Ref. 2).

Assumption 7 for the losses added to the downstream diffuser by the vanes and electrical effects has the same uncertainties as Assumption 5, but to a lesser extent because only liquid flow is involved.

Assumption 8, no electrical losses in the walls, is contingent on development of a thermally insulating, electrically insulating wall which exposes only metal to the lithium stream. A possible design is an axially-slotted metallic wall, purged by cesium vapor flowing into the lithium stream with ceramic between the wall and the generator stators and a vacuum interface with the stators for low heat transfer. Assumption 8 implies such a wall, with sufficiently fine spacing of slots (say 1 cm) for negligible eddy-current loss, and with negligible cesium purge flow or some non-flow method of preventing shorting between the wall segments.

Assumption 9, constant pressure in the generator, is adopted for simplicity.

Assumption 10, 50°K minimum recuperator ΔT, should allow adequate heat flux at the hot end. The ΔT at the cold end is typically 200-300°K because of the lithium condensation on the vapor side.

Assumption 11 specifies a cesium pump design utilizing power from the AC generator either directly or after rectification, with the electrical components at the cesium temperature. If lower electrical temperatures were employed there would be a requirement for radiation of some power at the lower temperature, but the cesium sink capacity would increase by an equal amount and there would be no change in cycle heat rejection.

Assumption 12 limits the heat rejection considered to that from the cesium vapor (and the lithium vapor mixed with it) only. Additional heat losses from cooling of the generator and other components and from stray losses are not considered in the heat balance or cycle efficiency.

Assumption 13, isothermal radiation at the local fluid temperature, is adopted merely to provide a basic radiator area. The area can be multiplied by additional factors to account for fluid and fin ΔT's.

Assumption 14, 5 psi injection pressure drop, is a value at which stable nozzle operation has been demonstrated. The assumed inlet velocity of 30ft/s, required only in calculating the nozzle inlet area (the effect on exit velocity is negligible), corresponds to 2.0 psi dynamic pressure of the lithium, and should be attainable with 5 psi injector pressure drop.

III. INPUTS

A. Inputs to Cycle Program From User

The twenty independent variables adopted for the cycle analysis are the following, listed in the order of input to the CYCLE-B program:

T_1 = nozzle inlet temperature

r_c = ratio of lithium flow rate to cesium flow rate in the nozzle

($T_{1\,nozzle}$ and r_c are supplied to the program as a single variable, the case number.)

A_2/A^* = ratio of nozzle exit area to nozzle throat area

c/h_2 = ratio of nozzle exit width to height

P_e = net electric power output

θ = nozzle impingement half-angle

K_v = factor for adjusting upstream diffuser inlet velocity to account for non-ideal separator behavior

r_{v_3} = ratio of gas volume flow rate to liquid volume flow rate at the upstream diffuser inlet

L_1/c = ratio of upstream compensating pole length (upstream diffuser length) to width

L_2/c = ratio of downstream compensating pole length (downstream vane length) to width

N_1 = number of upstream vane channels

N_2 = number of downstream vane channels

η_p = cesium pump efficiency

$\Delta p_{6,7}$ = pressure drop across the heat source

$\Delta p_{8,10}$ = pressure drop between the separator exit and the condenser inlet

$\Delta p_{12,13}$ = pressure drop across the liquid side of the recuperator

$\Delta p_{10,11}$ = pressure drop across the condenser

η_g = efficiency of the traveling-wave region of the generator

f = generator frequency

ϕ_c = compensating pole flux

Based on limited data, the three separator parameters can be tentatively set at θ = 15 deg, $K_v = 1$, and $r_{v_3} = 3$, assuming the nozzle exit aspect ratio is not too far from the present test value, say $c/h_2 = 3.5$. The four diffuser parameters L_1/c, L_2/c, N_1, and N_2 are not freely variable but should be adjusted to minimize end losses. The three generator parameters η_g, f, and ϕ_c can be specified but are more usefully left as variables to be supplied by program GENERATOR. Thus the analysis at present actually employs nine

independent variables: the nozzle conditions T_1, r_c, and A_2/A^*; the net power output P_e; the pump efficiency η_p; and the four pressure drops $\Delta p_{6,7}$, $\Delta p_{8,10}$, $\Delta p_{12,13}$, and $\Delta p_{10,11}$.

B. Inputs to Cycle Program from Nozzle Program

Nozzle throat area and a table of nozzle flow conditions versus pressure are supplied as inputs to the cycle analysis after the inlet conditions T_1 and r_c (actually the corresponding nozzle case number) are specified.

The quantities furnished from the nozzle program are as follows:

A^* = nozzle throat area (at $\dot{m}_t$ = 100 lb/s)

D_2 = exit drop diameter

$\overline{V}$ = mass-weighted mean velocity

A = flow area

$\overline{A}$ = flow area after equilization of liquid and gas velocities

$\overline{T}$ = temperature after equilization of liquid and gas temperatures

One value of A^* and D_2 is supplied for each nozzle case. The other quantities are supplied for a range of pressures covering the possible exit pressures of interest.

For the nozzle calculations themselves, additional quantities must be supplied as discussed next.

C. Inputs to Nozzle Program

The nozzle program is the two-phase, two-component program described in Ref. 1, with the options of drop breakup and specified p(x) selected. Quantities that must be supplied to the nozzle program are as follows:

T_1 = nozzle inlet temperature

r_c = lithium/cesium component ratio

p_1 = nozzle inlet pressure

H = inverse Henry's Law constant

$\dot{m}_t$ = total flow rate

V_1 = nozzle inlet velocity

D_1 = inlet lithium drop diameter

Tabulated fluid properties are furnished and a table of pressure versus distance through the nozzle is given.

The inlet pressure p_1 is the vapor pressure of a saturated cesium-lithium solution at temperature T_1. This pressure, according to data reported in Ref. 5, is the same as the sum of the vapor pressures of unmixed cesium and lithium for temperatures up to 1900°F, then falls 10 psi below at 2000°F. Table I presents the nozzle inlet pressures used in the available nozzle calculations. The pressures are 4 - 10 psi below the values that would be used based on Ref. 6. Also listed are the values of the inverse Henry's Law constant H calculated from Fig. 2 of Ref. 8. That figure gives α as a function of T_1 where α is the saturation concentration of cesium in the liquid; H is calculated from α using Eq. (A-4) of Appendix A. The α values are included in Table I.

The inlet velocity V_1 employed in the available nozzle calculations is V_1 = 50 ft/s instead of V_1 = 30 ft/s as adopted here for consistency with a 5 psi injection pressure drop; changing V_1 to 30 ft/s in the nozzle calculations would have negligible effect on the exit conditions and has not been done.

The total flow rate in the nozzle calculations is $\dot{m}_t$ = 100 lb/s, and this is used in the cycle analysis only to determine the nozzle size required for the actual flow rate.

The inlet drop diameter is chosen large enough to give breakup in the nozzle, D_1 = 0.05 in.

The fluid properties employed in the nozzle program are a compilation made in 1964. Employing the newer properties adopted for the cycle analysis (Ref. 6) would not significantly change the nozzle results.

The curve of pressure versus distance furnished to the nozzle program is one which gives the same pressure ratio versus distance as the curve in Fig. 7 of Ref. 1. This p(x) curve corresponds to a nozzle length of about 40 in. from the 30 ft/s point to an area 2.7 times the throat area. A nozzle length of 100 in. would give 1-2 % higher velocity.

The flow of information between the cycle, nozzle, and generator programs, and between the programs and the user, is diagrammed in Fig. 2.

IV. ANALYSIS

A. Nozzle Exit (Station 2)

From the specified nozzle area ratio A_2/A^*, the nozzle exit conditions can be determined by interpolating in the table of $\overline{V}$, A, $\overline{A}$, and $\overline{T}$ versus p furnished for the T_1, r_c, case specified. Other flow conditions required at the nozzle inlet and exit for the cycle analysis can then be calculated from p_1, T_1 and from p_2, T_2 $(=\overline{T})$, respectively, using the equations presented in Appendix A.

From the specified output power P_e and specified nozzle exit width/height ratio c/h_2, an initial estimate can be made of the required width of the nozzle, c. The width c is also the width of the separator, generator, and diffuser. With P_e in watts, the width in meters is estimated, as a first guess for iteration, from

$$c = 2.8 \times 10^{-4} \left[\left(\frac{c}{h_2} \right) P_e \right]^{\frac{1}{2}} \qquad (1)$$

The nozzle exit height is

$$h_2 = \frac{c}{c/h_2} \qquad (2)$$

The total nozzle exit area is $2h_2c$. The exit area A_2 from the nozzle program is the area corresponding to a total flow rate of $\dot{m}_t$ = 100 lb/s. Therefore, the liquid and gas flow rates calculated in Appendix A must be increased from the values calculated there by the factor

$$K = \frac{2h_2c}{A_2} \tag{3}$$

Experiments have indicated that actual flow rates are only 93% of the values given by the computer program (see Ref. 1, Figs. 26, 27, and 28). Therefore the factor is decreased to

$$K = \frac{0.93 \times 2h_2c}{A_2} \tag{4}$$

The inlet height of each nozzle, based on the total inlet area A_1 from Eq. (A-12) of Appendix A, is

$$h_1 = \frac{KA_1}{2c} \tag{5}$$

B. Impinging Jets (Station 2.1)

The liquid velocity at the nozzle exit is less than the mean velocity $\bar{V}$ because of slip between the phases, but the liquid is further accelerated downstream of the nozzles by the higher gas velocity. In Appendix B equations are derived for estimating the liquid velocity at distance L downstream from the nozzle exit given the ratio of exit area A to equalized-velocity area $\bar{A}$, drop diameter D_2, ratio of liquid flow rate to gas flow rate r, gas density ρ_g, and liquid density ρ_ℓ. The two effects accounted for are the finite distance required to accelerate a liquid drop and the radial displacement of gas from the liquid jet as the gas decelerates.

The value employed for the mean distance to impingement is the distance along each nozzle axis to the point of intersection with the midplane, as

sketched below:

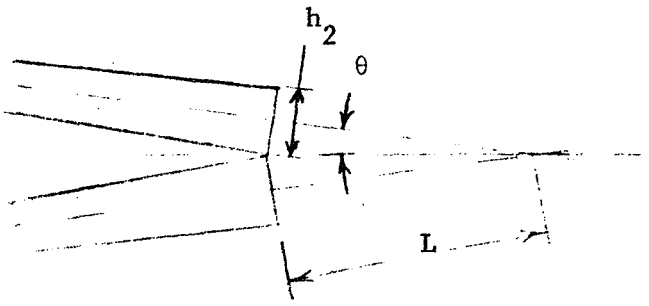

The mean distance to impingement is

$$L = \frac{h_2}{2 \tan \theta} \tag{6}$$

The velocity at impingement, $V_{2.1}$, is then given by Eq. (B-12).

C. Capture Slot (Station 3)

The velocity after impingement is the axial component of the velocity before impingement, times a factor K_v which can be used to specify velocity reductions from effects such as returning flow separated out from the cesium exhaust.

$$V_3 = K_v \, V_{2.1} \cos \theta \tag{7}$$

The temperature of the lithium is increased over $\bar{T}$ by the kinetic energy dissipated relative to $\bar{V}$.

$$T_3 = \bar{T} + \frac{\bar{V}^2 - V_3^2}{2 \, c_{Li_\ell}} \tag{8}$$

where

c_{Li_ℓ} = specific heat of liquid lithium from Eq. (G-24)

The capture slot area is equal to the mixture volume flow rate divided by the velocity.

$$A_3 = \frac{\dot{m}_{\ell_3} \left(1 + r_{v_3}\right)}{\rho_\ell V_3} \tag{9}$$

where

$\dot{m}_{\ell_3}$ = liquid flow rate entering the capture slot

r_{v_3} = specified gas/liquid volume ratio at the capture slot

ρ_ℓ = liquid density

The capture slot height, for zero vane thickness, is

$$h_3 = \frac{A_3}{c} \tag{10}$$

The actual height would have to be increased to account for vane thickness.

The flow rate of gas entering the capture slot is equal to the gas density times the gas volume flow rate.

$$\dot{m}_{g_3} = \frac{\rho_g A_3 V_3 r_{v_3}}{1 + r_{v_3}} \tag{11}$$

The gas flow rate leaving the separator and flowing to the recuperator is reduced by this amount.

$$\dot{m}_{g_8} = \dot{m}_{g_2} - \dot{m}_{g_3} \tag{12}$$

where

$\dot{m}_{g_8}$ = flow rate in the vapor loop (stations 8 through 13)

$\dot{m}_{g_2}$ = gas flow rate at the nozzle exit

The gas entering the capture slot dissolves, and the flow rate in the liquid loop (stations 4 through 7) is

$$\dot{m}_{\ell_4} = \dot{m}_{\ell_3} + \dot{m}_{g_3} \tag{13}$$

D. Upstream Diffuser Exit (Station 4)

The upstream diffuser flow is treated in two steps: (1) isentropic pressure rise to a pressure sufficient to dissolve all of the inlet cesium vapor, and (2) reduction of the exit velocity by friction and electrical losses. The isentropic flow equations are derived in Appendix C and the loss equations are derived in Appendix E (friction loss) and Appendix F (electrical losses).

The pressure for dissolving the cesium is given by Eq. (C-8), and the isentropic exit velocity is given by Eq. (C-13). The velocity loss due to friction and electrical losses is

$$\Delta V = \Delta V_f + \Delta V_e \tag{14}$$

where

ΔV_f = friction velocity loss from Eq. (E-11)

ΔV_e = electrical velocity loss from Eq. (F-21)

The diffuser exit velocity is

$$V_4 = V_{4_0} - \Delta V \tag{15}$$

where

V_{4_0} = isentropic (frictionless) exit velocity from Eq. (C-13)

The value of ΔV depends on the exit velocity. Hence Eq. (15) must be iterated until V_4 converges to the desired accuracy.

The diffuser exit height, again ignoring the vane thickness, is

$$h_4 = \frac{\dot{m}_{\ell_4}}{V_4 \rho_\ell c} \tag{16}$$

The exit temperature is increased by the kinetic energy dissipated (the kinetic energy reduction beyond the amount going into pumping work $\Delta p/\rho_\ell$),

the eddy-current losses, and the heat given up by the dissolving cesium (assumed equal to the heat released on condensing).

$$T_4 = T_3 + \frac{1}{c_{Li_\ell}} \left(\frac{V_3^2}{2} + \frac{p_3}{\rho_\ell} - \frac{V_4^2}{2} - \frac{p_4}{\rho_\ell} + \frac{P_{ec} + \dot{m}_{g_3} L_{cs}}{\dot{m}_{\ell_3}} \right) \qquad (17)$$

where

P_{ec} = eddy current loss from Eq. (F-29)

L_{Cs} = latent heat of vaporization of cesium at temperature T_3, from Eq. (G-22)

E. Downstream Diffuser Inlet (Station 5)

The downstream diffuser flow is treated in two steps: (1) pressure rise to the specified exit pressure p_6 with diffuser efficiency 0.85 and (2) increase in inlet velocity due to vane friction and compensating-pole electrical losses. The first step is treated in Appendix D, and the loss equations for the second step are the same used in the upstream diffuser: friction from Appendix E and electrical losses from Appendix F.

From Appendix D the required diffuser inlet velocity without vanes or electrical losses is

$$V_{5_0} = \left(2 \frac{p_6 - p_5}{0.85\ \rho_\ell} \right)^{\frac{1}{2}} \qquad (18)$$

where $p_5 = p_4$ in accordance with Assumption 9.

The inlet velocity with losses is

$$V_5 = V_{5_0} + \Delta V \qquad (19)$$

where ΔV is the velocity change due to friction and electrical effects, Eq. (14). The velocity loss depends on the inlet velocity; hence, Eq. (19) must be iterated until the desired accuracy in V_5 is reached. In addition, a relation between the inlet velocity and the vane exit velocity is required,

and this is furnished by the area ratio K across the vane section.

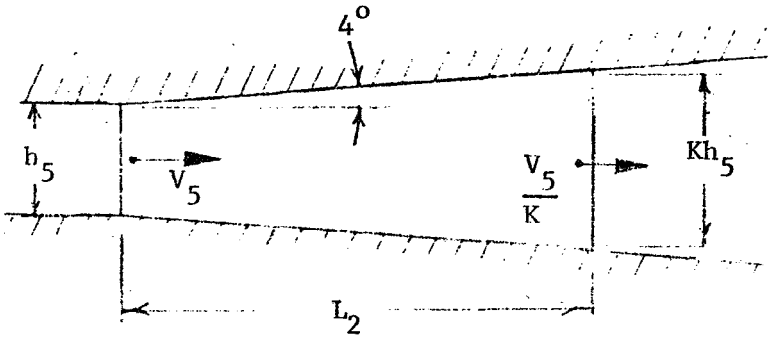

As shown in the sketch above, the vane exit velocity is V_5/K. Based on the specified L_2/c, and a 4 deg divergence half-angle,

$$K = 1 + \frac{2\ (L_2/c)\ c \tan 4^\circ}{h_5} \tag{20}$$

where h_5 can be estimated from

$$h_5 \cong \frac{h_4\ V_4}{V_{5_0}} \tag{21}$$

After finding V_5, the actual height is calculated from

$$h_5 = \frac{\dot{m}_{\ell_4}}{V_5\ \rho_\ell\ c} \tag{22}$$

F. Power and Efficiency

The fluid power available to the traveling wave region of the generator is

$$P_m = \frac{\dot{m}_{\ell_4}}{2}\left(V_4^2 - V_5^2\right) \tag{23}$$

The electric power required by the cesium pump is the fluid pumping power divided by the pump efficiency.

$$P_p = \frac{\dot{m}_{g_8} \left(p_{12} - p_{11} \right)}{\rho_{Cs_\ell} \eta_p} \tag{24}$$

where

ρ_{Cs_ℓ} = liquid cesium density from Eq. (G-18)

The net electric output from the generator is P_m times the efficiency of the traveling-wave region, minus the pump power and diffuser eddy current losses.

$$P_e = P_m \eta_g - P_{ec_1} - P_{ec_2} - P_p \tag{25}$$

where

η_g = efficiency of the traveling-wave region (specified, or supplied by generator program)

P_{ec_1} = eddy current loss in the upstream compensating pole from Eq. (F-29)

P_{ec_2} = eddy current loss in the downstream compensating pole from Eq. (F-29)

The value of P_e from Eq. (25) is compared with the specified output power, and if the two differ by more than the desired accuracy, the nozzle exit width is adjusted to

$$c_{new} = c \left(\frac{P_{e_{specified}}}{P_e} \right)^{\frac{1}{2}} \tag{26}$$

and the calculations are repeated starting with Eq. (2).

The temperature of the cesium leaving the pump, according to Assumption 11, is increased by the dissipated electric power.

$$T_{12} = T_{11} + \frac{P_p \left(1 - \eta_p \right)}{\dot{m}_{g_8} c_{Cs_\ell}} \tag{27}$$

The heat sink capacity of the liquid cesium and the small amount of lithium mixed with it, between the pump exit temperature T_{12} and the allowable recuperater exit temperature T_{13}, is

$$Q_\ell = \dot{m}_{g_8} \left[1 - \beta \right] \overline{c_{Cs_\ell}} + \beta \overline{c_{Li_\ell}} \left(T_{13} - T_{12} \right) \tag{28}$$

where

β = fraction of lithium mixed with the cesium, Eq. (A-5)

$\overline{c_{Cs_\ell}}$ = specific heat of liquid cesium at the mean temperature $(T_{12} + T_{13})/2$, from Eq. (G-23)

$\overline{c_{Li_\ell}}$ = specific heat of liquid lithium at the mean temperature $(T_{12} + T_{13})/2$, from Eq. (G-24)

The heat that must be rejected to condense the lithium vapor entering the recuperator and to cool the cesium vapor and the lithium condensate to the saturation temperature of cesium at the condenser inlet is

$$Q_v = \dot{m}_{g_8} \left\{ \left[(1 - \beta)\, \overline{c_p} + \beta\, \overline{c_{Li_\ell}} \right] \left(T_8 - T_{10} \right) + \beta\, L_{Li} \right\} \qquad (29)$$

where

$\overline{c_p}$ = mean specific heat of cesium vapor between superheat at T_8 and saturation at T_{10}, from Eq. (G-26)

$\overline{c_{Li_\ell}}$ = specific heat of liquid lithium at the mean temperature $(T_8 + T_{10})/2$, from Eq. (G-24)

L_{Li} = latent heat of vaporization of lithium at temperature T_8, from Eq. (G-27)

The desuperheat rejection Q_v always exceeds the liquid cesium sink capacity Q_ℓ. Therefore, there is an amount of heat remaining to be rejected by the desuperheater radiator equal to

$$Q_d = Q_v - Q_\ell \qquad (30)$$

The condenser heat rejection is equal to the heat rejected by condensing the cesium at temperature T_{10} plus the heat rejected by cooling the cesium condensate and lithium condensate to T_{11}, the saturation temperature at the condenser exit.

$$Q_c = \dot{m}_{g_8} \left\{ (1 - \beta)\, L_{Cs} + \left[(1 - \beta)\, c_{Cs_\ell} + \beta\, c_{Li_\ell} \right] \left(T_{10} - T_{11} \right) \right\} \qquad (31)$$

where L_{Cs}, c_{Cs_ℓ}, and c_{Li_ℓ} are evaluated at T_{10}.

The heat input to the cycle is equal to the sum of the heat rejected by the condenser, the heat rejected by the desuperheater, and the net electric output.

$$Q_h = Q_c + Q_d + P_e \tag{32}$$

The cycle efficiency is the ratio of net electric output to heat input.

$$\eta = \frac{P_e}{Q_h} \tag{33}$$

The power dissipated in the generator is $P_m(1 - \eta_g)$, and most of this power is dissipated in lithium friction and ohmic losses. The lithium temperature leaving the generator is, therefore, approximately

$$T_5 = T_4 + \frac{P_m\left(1 - \eta_g\right)}{\dot{m}_{\ell_4} c_{Li_\ell}} \tag{34}$$

The diffuser exit temperature is increased by the kinetic energy change, above pumping work, and by the downstream eddy current losses.

$$T_6 = T_5 + \frac{1}{c_{Li_\ell}}\left(\frac{V_5^2}{2} + \frac{p_5}{\rho_\ell} - \frac{p_6}{\rho_\ell} + \frac{P_{ec_2}}{\dot{m}_{\ell_4}}\right) \tag{35}$$

The heat source exit temperature is

$$T_7 = T_6 + \frac{Q_h}{\dot{m}_{\ell_4} c_{Li_\ell}} \tag{36}$$

The desuperheater inlet temperature is

$$T_9 = T_{10} + \frac{Q_d}{\dot{m}_{g_8}\left[(1-\beta)\,\overline{c_p} + \beta\, c_{Li_\ell}\right]} \tag{37}$$

where

$\overline{c_p}$ = mean specific heat of cesium vapor between superheat at T_9 and saturation at T_{10}

Since $\overline{c_p}$ depends on T_9, Eq. (37) must be iterated until T_9 converges to the desired accuracy.

The areas of the desuperheater and condenser radiators are, respectively,

$$A_d = \frac{Q_d}{\sigma \epsilon T_{eff_d}^4} \tag{38}$$

and

$$A_c = \frac{Q_c}{\sigma \epsilon T_{eff_c}^4} \tag{39}$$

where

σ = Stefan-Boltzman constant

= 5.6697×10^{-8} W m^{-2} $^oK^{-4}$ (Ref. 7, p.5)

ϵ = emissivity

= 0.9 (Assumption 13)

T_{eff_d} = effective radiating temperature between T_9 and T_{10} from Eq. (H-6)

T_{eff_c} = effective radiating temperature between T_{10} and T_{11} from Eq. (H-6)

Table I

Inlet Conditions Employed

in Nozzle Program

T_1	T_1	p_1	p_1	H	α
^oF	^oK	psi	N/cm^2	psi^{-1}	%
1800	1255.6	137.0	94.5	1.294	3.29
1850	1283.3	155.0	106.9	1.410	4.05
1900	1311.1	177.0	122.0	1.512	4.90
1950	1338.9	201.0	138.6	1.629	5.93
2000	1366.7	224.0	154.4	1.831	7.34
				$\times 10^{-5}$	

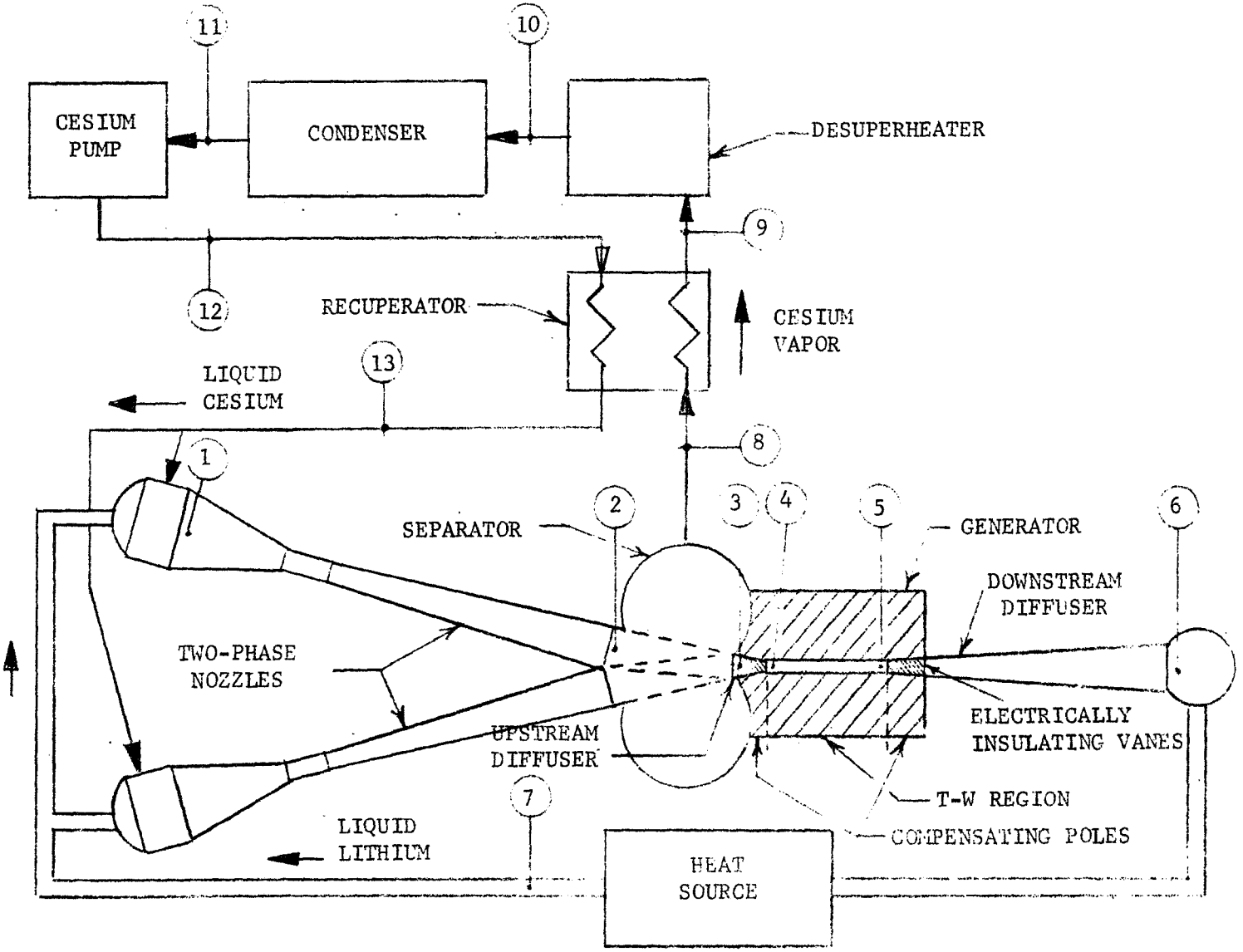

Fig. 1. Cesium-lithium MHD power system with an impinging-jet separator

References

1. Elliott, D. G., and Weinberg, E., "Acceleration of Liquids in Two-Phase Nozzles," Technical Report 32-987, Jet Propulsion Laboratory, Pasadena, Calif., July 1, 1968.

2. Reneau, L. R., Johnston, J. P., and Kline, S. J., "Performance and Design of Straight, Two Dimensional Diffusers," Report PD-8, Department of Mechanical Engineering, Stanford University, Stanford, Calif., September 1964.

3. Eckert, E. R. G., and Drake, R. M., Heat and Mass Transfer, p. 147, McGraw-Hill, N. Y., 1959.

4. Sutton, G. W., Hurwitz, H., Jr., and Poritsky, H., "Electrical and Pressure Losses in a Magnetohydrodynamic Channel Due to End Current Loops," AIEE Transactions, 58, pp. 687-695, January 1962.

5. Elliott, D. G., Cerini, D. J., and Weinberg, E., "Liquid-Metal MHD Power Conversion," Space Power Systems Engineering, Academic Press, N. Y., 1966, pp. 1275-1297.

6. Achener, P. Y., Mackewicz, W. V., Fisher, D. L., and Camp, D. C., "Thermophysical and Heat Transfer Properties of Alkali Metals," Report No. AGN-8195, Vol. I, Aerojet-General Corp., San Ramon, Calif., April 1968.

7. Mechtly, E. A., "The International System of Units; Physical Constants and Conversion Factors," NASA SP-7012, 1964.

8. Tepper, F., Udavcak, R., and Zelenak, J., "Determination of the Solubility of Potassium and Cesium in Lithium," Report MSAR 64-19, MSA Research Corp., Cullery, Pa., April 16, 1964.

Appendix IIA

Reconstruction of Nozzle Inlet and Exit Conditions from p, T, $\bar{V}$, A, and $\bar{A}$

For the cycle analysis the following quantities must be known at the nozzle inlet and exit:

A = flow area

$\bar{A}$ = flow area after velocity and temperature equalization

$\dot{m}_g$ = gas flow rate

$\dot{m}_\ell$ = liquid flow rate

p = pressure

r_v = ratio of gas volume flow rate to liquid volume flow rate

$\bar{T}$ = temperature after equalization

$\bar{V}$ = velocity after equalization

α = mass fraction of cesium dissolved in the liquid phase

β = mass fraction of lithium vapor in the gas phase

ρ_g = density of the gas

ρ_ℓ = density of the liquid

All of these are printed out by the nozzle program, but to save copying only p, $\bar{V}$, A, $\bar{A}$, and $\bar{T}$ are supplied to the cycle program while the rest are recalculated within the program. The temperature-dependent quantities α, β, ρ_g, and ρ_ℓ are evaluated at the equalized temperature $\bar{T}$ and will agree with the barred quantities in the nozzle output; $\bar{T}$ is the proper temperature to use since the gas and liquid temperatures approach equality rapidly downstream of the nozzles and α, β, ρ_g, and ρ_ℓ are only needed after that.

The partial pressure of the cesium vapor is given by Eq. (42) of Ref. 1.

$$p_{Cs} = \frac{p - p_{Li_0}}{1 - H\, p_{Li_0}} \tag{A-1}$$

where

p_{Cs} = cesium partial pressure

p_{Li_0} = vapor pressure of lithium at $\bar{T}$

H = inverse Henry's Law constant

= moles Cs dissolved per unit of Cs partial pressure

The lithium partial pressure is given by Eq. (40) of Ref. 1.

$$p_{Li} = (1 - H\, p_{Cs})\, p_{Li_0} \tag{A-2}$$

The effective molecular weight of the gas phase is given by Eq. (46) of Ref. 1.

$$W_g = \frac{W_{Cs_g}\, p_{Cs} + W_{Li_g}\, p_{Li}}{p} \tag{A-3}$$

where

W_g = effective molecular weight of the gas phase

W_{Cs_g} = effective molecular weight of the cesium vapor (Appendix G)

W_{Li_g} = effective molecular weight of the lithium vapor (Appendix G)

The fraction of cesium dissolved in the liquid phase is given by Eq. (39) of Ref. 1.

$$\alpha = \frac{\left(W_{Cs_\ell}/W_{Li_\ell}\right) H\, p_{Cs}}{1 + \left(W_{Cs_\ell}/W_{Li_\ell} - 1\right) H\, p_{Cs}} \tag{A-4}$$

where

W_{Cs_ℓ} = molecular weight of liquid cesium (atomic weight) = 132.9

W_{Li_ℓ} = molecular weight of liquid lithium (atomic weight) = 6.94

The fraction of lithium vapor in the gas phase is given by Eq. (49) of Ref. 1.

$$\beta = \frac{W_{Li_g} p_{Li}}{W_g p} \tag{A-5}$$

The mixture ratio of liquid to gas, Eq. (51) of Ref. 1, is

$$r = \frac{r_c - (1 + r_c)\ \beta}{1 - (1 + r_c)\ \alpha} \tag{A-6}$$

where

r = ratio of liquid mass flow rate to gas mass flow rate

r_c = ratio of lithium mass flow rate to cesium mass flow rate

The mass flow rates of gas and liquid, from the definition of r, are, respectively

$$\dot{m}_g = \frac{\dot{m}_t}{1 + r} \tag{A-7}$$

and

$$\dot{m}_\ell = r\ \dot{m}_g \tag{A-8}$$

where

$\dot{m}_t$ = total mass flow rate

The density of the liquid, based on additive-volume mixing, is given by Eq. (54) of Ref. 1.

$$\rho_\ell = \frac{1}{\alpha/\rho_{Cs_\ell} + (1 - \alpha)/\rho_{Li_\ell}} \tag{A-9}$$

where

ρ_{Cs_ℓ} = density of liquid cesium (Appendix G)

ρ_{Li_ℓ} = density of liquid lithium (Appendix G)

The density of the gas is given by the perfect gas law, Eq. (13) of Ref. 1, using the effective molecular weight which contains the real-gas effects.

$$\rho_g = \frac{W_g\, p}{R\, \bar{T}} \tag{A-10}$$

where

R = universal gas constant

= 8314 J kg-mole$^{-1}{}^{o}$K^{-1}

The volume flow ratio of gas to liquid is

$$r_v = \frac{\dot{m}_g\, \rho_\ell}{\dot{m}_\ell\, \rho_g} \tag{A-11}$$

The flow area with no slip between the phases is given by Eq. (133) of Ref. 1.

$$A_{\substack{no \\ slip}} = \frac{\dot{m}_g}{\bar{V}} \left(\frac{1}{\rho_g} + \frac{r}{\rho_\ell} \right) \tag{A-12}$$

Appendix IIB

Velocity Equalization Downstream of a Two-Phase Nozzle

At the exit of a two-phase nozzle the velocity of the gas is typically 40% higher than the velocity of the liquid (see Fig. 13 of Ref. 1). As the jet proceeds downstream at constant pressure the gas and liquid velocities approach equality at $\bar{V}$, and the liquid can gain 4% in velocity at the typical Li/Cs mixture ratio of 10. The actual gain is less because of two effects: (1) only a finite distance is available before impingement in the separator and (2) as the gas decelerates it spreads radially beyond the liquid jet and approaches an area $\bar{A}$ while only the central part with area A (typically 70% of $\bar{A}$) remains available to accelerate the liquid.

The following analysis provides an estimate of the liquid velocity deficiency below $\bar{V}$ as a function of distance beyond the nozzle exit.

A. Deficiency Due to Finite Distance

The rate of increase of velocity of the liquid drops with distance, dV_ℓ/dx, can be found by equating the drag force on the drops, due to the higher gas velocity, to the mass times the acceleration of the drops. Thus,

$$\begin{pmatrix}\text{dynamic pressure of}\\ \text{relative gas flow}\end{pmatrix} \times \begin{pmatrix}\text{drag}\\ \text{coefficient}\end{pmatrix} \times \begin{pmatrix}\text{frontal area}\\ \text{of drop}\end{pmatrix}$$
$$= \begin{pmatrix}\text{mass of}\\ \text{drop}\end{pmatrix} \times \begin{pmatrix}\text{acceleration of}\\ \text{drop}\end{pmatrix}$$

or

$$\frac{1}{2}\rho_g (V_g - V_\ell)^2 C_D \frac{\pi D^2}{4} = \rho_\ell \frac{\pi D^3}{6}\left(V_\ell \frac{d V_\ell}{dx}\right) \qquad \text{(B-1)}$$

where

C_D = drag coefficient

D = drop diameter

V_g = gas velocity

V_ℓ = liquid drop velocity

t = time

x = distance from nozzle exit

ρ_g = gas density

ρ_ℓ = liquid density

The equalized velocity which the liquid would reach at infinite distance if all the gas remained mixed with the liquid is the mass-weighted mean velocity $\bar{V}$. This velocity is given by Eq. (6) of Ref. 1.

$$\bar{V} = \frac{V_g + r\, V_\ell}{1 + r} \tag{B-2}$$

where

$\bar{V}$ = velocity after equalization

r = ratio of liquid mass flow rate to gas mass flowrate

Solving Eq. (B-2) for V_g and substituting for V_g in (B-1), the relation between distance and liquid velocity is

$$dx = - \frac{4\, \bar{V}\, \rho_\ell\, D}{3 \rho_g\, C_D\, (1 + r)^2} \frac{d\,(\bar{V} - V_\ell)}{(\bar{V} - V_\ell)^2} \tag{B-3}$$

where V_ℓ has been approximated by $\bar{V}$ in the factor $4\, \bar{V}\, \rho_\ell\, D$.

The Reynolds number for the gas flow past the drops is typically above 500 where C_D is nearly constant at about 0.5 (see Fig. 2, Ref. 1.). With only V_ℓ varying, Eq. (B-3) can be integrated from $V_\ell = V_{\ell_1}$ at $x = 0$ to $V_\ell = V_{\ell_2}$ at $x = L$ to give the velocity deficiency at L. The result is

$$\bar{V} - V_{\ell_2} = \frac{\bar{V}}{\dfrac{\bar{V}}{\bar{V} - V_{\ell_1}} + 0.375 \dfrac{\rho_g\, L\, (1 + r)^2}{\rho_\ell\, D}}$$

$$= \frac{\bar{V}}{K_d} \tag{B-4}$$

where

V_{ℓ_1} = liquid velocity at nozzle exit

V_{ℓ_2} = liquid velocity at distance L downstream

K_d = "distance factor" defined by Eq. (B-4)

Solving Eq. (B-4) for the downstream liquid velocity the result is

$$V_{\ell_2} = \bar{V} \left(1 - 1/K_d\right) \tag{B-5}$$

The initial liquid velocity V_{ℓ_1} can be estimated with sufficient accuracy from $\bar{V}$, A, and $\bar{A}$. Since the flow area is mostly gas, the continuity equation for the gas before and after equalization is $V_{g_1} A = \bar{V} \bar{A}$, or

$$V_{g_1} = \bar{V} \bar{A}/A \tag{B-6}$$

Substituting this value of V_g into Eq. (B-2), the initial liquid velocity is

$$V_{\ell_1} = \bar{V} \left(1 - \frac{\bar{A}/A - 1}{r}\right) \tag{B-7}$$

Using this value of V_{ℓ_1} in Eq. (B-4), the "distance factor" K_d is

$$K_d = \frac{r}{\bar{A}/A - 1} + 0.375 \frac{\rho_g L (1 + r)^2}{\rho_\ell D} \tag{B-8}$$

B. Deficiency Due to Gas Flow Loss

At infinite distance downstream the final liquid velocity is $\bar{V}$ (without the flow loss effect), and the gas flow occupies area $\bar{A}$ while the liquid flow still occupies area A, neglecting divergence of the liquid jet. The final flow rate of gas mixed with the liquid is, therefore, only $\dot{m}_g A/\bar{A}$, and the mean flow of gas available to accelerate the liquid is

$$\dot{m}_{g_m} = \dot{m}_g \frac{1 + A/\bar{A}}{2} \tag{B-9}$$

The velocity increase of the liquid is reduced in proportion to the reduction in gas flow. Thus,

$$\frac{V_{\ell_2} - V_{\ell_1}}{\bar{V} - V_{\ell_1}} = \frac{\dot{m}_{g_m}}{\dot{m}_g} \tag{B-10}$$

Substituting the mean gas flow from Eq. (B-9) and the initial liquid velocity from Eq. (B-7), the velocity deficiency at infinite distance due to the flow loss is

$$\bar{V} - V_{\ell_2} = \frac{\bar{V}\ (1 - A/\bar{A})^2}{2r\ A/\bar{A}}$$

$$= \bar{V}\ K_f \tag{B-11}$$

where

K_f = "flow loss factor" defined by Eq. (B-11)

From Eqs. (B-5) and (B-11), the liquid velocity including both the distance effect and the flow loss effect is

$$V_{\ell_2} = \bar{V}\ (1 - 1/K_d)(1 - K_f) \tag{B-12}$$

Typical exit conditions for a cesium-lithium nozzle are: mixture ratio $r = 14.5$, area ratio $A/\bar{A} = 0.69$, gas density $\rho_g = 0.88$ kg/m^3, liquid density $\rho_\ell = 437$ kg/m^3, drop diameter $D = 0.057$ cm, and mean exit velocity $\bar{V} = 138.8$ m/s. Equations (B-6) and (B-7) give $V_{g_1} = 202$ m/s and $V_{\ell_1} = 134.5$ m/s, respectively, in sufficient agreement with the true values 199 m/s and 134.7 m/s from the nozzle program. The value of K_f from Eq. (B-11) is 0.0048 showing that the limiting liquid velocity is 0.48% less than $\bar{V}$.

Figure B-1 presents the variation of liquid velocity with distance calculated from Eq. (B-12). The velocity increases rapidly for the first 20 cm then approaches the limiting value slowly. In a 300 kWe system the distance to the intersection of the center lines of the two impinging nozzles would be about 15 cm. The liquid velocity at that distance is 136.4 m/s, which is 1.7% less than $\bar{V}$ and 40% of the way from V_{ℓ_1} to $\bar{V}$.

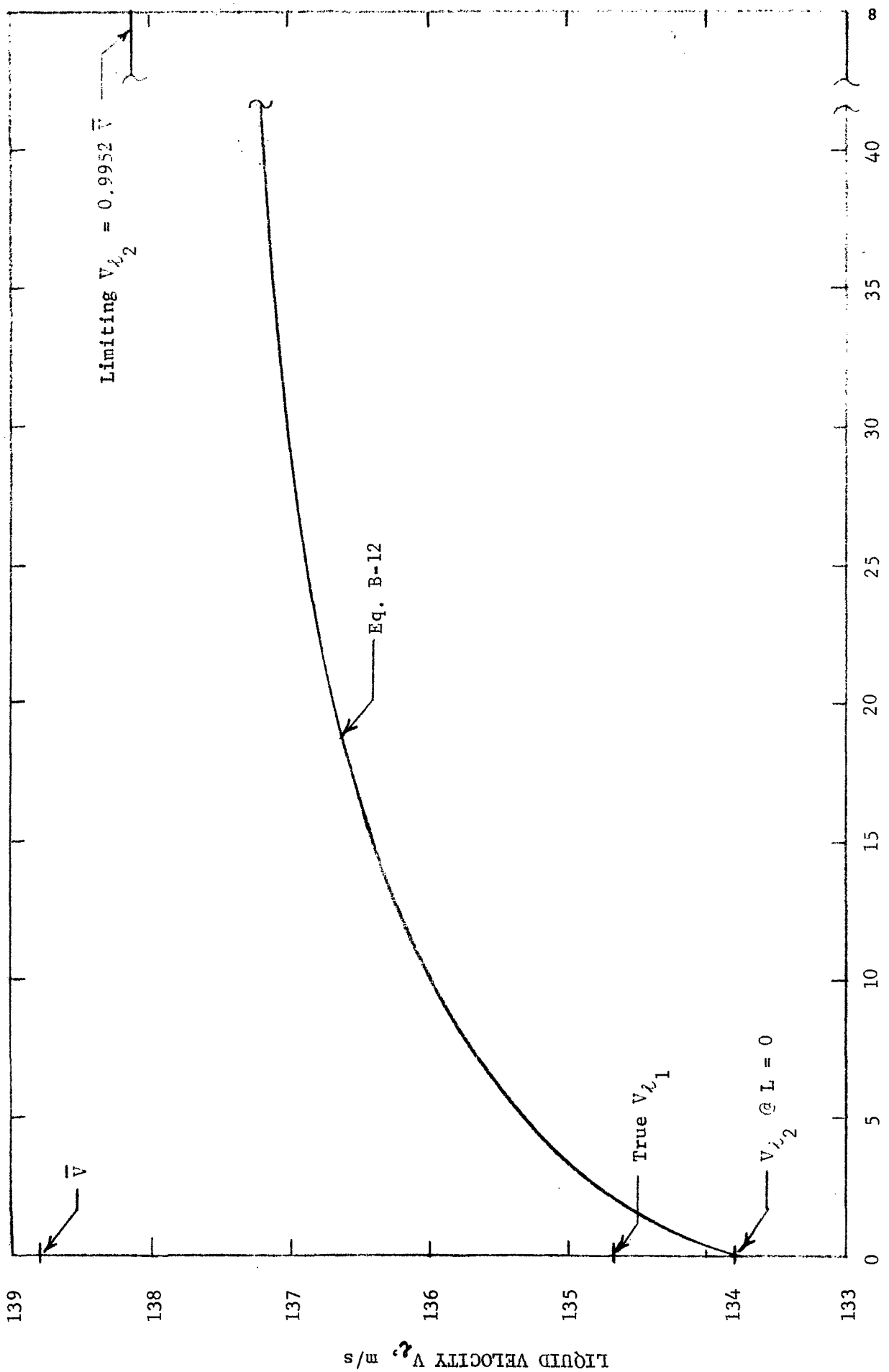

Fig. B-1. Acceleration of lithium downstream of a cesium-lithium nozzle

Appendix IIC

Isentropic Dissolving Diffuser Flow

A two-phase mixture of cesium and lithium enters a diffuser at pressure p_1 and velocity V_1. In the diffuser the pressure increases to p_2, causing the cesium to dissolve in the lithium, and an all-liquid stream leaves the diffuser at a reduced velocity V_2. The problem is, first, to find the pressure p_2 at which dissolving is complete and then to find the corresponding velocity V_2, for flow without friction (isentropic flow).

A. Exit Pressure

The mass of cesium dissolved in the liquid at the diffuser inlet is

$$\dot{m}_{d_1} = \alpha \dot{m}_{\ell_1} \tag{C-1}$$

where

$\dot{m}_{\ell_1}$ = inlet liquid flow rate

α = mass fraction of cesium dissolved in the liquid at the inlet

At a point in the diffuser where the pressure has increased to p and the gas flow rate has decreased to $\dot{m}_g$ the dissolved cesium flow is

$$\dot{m}_d = \dot{m}_{d_1} + \dot{m}_{g_1} - \dot{m}_g \tag{C-2}$$

where

$\dot{m}_{g_1}$ = inlet gas flow rate

Ignoring the lithium partial pressure for simplicity, the pressure ratio for dissolving the additional cesium is

$$\frac{p}{p_1} = \frac{\dot{m}_d}{\dot{m}_{d_1}} \tag{C-3}$$

Substituting Eqs. (C-1) and (C-2) into Eq. (C-3), the pressure ratio is

$$\frac{p}{p_1} = 1 + \frac{\dot{m}_{g_1}}{\alpha \dot{m}_{\ell_1}} \left(1 - \frac{\dot{m}_g}{\dot{m}_{g_1}}\right) \tag{C-4}$$

By definition of the volume ratio r_v, the inlet gas flow rate is

$$\dot{m}_{g_1} = \frac{\dot{m}_{\ell_1} r_{v_1} \rho_{g_1}}{\rho_\ell} \tag{C-5}$$

where

r_{v_1} = inlet gas/liquid volume ratio

ρ_{g_1} = inlet gas density

ρ_ℓ = liquid density

The gas flow rate at pressure p is

$$\dot{m}_g = \frac{\dot{m}_\ell r_v \rho_g}{\rho_\ell}$$

$$= \frac{\dot{m}_\ell r_v \rho_{g_1} p}{\rho_\ell p_1} \tag{C-6}$$

ignoring the small temperature change.

Substituting Eqs. (C-5) and (C-6) into Eq. (C-4) and ignoring the small change in liquid flow rate, the pressure ratio is

$$\frac{p}{p_1} = 1 + \frac{\dot{m}_{g_1}}{\alpha \dot{m}_{\ell_1}} \left(1 - \frac{r_v p}{r_{v_1} p_1} \right) \tag{C-7}$$

At the exit $r_v = 0$. Therefore, the exit pressure is given by

$$\frac{p_2}{p_1} = 1 + \frac{\dot{m}_{g_1}}{\alpha \dot{m}_{\ell_1}} \tag{C-8}$$

B. Exit Velocity

The retarding force on a fluid element in the diffuser with pressure p upstream and pressure p + dp downstream is A dp. This retarding force reduces the momentum such that

$$\dot{m}_{\ell_2} \, dV = - A \, dp \tag{C-9}$$

where

A = local flow area

$\dot{m}_{\ell_2}$ = exit liquid flow rate

= total flow rate

V = local velocity

The flow area is related to the local volume ratio by

$$A = \frac{\dot{m}_\ell \, (1 + r_v)}{\rho_\ell \, V} \tag{C-10}$$

Substituting this value of A into Eq. (C-9), noting that $V \, dV = dV^2/2$, and neglecting the change in liquid flow, the momentum equation, Eq. (C-9), becomes

$$dV^2 = - \frac{2 \, (1 + r_v)}{\rho_\ell} \, dp \tag{C-11}$$

Substituting Eq. (C-8) into Eq. (C-7), the volume ratio as a function of pressure is

$$r_v = r_{v_1}\left(\frac{p_1}{p}\right)\left(\frac{1 - p/p_2}{1 - p_1/p_2}\right) \tag{C-12}$$

Substituting this expression for r_v into the momentum equation, Eq. (C-11), and integrating between p_1 and p_2, the exit velocity is

$$V_2 = \left\{V_1^2 - \frac{2p_2}{\rho_\ell}\left[1 - \left(1 + r_{v_1}\right)\left(p_1/p_2\right) - \frac{r_{v_1}(p_1/p_2)\log_e(p_1/p_2)}{1 - p_1/p_2}\right]\right\}^{\frac{1}{2}} \tag{C-13}$$

Appendix IID

Liquid Diffuser Flow

The downstream diffuser is a simple diverging diffuser with liquid flow. Two added losses are the vane friction and electrical force, but these are calculated separately using the relations of Appendix E and Appendix F. For the diffuser channel without the vanes and electrical effects, Ref. 2, Fig. 2.01, shows that an efficiency of 0.85 is attained experimentally when (1) the inlet boundary layer is thin, which should be the case with the velocity profile flattening caused by the generator, (2) the divergence half-angle is 3-5 deg, and (3) the area ratio is 4.0 or larger. The efficiency is defined as

$$\eta_d = \frac{p_2 - p_1}{\rho_\ell V_1^2/2} \tag{D-1}$$

where

η_d = diffuser efficiency (= pressure recovery C_p in Ref. 2)

p_1 = inlet pressure

p_2 = exit pressure

V_1 = inlet velocity

ρ_ℓ = liquid density

Thus, the required diffuser inlet velocity for given p_1 and p_2, without vane friction losses or electrical losses, is

$$V_1 = \left(2 \frac{p_2 - p_1}{0.85\ \rho_\ell} \right)^{\frac{1}{2}} \tag{D-2}$$

Appendix IIE

Vane-channel Friction Loss

Figure E-1 shows the flow geometry. The inlet height is

$$h_1 = \frac{\dot{m}_\ell \left(1 + r_{v_1} \right)}{V_1 \, \rho_\ell \, c} \tag{E-1}$$

where

$\dot{m}_\ell$ = the liquid flow rate, assumed constant at the generator flow value $\dot{m}_{\ell_4}$ in both diffusers

r_{v_1} = inlet volume ratio

V_1 = inlet velocity

ρ_ℓ = liquid density

c = diffuser width

The exit height, since r_{v_2} is zero in both diffusers, is

$$h_2 = \frac{\dot{m}_\ell}{V_2 \, \rho_\ell \, c} \tag{E-2}$$

where

V_2 = exit velocity

For simplicity, the friction loss will be calculated for constant-velocity flow at the mean conditions. The mean height is

$$h = \frac{h_1 + h_2}{2} \tag{E-3}$$

The mean velocity is

$$V = \frac{V_1 + V_2}{2} \tag{E-4}$$

The inlet density is

$$\rho_1 = \frac{\rho_\ell}{1 + r_{v_1}} \tag{E-5}$$

The exit density is ρ_ℓ, and the mean density is $(\rho_1 + \rho_2)/2$ or

$$\rho = \frac{\rho_\ell \left[1 + r_{v_1}/2 \right]}{1 + r_{v_1}} \tag{E-6}$$

The area over which the friction force is exerted is the sum of the wall area and the vane area.

$$A = 2\,L\,c + 2\,L\,N\,h \tag{E-7}$$

where

L = vane length

N = number of vane channels

For the downstream diffuser the wall area is omitted, because the diffuser efficiency (Appendix D) already includes the wall friction.

The vanes in both diffusers, and the walls in the upstream diffuser, have no initial boundary layer, and the vane-channel lengths are typically too short for the boundary layers from opposite sides to meet. Therefore, the drag is calculated from flat plate relations. The Reynolds number based on vane length is

$$Re_x = \frac{V\,\rho\,L}{\mu} \tag{E-8}$$

where

μ = liquid viscosity

A simple relation for the mean friction factor is given in Ref. 3.

$$f_{pm} = \frac{0.455}{(\log_{10} Re_x)^{2.58}} \tag{E-9}$$

The friction force is the product of dynamic pressure $\rho V^2/2$, friction factor, and area. Adding 30% to be conservative, the friction force is

$$F = 0.65 \rho V^2 f_{pm} A \tag{E-10}$$

In the upstream diffuser this force produces a decrease in exit velocity, and in the downstream diffuser it produces an increase in required inlet velocity, equal to

$$\Delta V_f = \frac{F}{\dot{m}_\ell} \tag{E-11}$$

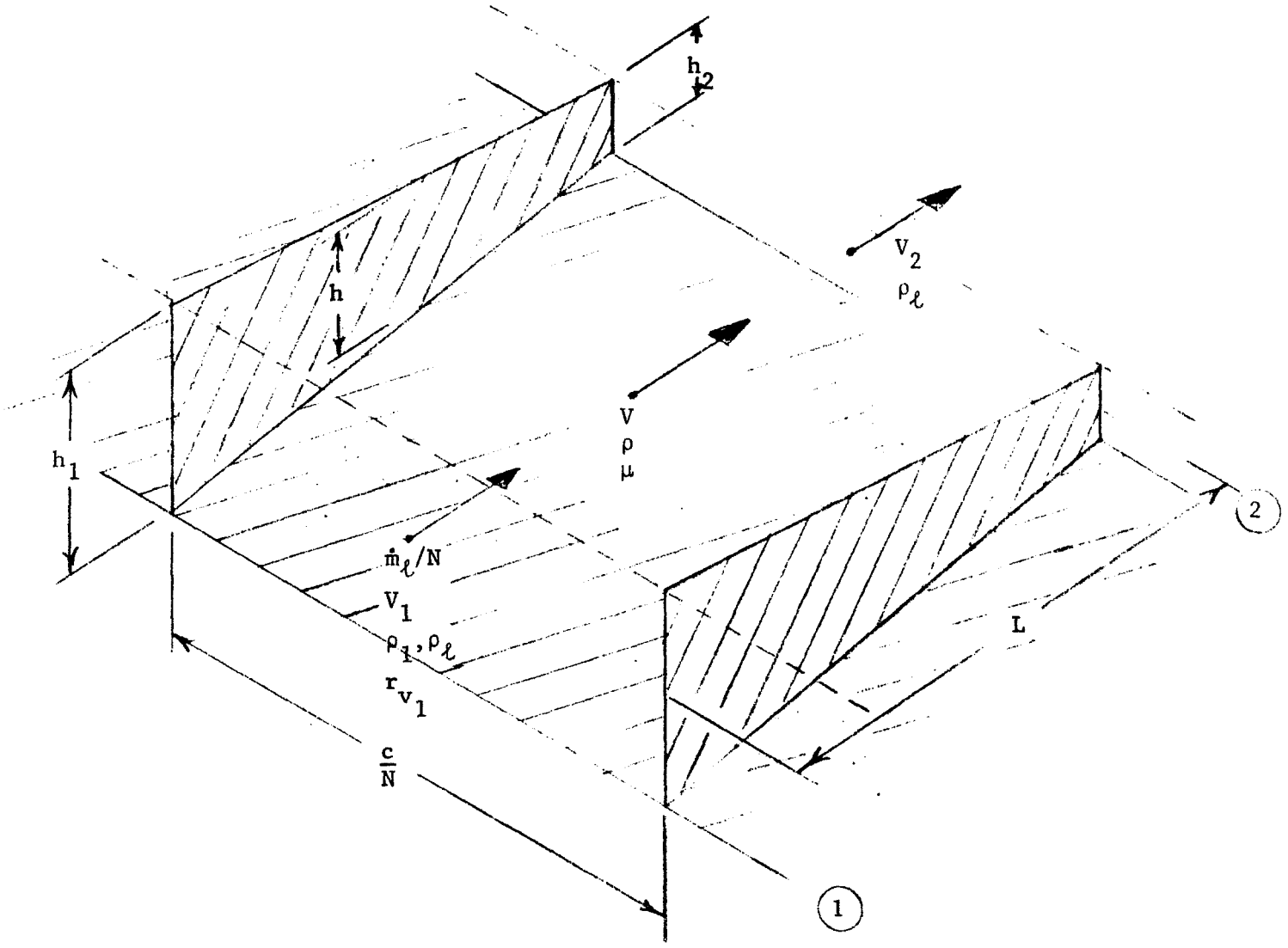

Fig. E-1. Friction loss in a vane channel

Appendix IIF

Vane Channel Electrical Losses

The two kinds of electrical losses from the compensating flux are illustrated in Fig. F-1: (1) the motion of the fluid through the magnetic field generates a voltage across each vane channel causing shunt end currents, and (2) the rate of change of the field generates eddy-current loops in each channel.

The power losses can be calculated separately and added even though the currents may overlap, because the currents from the two effects are 90 deg apart in phase. If I_1 is the rms current through an arbitrary fluid element due to the first effect and I_2 is the rms current due to the second effect, then the rms total current through the element is

$$I = \left(I_1^2 + I_2^2\right)^{\frac{1}{2}} \tag{F-1}$$

If the resistance of the element is R the power dissipated in it is $P = I^2R$, and from Eq. F-1

$$P = I_1^2 R + I_2^2 R$$

$$= P_1 + P_2 \tag{F-2}$$

where

P = total loss in the fluid element

P_1 = loss due to motion-induced current (effect 1)

P_2 = loss due to eddy current (effect 2)

Since Eq. (F-2) holds at each point, the total power loss in the fluid can be found by calculating the loss due to each effect separately and adding.

A. Mean Flow Conditions

For simplicity, the electrical losses will be calculated for constant-velocity flow at the mean conditions. The mean height h and mean velocity V are the same as used in Appendix E. A mean electrical conductivity is required. The conductivity of liquid lithium is 2×10^6 mho/m, and this will be the conductivity at the exit of the upstream vane channels and throughout the downstream vane channels. At the inlet of the upstream vane channels the conductivity can be estimated from the volume ratio r_{v_1} using the data plotted in Fig. 9 of Ref. 5. The conductivity is equal to or less than

$$\sigma_1 = \frac{2 \times 10^6}{\left(1 + r_{v_1}\right)^{1.6}} \tag{F-3}$$

where

σ_1 = inlet conductivity

r_{v_1} = inlet gas/liquid volume ratio

The mean conductivity is

$$\sigma = \frac{\sigma_1 + \sigma_2}{2} \tag{F-4}$$

where

σ_2 = exit conductivity

= 2×10^6 mho/m

Although σ_1 may be several times less than σ_2, Eq. (F-4) properly averages the two values for calculating total power loss, at least for the shunt end currents. With the same voltage E applied across the end resistances at each end,

the loss calculated by treating each end separately would be const x ($E^2 \sigma_1$ + $E^2 \sigma_2$), which is the same as const x(2 $E^2 \sigma$).

Substituting Eq. (F-3) into Eq. (F-4), the mean conductivity is

$$\sigma = 10^6 \left[1 + \frac{1}{\left(1 + r_{v_1}\right)^{1.6}} \right] \tag{F-5}$$

B. Shunt End Loss

The shunt end loss can be calculated from the theory of Ref. 4. The theory requires a value of the e-folding length of the magnetic field. Referring to Fig. F-1, the rms field is constant at a value B_0 over a central portion of the channel of length L_0 and drops off to 1/e of that value at the ends of the channel. The distance over which the decrease occurs is the e-folding length. The central, constant-field, length is

$$L_0 = L - 2\ Y_e \tag{F-6}$$

where

L_0 = length of constant field

L = length of vanes

Y_e = distance over which the field decreases to B_0/e

The e-folding length of a magnet is roughly equal to the gap, h in this case, ignoring the thermal insulation thickness. If h/L is large enough to make L_0 less than L/5, then Y_e is assumed to be sufficiently smaller than h to make L_0 = L/5. Thus,

$$\begin{aligned} Y_e &= h \quad \text{if} \quad L - 2h > L/5 \\ &= 2L/5 \quad \text{if} \quad L - 2h < L/5 \end{aligned} \tag{F-7}$$

where

h = mean channel height from Eq. (E-3) (h = 1 in Ref. 4)

The rms magnetic flux produced by the field is

$$\phi = c\ L_0\ B_0 + 2c \int_0^{\infty} B_0\ e^{-x/Y_e}\ dx$$

$$= c\ B_0\ (L_0 + 2\ Y_e) \qquad \text{(F-8)}$$

Using L_0 from Eq. (F-6), the rms center field required is

$$B_0 = \frac{\phi_c}{c\ L_i} \qquad \text{(F-9)}$$

where

ϕ_c = the required rms compensating flux

Quantities required in the theory of Ref. 4 are

$$c_1 = \frac{c}{N} \qquad \text{(F-10)}$$

$$y_e = \frac{2\pi\ Y_e}{c_1} \qquad \text{(F-11)}$$

$$\gamma = \frac{2}{y_e} \qquad \text{(F-12)}$$

where

c_1 = width of an individual vane channel (= h in Ref. 4)

y_e = dimensionless e-folding length of the field extension

γ = exponential coefficient of the field extension

The quantities y_e and γ are used for calculating the two coefficients β_1 and β_3 employed in the theory for determining the effect of the e-folding length on the shunt end currents.

The parameter β_1 is given as a function of γ by Eq. (20) of Ref. 4. To provide a simpler formula for faster computation, a polynomial was fitted to the inverse of β_1 over the range of γ values of interest, $0 < \gamma < 10$. The formula is

$$\beta_1 = 1/(1.45125 + 1.31968\ \gamma - 0.02505\ \gamma^2 + 0.00119\ \gamma^3) \qquad \text{(F-13)}$$

The parameter β_3 is the function of y_e inside the bracket of Eq. (91) of Ref. 4, with a minus sign (β_3 here equals - β_3 in Ref. 4). A polynomial was fitted to β_3 over the range of y_e values of interest, $0 < y_e < 20$. The formula is

$$\beta_3 = 0.0044 + 0.12828\ y_e - 0.022195\ y_e^2 + 0.0020146\ y_e^3 - 0.8824 \times 10^{-4}\ y_e^4 + 0.1473 \times 10^{-5}\ y_e^5 \qquad \text{(F-14)}$$

Each vane channel acts as an open-circuit generator, with zero power output. The loading, or voltage coefficient, for this condition is given by Eq. (22) of Ref. 4. Using the present notation,

$$K_0 = \frac{1 + \dfrac{2c_1\ \beta_1}{\pi\ L_0}}{1 + \dfrac{2c_1\ \log_e 2}{\pi\ L_0}} \qquad \text{(F-15)}$$

K_0 is the ratio between the actual voltage across the vane channel and the voltage $c_1\ B_0\ V$ that would exist without end currents (K_0 is denoted η in Ref. 4.).

The pressure change from upstream of the channel to downstream of the channel due to the shunt currents is given by Eq. (91) of Ref. 4. Using present notation,

$$\Delta p_a = \frac{\Delta P^+}{Vc_1} - \sigma\ V\ c_1\ B_0^2\ \beta_3 + \Delta\ p_i \qquad \text{(F-16)}$$

where

Δp_a = difference between the pressure downstream of the channel and the pressure upstream of the channel

ΔP^+ = power generated due to field extension

Δp_i = ideal pressure change (no end effects)

The value of ΔP^+ is given by Eq. (71) of Ref. 4. Correcting the misprinted $\pi^{-\frac{1}{2}}$ to π^{-1}, the relation is

$$\Delta P^+ = 2 \sigma K_0 V^2 B_0^2 c_1^2 \beta_1/\pi \tag{F-17}$$

The value of Δp_i is given by Eq. (81) of Ref. 4 (in which σ is missing on the right side).

$$\Delta p_i = \sigma (K_0 - 1) V B_0^2 L_0 \tag{F-18}$$

For the constant velocity case treated in Ref. 4 the fluid input power is equal to the volume flow rate times the pressure drop. For all N vane channels the power input, which is equal to the power dissipated in the shunt end currents, is

$$\begin{aligned} P_s &= - N c_1 h V \Delta p_a \\ &= - c h V \Delta p_a \end{aligned} \tag{F-19}$$

Equation (F-19) merely expresses the fact that there is a retarding force on the fluid due to the shunt currents such that

$$F_e = \frac{P_s}{V} \tag{F-20}$$

In the present case the force changes the velocity instead of the pressure, and the velocity change is

$$\Delta V_e = \frac{P_s}{\dot{m}_\ell V} \tag{F-21}$$

where

$\dot{m}_\ell$ = the flow rate through the diffuser

Substituting Eqs. (F-16), (F-17), and (F-18) into Eq. (F-19), the fluid power input due to the shunt end currents is

$$P_s = \sigma\, c\, h\, L_0\, B_0^2\, V^2 \left[1 - K_0 + \frac{c_1}{L_0}\left(\beta_3 - \frac{2\, K_0\, \beta_1}{\pi}\right)\right] \tag{F-22}$$

C. Eddy Current Loss

Figure F-2 shows the fluid in one of the vane channels as viewed in the field direction. For calculating the eddy-current loss the fluid in a vane channel will be treated as a slab of length L, width c_1, thickness h, and conductivity σ, with a uniform magnetic field of rms value B_0 penetrating it and oscillating at frequency f.

The eddy current paths can be approximated by rectangular loops, one of which is shown in Fig. F-2. The resistance of each of the longitudinal legs is

$$R_L = \frac{2x}{\sigma\, h\, dx\, (c_1/L)} \tag{F-23}$$

where

x = distance from the center of the channel to the loop in the L direction

dx = width of the loop in the L direction

The resistance of each of the lateral legs is

$$R_c = \frac{2\, x\, c_1/L}{\sigma\, h\, dx} \tag{F-24}$$

The total resistance around the loop is

$$R = 2\,(R_c + R_L)$$

$$= \frac{4x}{\sigma\, h\, dx}\left(\frac{c_1}{L} + \frac{L}{c_1}\right) \tag{F-25}$$

The area inside the loop is $4\,x^2\,c_1/L$, and the time rate of change of flux through this area is equal to the resistance times the current in the loop.

$$R\,dI = 2\,\pi\,f\,B_0\left[4\,x^2\,c_1/L\right] \tag{F-26}$$

where

f = frequency of the field

Substituting R from Eq. (F-25), the current in the loop is

$$dI = \frac{2\,\pi\,f\,\sigma\,c_1\,h\,B_0\,x\,dx}{L\,(c_1/L + L/c_1)} \tag{F-27}$$

The power dissipated in the loop is

$$d\,P_{ec} = R\,(dI)^2$$

$$= \frac{16\,\pi^2\,f^2\,\sigma\,c_1{}^2\,h\,B_0{}^2\,x^3\,dx}{L^2\,(c_1/L + L/c_1)} \tag{F-28}$$

The power dissipated in the vane channel is the integral of dP_{ec} from $x = 0$ to $x = L/2$. Multiplying by N, the eddy current loss in the diffuser is

$$P_{ec} = \frac{\sigma\,N\,h\,(\pi\,f\,B_0\,c_1\,L)^2}{4\,(c_1/L + L/c_1)} \tag{F-29}$$

This power loss does not produce a retarding force on the fluid, since forces on one side of the current loops are canceled by forces on the other. The source of the power is the generator, and P_{ec} must be subtracted from the generator power output.

The eddy currents also affect the generator in requiring an increase in compensating-pole winding current to overcome the reaction field produced by the eddy currents. The field produced by the current loop dI is

$$dB = \frac{\mu_0 \, dI}{g} \tag{F-30}$$

where

g = iron gap

μ_0 = fluid permeability

The flux is dB times the loop area $4 x^2 c_1/L$.

$$d\phi_r = \frac{4 \mu_0 x^2 c_1 \, dI}{g L} \tag{F-31}$$

where

ϕ_r = reaction flux due to the eddy currents

Substituting dI from Eq. (F-27) and integrating over the vane channel, the total reaction flux is

$$\phi_r = \frac{\sigma h \pi f \mu_0 B_0 L^2 c_1^2}{8 g (c_1/L + L/c_1)} \tag{F-32}$$

The number of ampere-turns of winding current required to overcome the reaction flux is given by

$$\phi_r = \frac{\mu_0 N I L c_1}{g} \tag{F-33}$$

Substituting ϕ_r from Eq. (F-32) and solving for N I, the number of ampere-turns that must be added to the generator compensating-pole excitation (180 deg out of phase with the eddy currents) is

$$N I = \frac{\sigma h \pi f B_0 c_1 L}{8 (c_1/L + L/c_1)} \tag{F-34}$$

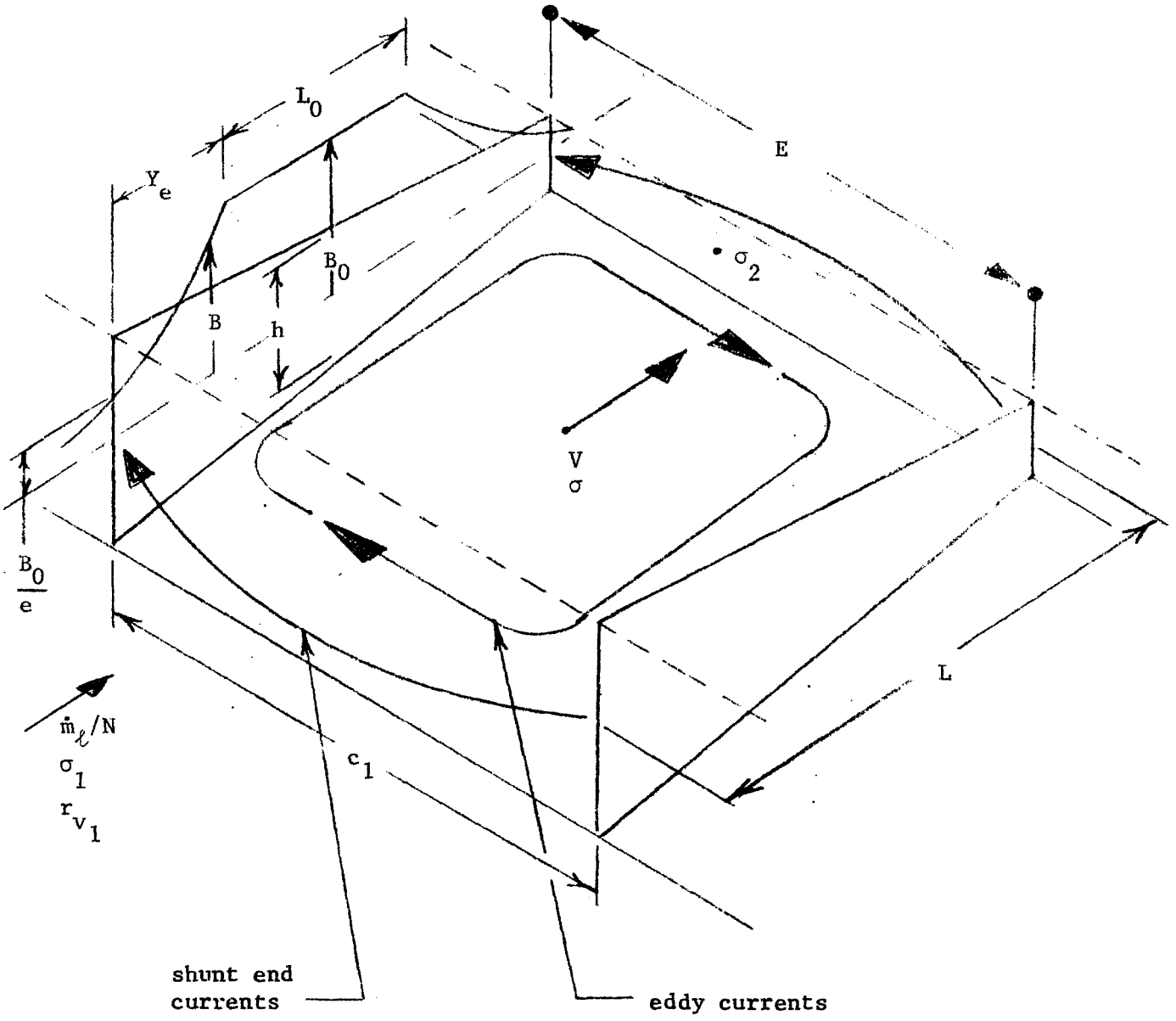

Fig. F-1. Electrical losses in a vane channel

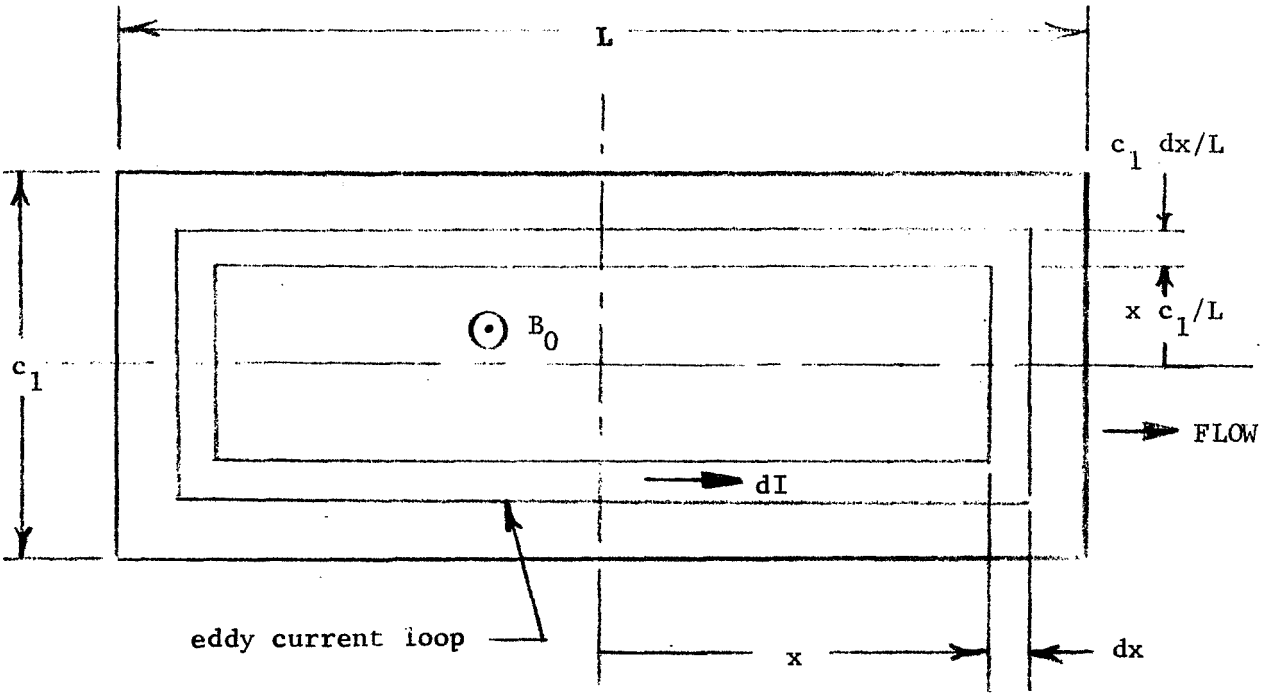

Fig. F-2. Eddy currents in a vane channel

Appendix IIG

Fluid Properties

The cesium and lithium properties are taken from Ref. 6, the most recent compilation of alkali metal properties.

The vapor pressure of lithium is given by Eq. (138) of Ref. 6.

$$\log_{10} p = - 2.1974 - \frac{6499.1}{T} + 1.9390 \log_{10} T \qquad \text{(G-1)}$$

where

p = vapor pressure in atmospheres

T = temperature in ^{o}K

Solving for p and multiplying by the conversion factor from atm to N/m^2 (101325 from Ref. 7, p. 17) the lithium vapor pressure is

$$p_{Li_0} = 101325 \times 10^{\left(- 2.1974 - \frac{6499.1}{T} + 1.9390 \log_{10} T\right)} \qquad \text{(G-2)}$$

The vapor pressure of cesium in atm is given by Eq. (18) of Ref. 6.

$$\log_{10} p = 3.36292 - \frac{3617.76}{T} + 0.16005 \log_{10} T \qquad \text{(G-3)}$$

To calculate the temperature from the pressure, Eq. (G-3) can be rearranged for iterative solution. Dividing p by 101325 to convert to N/m^2, the saturation temperature in ^{o}K is

$$T_s = \frac{3617.76}{3.36292 - \log_{10}\left(\frac{p}{101325}\right) + 0.16 \log_{10} T_s} \qquad \text{(G-4)}$$

The effective cesium molecular weight is the value which, when substituted in the perfect gas equation, gives the actual density of cesium vapor. Thus, the effective molecular weight is defined by

$$\rho_{Cs_g} = \frac{W_{Cs_g} p}{R T} \tag{G-5}$$

where

ρ_{Cs_g} = cesium vapor density

p = pressure

R = universal gas constant

T = temperature

The effective molecular weight can be determined from the equation of state given by Eq. (27) of Ref. 6.

$$p = \frac{RT}{v} Z \tag{G-6}$$

where

v = volume per mole of monomer

and Z is given by

$$Z = 1 - \frac{82.173\ T^{0.15}}{v} + \frac{2.7318 \times 10^{7} \exp(1500/T)}{v^2} - \frac{1.0421 \times 10^{12} \exp(550/T)}{v^3} + \frac{1.2610 \times 10^{16}}{v^4} - \frac{3.6091 \times 10^{19}}{v^5} \tag{G-7}$$

with v in cm^3 $g\text{-}mole^{-1}$ monomer.

The monomer molecular weight is the liquid molecular weight (atomic weight) $W_{Cs_\ell} = 132.9$ used in Appendix A. The specific volume, by definition of v, is v/W_{Cs_ℓ} and the density is the inverse.

$$\rho_{Cs_g} = \frac{W_{Cs_\ell}}{v} \tag{G-8}$$

From Eqs. (G-5) and (G-8) the value of v is

$$v = \frac{W_{Cs_\ell} RT}{W_{Cs_g} p} \tag{G-9}$$

Substituting Eq. (G-9) into Eq. (G-6), the effective molecular weight is

$$W_{Cs_g} = \frac{W_{Cs_\ell}}{Z} \tag{G-10}$$

The procedure for calculating W_{Cs_g} for given pressure and temperature is: (1) guess a value of W_{Cs_g}, say W_{Cs_ℓ}, (2) calculate v from Eq. (G-9), (3) calculate Z from Eq. (G-7) and W_{Cs_g} from Eq. (G-10), (4) continue recalculating v, Z, and W_{Cs_g} until W_{Cs_g} converges to the desired accuracy. Using R = 8.314 in Eq. (G-9) will give v in m^3 g-mole^{-1} $^oK^{-1}$ (Ref. 7, p. 5); to provide v in cm^3 g-mole ^oK for Eq. (G-7), R must be multiplied by 10^6.

The effective molecular weight of lithium vapor is given by Eq. (148) of Ref. 6. In present notation,

$$W_{Li_g} = W_{Li_\ell}\left(2 - \frac{p_1}{p_{Li_0}}\right) \tag{G-11}$$

where

W_{Li_ℓ} = liquid, or monomer, molecular weight (atomic weight)

= 6.94

p_{Li_0} = lithium vapor pressure

p_1 = partial pressure of the monomer

The monomer partial pressure is given by Eq. (146) of Ref. 6.

$$p_1 = \frac{-1 + \left(1 + 4K_2 p_{Li_0}\right)^{1/2}}{2K_2} \qquad \text{(G-12)}$$

where

K_2 = equilibrium constant for formation of the dimer from the monomer

Substituting Eq. (G-12) into Eq. (G-11), the effective molecular weight is

$$W_{Li_g} = W_{Li_\ell}\left[2 - \frac{\left(1 + 4K_2 p_{Li_0}\right)^{1/2} - 1}{2K_2 p_{Li_0}}\right] \qquad \text{(G-13)}$$

where p_{Li_0} is in atm for the K_2 values given in Ref. 6.

Equation (145) of Ref. 6 gives the value of K2 as

$$K_2 = \frac{K_{f,2}}{(K_{f,1})^2} \qquad \text{(G-14)}$$

where

$K_{f,1}$ = equilibrium constant for formation of the monomer from the liquid

$K_{f,2}$ = equilibrium constant for formation of the dimer from the liquid

Values of $\log_{10} K_{f,1}$ and $\log_{10} K_{f,2}$ are given in Tables 74 and 75, respectively, of Ref. 6. In terms of these values Eq. (G-14) is

$$K_2 = 10^Q \tag{G-15}$$

where

$$Q = \log_{10} K_{f,2} - 2 \log_{10} K_{f,1} \tag{G-16}$$

Values of $\log_{10} K_{f,1}$ and $\log_{10} K_{f,2}$ from Ref. 6 and the corresponding values of Q from Eq. (G-16) are tabulated in Table G-1 for the temperature range of interest, 1000 - 1500°K. The values of Q can be fitted within 1% by

$$Q = 10.1245 - 0.01183825\ T + 0.31625 \times 10^{-5}\ T^2 \tag{G-17}$$

The density of liquid cesium in g/cm^3 as a function of temperature, t, in °C is given by Eq. (5) of Ref. 6. Replacing t by T-273 and multiplying by 1000, the density of liquid cesium in kg/m^3 is

$$\rho_{Cs_\ell} = 434 + 24.95\ (2043\text{-}T)^{1/2} + 0.2083\ (2043\text{-}T) \tag{G-18}$$

The density of liquid lithium in g/cm^3 as a function of temperature, t, in °C is given by Eq. (125) of Ref. 6. Replacing t by T-273 and multiplying by 1000, the density of liquid lithium in kg/m^3 is

$$\rho_{Li_\ell} = 124 + 5.306\ (3173\text{-}T)^{1/2} + 0.04135\ (3173\text{-}T) \tag{G-19}$$

The viscosity of liquid lithium in millipoise is given by Eq. (136) of Ref. 6

$$\log_{10} \mu = 5.41921 - \frac{155.991}{T} - 1.61506 \log_{10} T \tag{G-20}$$

Solving for μ and multiplying by 10^{-4} to convert millipoise to $N \cdot s/m^2$ (Ref. 7, p. 18), the viscosity of liquid lithium is

$$\mu = 10^{(1.419 - 156/T - 1.615 \log_{10} T)} \qquad \text{(G-21)}$$

The latent heat, or enthalpy, of vaporization of cesium in cal g^{-1} is given by Eq. (21) of Ref. 6. Multiplying by 4184 to convert to J/kg (Ref. 7, p. 13 or Ref. 6, p. 5), the latent heat of vaporization of cesium is

$$L_{Cs} = 6.1555 \times 10^5 \left(1 - \frac{T}{2043}\right)^{0.3547} \qquad \text{(G-22)}$$

The specific heat of liquid cesium in cal $g^{-1}\ {}^{o}K^{-1}$ is given by Eq. (10) of Ref. 6. Multiplying by 4184 to convert to J $kg^{-1}\ {}^{o}K^{-1}$, the specific heat of liquid cesium is

$$c_{Cs_\ell} = 286.2 - 0.3361\ t + 3.345 \times 10^{-4}\ t^2 \qquad \text{(G-23)}$$

where

t = temperature in ^{o}C

= T-273

The specific heat of liquid lithium in cal $g^{-1}\ {}^{o}K^{-1}$ is given by Eq. (130) of Ref. 6. Multiplying by 4184 to convert to J $kg^{-1}\ {}^{o}K^{-1}$, the specific heat of liquid lithium is

$$c_{Li_\ell} = 4425 - 0.5084\ t + 2.237 \times 10^{-4}\ t^2 \qquad \text{(G-24)}$$

where

t = temperature in ^{o}C

= T-273

For the recuperator and desuperheater calculations it is necessary to find the enthalpy change of cesium vapor between superheat conditions T, p and saturation conditions T_s, p at the same pressure. The enthalpy change can be calculated from a mean specific heat defined by

$$\overline{c_p} = \frac{H(T,p) - H(T_s, p)}{T - T_s} \qquad \text{(G-25)}$$

The enthalpy of saturated and superheated cesium vapor is given in Table 9 of Ref. 6. The saturation temperatures and enthalpies from this Table are plotted in Fig. G-1 as a function of pressure over the range of interest, 0.2 - 3.0 atm.

Table G-2 presents the saturation and superheat enthalpies as a function of pressure and temperature. The first line for each pressure gives the saturation conditions: T_s from Fig. G-1 in Column 2 and H_s from Fig. G-1 in Column 3. The remaining lines for each pressure give the temperature and corresponding enthalpy for superheat conditions at that pressure, taken directly from Table 9 of Ref. 6.

The fourth column in Table G-2 gives the temperature increase $\Delta T = T - T_s$ above saturation, and the fifth column gives the enthalpy increase ΔH above saturation. The last column gives the mean specific heat $\Delta H/\Delta T$ (Eq. G-25).

The mean specific heat values are plotted as a function of ΔT in Fig. G-2, and smooth curves are drawn through the points. Each curve is for a fixed pressure and saturation temperature. The curves are cross-plotted in Fig. G-3 to show mean specific heat as a function of saturation temperature at constant ΔT. The dependence of $\overline{c_p}$ on T_s is nearly linear and can be represented by the following equation:

$$\overline{c_p} = 6.66 - 1.6 \times 10^{-3}\ \Delta T + (1.2 \times 10^{-2} - 1.1 \times 10^{-5}\ \Delta T)(T_s - 800) \qquad \text{(G-26)}$$

where $\overline{c_p}$ is in cal g-mole^{-1} $^{o}K^{-1}$.

Equation (G-26) is plotted in Fig. G-3 for comparison with the data. The equation agrees with the data within 1% from $\Delta T = 200$ to $\Delta T = 400$, the range of interest.

To convert $\overline{c_p}$ to J kg^{-1} $^{o}K^{-1}$ Eq. (G-26) must be divided by $W_{Cs_\ell} = 132.9$ to give cal g^{-1} $^{o}K^{-1}$ and then multiplied by 4184 (Ref. 7, p. 13). The combined factor is 4184/132.9 = 31.48.

The latent heat of vaporization of lithium in cal g^{-1} is given by Eq. (142) of Ref. 6. Multiplying by 4184 to convert to J/kg, the latent heat is

$$L_{Li} = 2.536 \times 10^{7} \left(1 - \frac{T}{3173}\right)^{0.3725} \qquad \text{(G-27)}$$

Table G-1

Lithium Equilibrium Constants

T ^{o}K	$\log_{10} K_{f,1}$ (Table 74, Ref. 6)	$\log_{10} K_{f,2}$ (Table 75, Ref. 6)	Q Eq. (G-16)
1000	- 3.0129	- 4.569	1.457
1100	- 2.2919	- 3.667	0.917
1200	- 1.6937	- 2.920	0.467
1300	- 1.1909	- 2.296	0.086
1400	- 0.7621	- 1.764	- 0.240
1500	- 0.3921	- 1.309	- 0.525

Table G-2

Enthalpy Change and Mean Specific Heat of

Cesium Vapor Between Superheat and Saturation

p, atm	T, ^{o}K	H, $\frac{cal}{mole}$	ΔT, ^{o}K	ΔH, $\frac{cal}{mole}$	$\overline{c_p} = \frac{\Delta H}{\Delta T}$, $\frac{cal}{^{o}K\ mole}$
0.2	799	20510	0	0	
	825	20683	26	173	6.654
	900	21169	101	659	6.525
	1000	21793	201	1283	6.383
	1100	22349	301	1839	6.110
	1200	22923	401	2413	6.017
	1300	23559	501	3049	6.086
	1400	24149	601	3639	6.055
0.4	856	20604	0	0	
	875	20763	19	159	8.368
	900	20955	44	351	7.977
	1000	21660	144	1056	7.333
	1100	22259	244	1655	6.782
	1200	22858	344	2254	6.552
	1300	23509	444	2905	6.543
	1400	24110	544	3506	6.445
0.6	892	20665	0	0	
	950	21154	58	489	8.431
	1000	21528	108	863	7.991
	1100	22170	208	1505	7.236
	1200	22794	308	2129	6.912
	1300	23461	408	2796	6.853
	1400	24072	508	3407	6.707

(Continued)

Table G-2 (Continued)

p, atm	T, ^{o}K	H, cal/mole	ΔT, ^{o}K	ΔH, cal/mole	$\overline{c_p} = \frac{\Delta H}{\Delta T}$, cal/$^{o}K$ mole
0.8	920	20712	0	0	
	975	21200	55	488	8.873
	1000	21398	80	686	8.575
	1050	21759	130	1047	8.054
	1100	22084	180	1372	7.622
	1200	22733	280	2021	7.218
	1300	23414	380	2702	7.111
	1400	24036	480	3324	6.925
1.0	942	20748	0	0	
	1000	21269	58	521	8.983
	1050	21656	108	908	8.407
	1100	22000	158	1252	7.924
	1200	22673	258	1925	7.461
	1300	23369	358	2621	7.321
	1400	24001	458	3253	7.103
2.0	1021	20880	0	0	
	1100	21606	79	726	9.190
	1200	22399	179	1519	8.486
	1300	23167	279	2287	8.197
	1400	23844	379	2964	7.821
3.0	1074	20975	0	0	
	1200	22156	126	1181	9.373
	1300	22990	226	2015	8.916
	1400	23709	326	2734	8.387

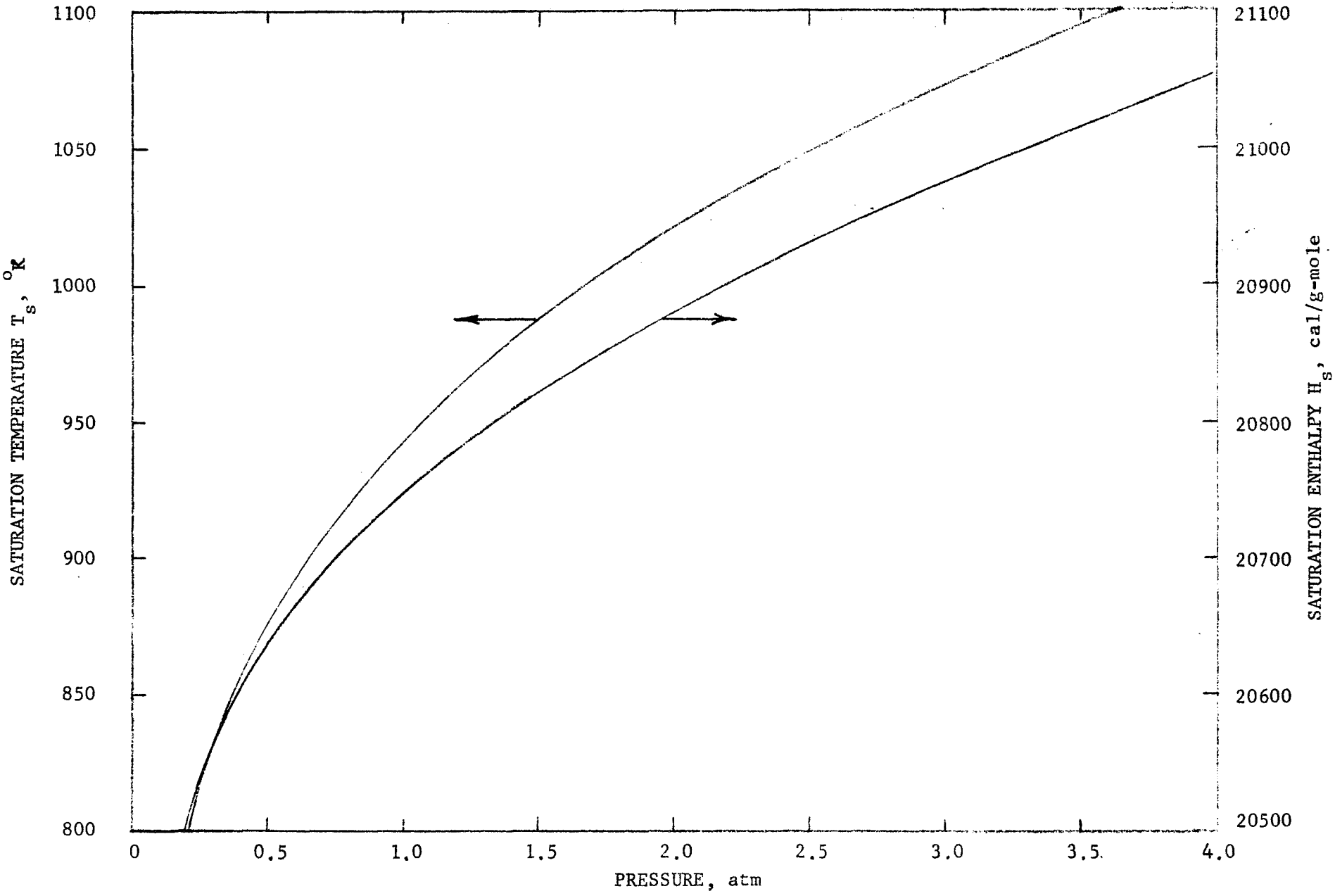

Fig. G-1. Saturation temperature and enthalpy of cesium (Ref. 6, Table 9)

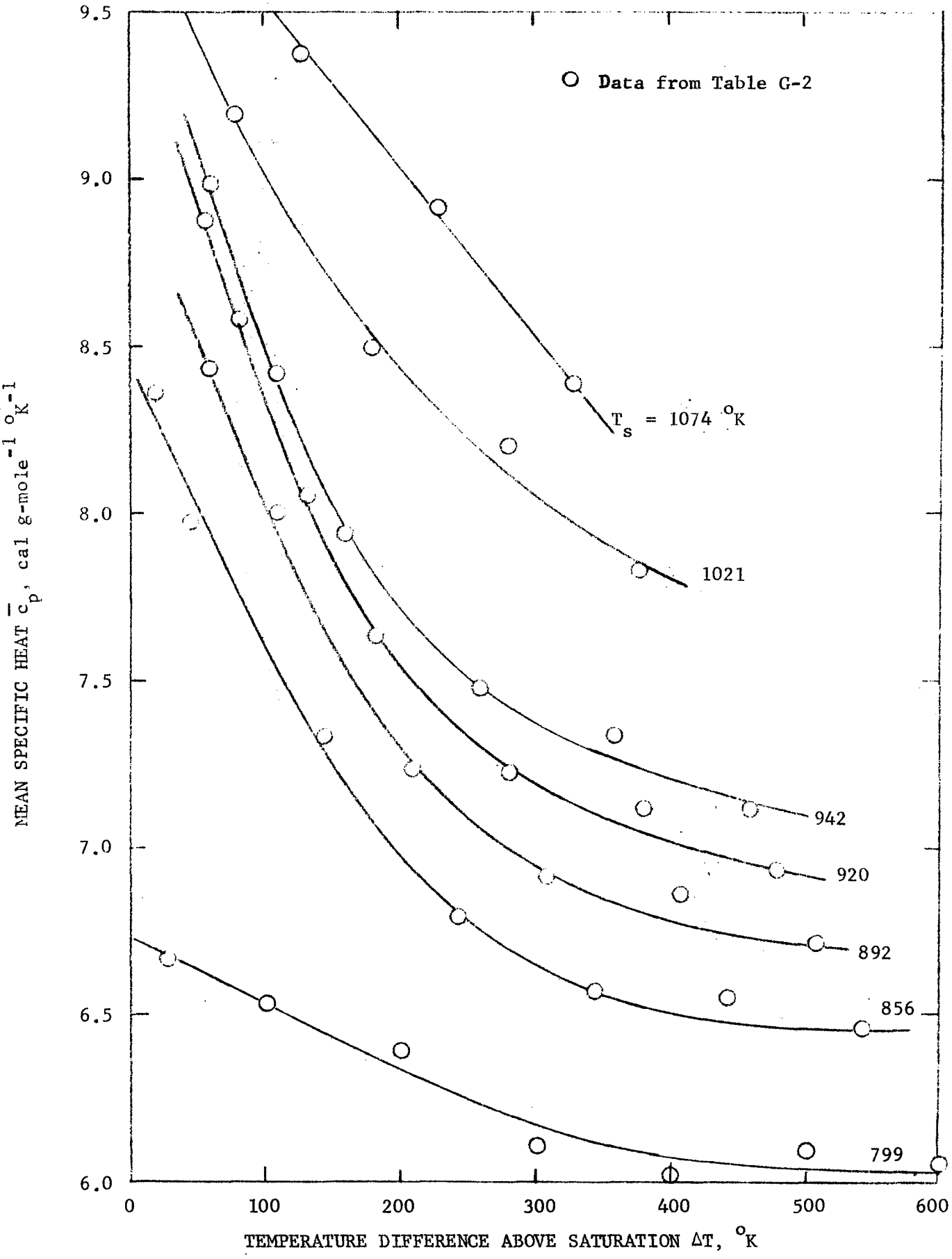

Fig. G-2. Mean specific heat of cesium vapor between superheat and saturation

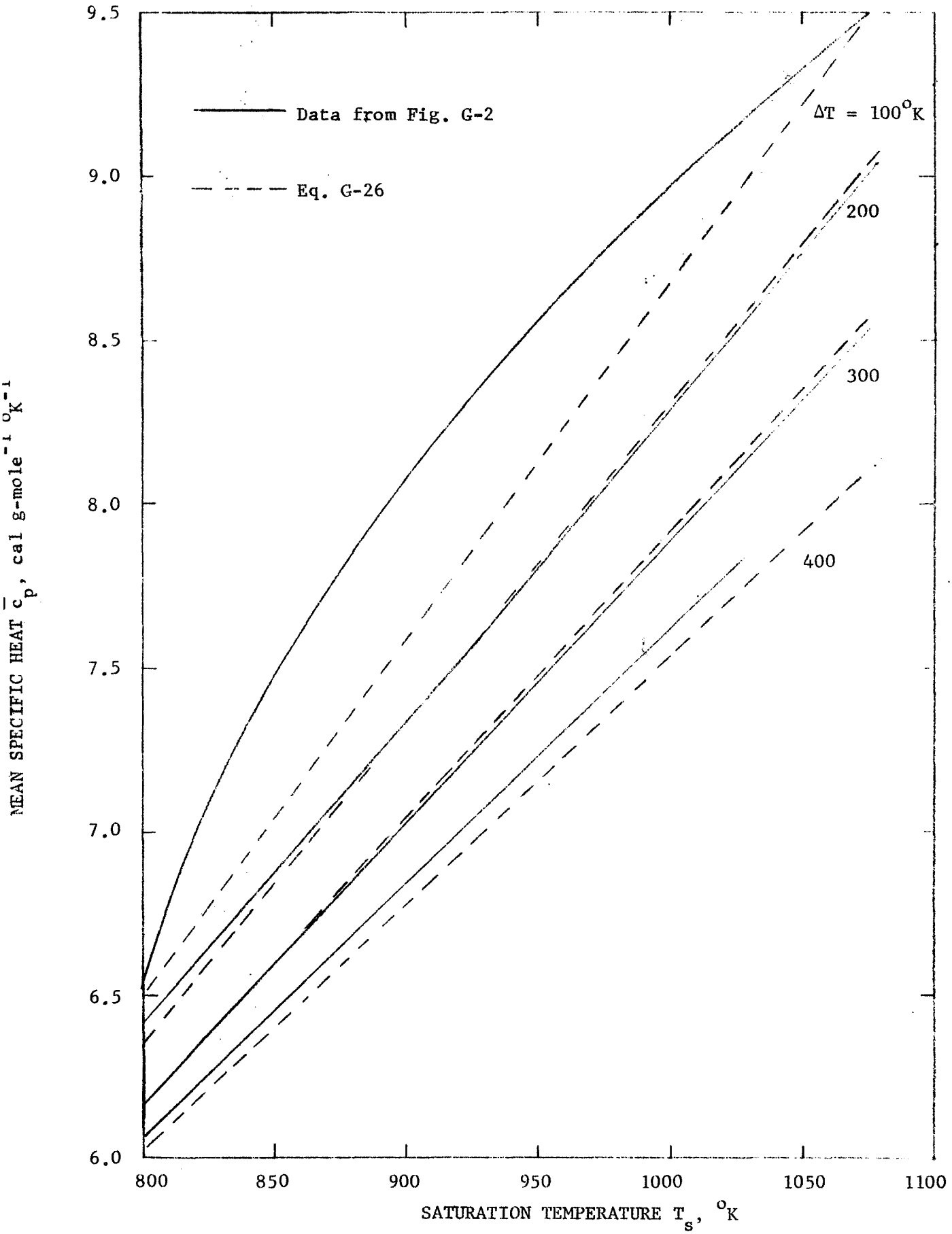

Fig. G-3. Mean specific heat of cesium vapor between superheat and saturation as a function of saturation temperature, and comparison with Eq. G-26

Appendix IIH

Effective Radiating Temperature of a Variable-Temperature Radiator

A fluid enters a radiator at temperature T_1 and leaves at temperature T_2 after giving up heat Q. The heat rejected over each increment of temperature is assumed to be constant. Thus,

$$\frac{dQ}{dT} = \frac{Q}{T_2 - T_1} \tag{H-1}$$

It is desired to find an effective temperature such that

$$Q = \sigma \epsilon A T_{eff}^4 \tag{H-2}$$

where

σ = Stefan-Boltzman constant

ϵ = emissivity

A = radiator area

The increment of area required to reject increment of heat dQ at local temperature T is

$$dA = \frac{dQ}{\sigma \epsilon T^4} \tag{H-3}$$

Substituting dQ from Eq. (H-1),

$$dA = \frac{Q\, dT}{\sigma \epsilon (T_2 - T_1) T^4} \tag{H-4}$$

Integrating from T_1 to T_2, the total area is

$$A = \frac{Q}{3\sigma \epsilon T_1^3 T_2} \left[1 + \frac{T_1}{T_2} + \left(\frac{T_1}{T_2} \right)^2 \right] \tag{H-5}$$

Substituting A into Eq. (H-2) the effective temperature is given by

$$T_{eff}^4 = \frac{3 T_1^3 T_2}{1 + \frac{T_1}{T_2} + \left(\frac{T_1}{T_2} \right)^2} \tag{H-6}$$

GENERAL ELECTRIC